PhD program in QUANTUM TECHONOLOGIES

XXXVI cycle

Coordinatore: Prof. Francesco Tafuri

TARGET DETECTION WITH QUANTUM ILLUMINATION AND ENTANGLEMENT GENERATION THROUGH HEISENBERG EXCHANGE INTERACTION

Settore Scientifico Disciplinare FIS/02

Dottorando
THEERTHAGIRI LAKSHMANAN

Tutore
Prof. DAVID VITALI

Academic Year (Nov 2020 - Dec 2023)

Abstract

In cases where entanglement is disrupted, quantum illumination (QI) surpasses classical illumination significantly in target detection. The superiority of QI was previously measured using a Bayesian framework, assuming equal likelihood of the target's presence or absence, with error probability as the performance metric. However, radar theory favors the Neyman-Pearson performance criterion over the Bayesian approach. The Neyman-Pearson criterion sidesteps challenges related to assigning appropriate prior probabilities to target presence and absence, as well as the associated costs of false alarms and missed detections. This study utilizes findings from our phase conjugate receiver (PC) and Correlation-To-Displacement (C-D) receiver research to compute the receiver operating characteristic, which illustrates the trade-off between detection probability and false alarm probability. This analysis aims to optimize QI target detection under the Neyman-Pearson criterion. The correlation-To-Displacement (C-D) receiver is studied in this thesis first part. Entanglement is vulnerable to degradation in a noisy sensing scenario, but surprisingly, the quantum illumination protocol has demonstrated that its advantage can survive. However, designing a measurement system that realizes this advantage is challenging since the information is hidden in the weak correlation embedded in the noise at the receiver side. Recent progress in a correlation-to-displacement conversion module provides a route towards an optimal protocol for practical microwave quantum illumination. In this work, we extend the conversion module to accommodate experimental imperfections that are ubiquitous in microwave systems. To mitigate loss, we propose amplification of

the return signals. In the case of ideal amplification, the entire six-decibel error-exponent advantage in target detection error can be maintained. However, in the case of noisy amplification, this advantage is reduced to three-decibel. We analyze the quantum advantage under different scenarios with a Kennedy receiver in the final measurement. In the ideal case, the performance still achieves the optimal one over a fairly large range with only on-off detection. Empowered by photon number resolving detectors, the performance is further improved and also analyzed in terms of receiver operating characteristic curves. Our findings pave the way for the development of practical microwave quantum illumination systems.

In the second part of this thesis, we generate the W entangled state through Heisenberg exchange interaction. The spread of entanglement is a problem of great interest. It is particularly relevant to quantum state synthesis, where an initial direct-product state is sought to be converted into a highly entangled target state. In devices based on pairwise exchange interactions, such a process can be carried out and optimized in various ways. As a benchmark problem, we consider the task of spreading one excitation among N two-level atoms or qubits which is the typical feature of a W state. Starting from an initial state where one qubit is excited, we seek a target state where all qubits have the same excitation amplitude a generalized-W state. This target is to be reached by suitably chosen pairwise exchange interactions. For example, we may have a a setup where any pair of qubits can be brought into proximity for a controllable period of time. We describe three protocols that accomplish this task, each with $N-1$ tightly-constrained steps. In the first, one atom acts as a flying qubit that sequentially interacts with all others. In the second, qubits interact pairwise in sequential order. In these two cases, the required interaction times follow a pattern with an elegant geometric interpretation. They correspond to angles within the spiral of Theodorus – a construction known for more than two millennia. The third protocol follows a divide-and-conquer approach – dividing equally between two qubits at each step. For large N, the flying-qubit protocol yields a total interaction time

that scales as $\sqrt{N}$, while the sequential approach scales linearly with N. For the divide-and-conquer approach, the time has a lower bound that scales as $\ln N$. With any such protocol, we show that the phase differences in the final state cannot be independently controlled. For instance, a W-state (where all phases are equal) cannot be generated by pairwise exchange.

Contents

Abstract **1**

Declaration **1**

Acknowledgements **2**

1 Introduction **4**

1.1 Motivation 5

1.1.1 Classical Radar 8

1.1.2 Signal-to-noise ratio (SNR) 10

1.1.3 Quantum Radar 11

1.2 The classical benchmark for quantum radar 12

1.3 Types of radar 12

1.3.1 Lloyd initial single photon quantum illumination proposal 13

1.3.2 Gaussian source of Quantum illumination 16

1.4 Microwave Quantum illumination 19

1.5 Illumination receivers 20

1.5.1 Optical parametric amplifier (OPA) 21

1.5.2 Phase conjugate receiver (PCR) 22

1.6 Experimental studies 23

1.7 Thesis outline 24

2 Preliminary Notations **28**

2.1 Introduction 28

2.2 Continuous variable systems, harmonic oscillators and bosonic modes . . 29

2.2.1 Bosonic modes 29

2.2.2 Phase-space representation 31

2.2.3 Coherent State 35

2.2.4 Photon statistics of coherent states 36

2.2.5 Thermal State 36

2.2.6 Single mode Squeezed State 37

2.2.7 Two mode Squeezed State 38

2.3 Quantum Hypothesis testing 40

2.3.1 Bayes Symmetric Hypothesis test 40

2.3.2 Helstrom Bound 43

2.3.3 Quantum chernoff Bound (QCB) 45

2.3.4 Quantum Battacharyya Bound 46

2.3.5 Formulas for Gaussian states 47

2.4 Measurement Detectors 49

2.4.1 General-dyne measurement 52

2.4.2 Conditional general-dyne measurement 53

3 Microwave quantum illumination with correlation-to-displacement conversion **56**

3.1 Introduction 56

3.2 Overall protocol 59

3.3 Quantum illumination for target detection 60

3.4 Correlation-to-displacement conversion in the ideal case 62

3.4.1 Heterodyne measurement 63

3.5 Practical microwave detection scenario 67
3.6 Correlation-to-displacement conversion in practice 70
3.6.1 Performance limits of the conversion module in practice 72
3.6.2 Kennedy receiver 74
3.7 Performance benchmarks 76
3.8 Enhanced performance with number-resolving detection 78
3.8.1 Bayesian error probability 81
3.8.2 Receiver operating characteristic 82

4 Synthesis of Entanglement **88**
4.1 Quantum Entanglement 89
4.2 Density Operator 90
4.3 Entanglement Entropy 91
4.4 Qubit representation 91
4.4.1 Two-level system 93
4.4.2 Bell state 95
4.4.3 W state synthesis 97
4.5 Spin system 98
4.5.1 Collective spin operators 100
4.6 Dicke model 102
4.7 Two Spin-1/2 particles 104
4.7.1 Three Spin-1/2 particles 105
4.8 Many-body Entangled state 108

5 Spreading entanglement through pairwise exchange interactions **110**
5.1 Introduction 110
5.2 Entanglement by exchange 112
5.3 Problem statement 114

5.4 Protocol with a single flying qubit 115
5.5 Protocol with sequential pairwise interactions 118
5.6 Divide-and-conquer protocol 120
5.7 Phase differences in the target state 122

6 Conclusion **123**

6.1 Future Direction 126

List of Figures

1.1 Classical Radar 9

1.2 Quantum illumination 14

1.3 Optical parametric amplifier (OPA) with gain G, the measurement of the total number of photons, N, is counted. If N is less than a certain threshold η, the receiver collapse to H_0; otherwise, H_1. 21

1.4 The input of the balanced difference detector in the PCR are phase-conjugated return and idler modes. The measured total number of photon counts, N, less than a threshold η, the receiver decides H_0; otherwise, H_1. 22

2.1 Depicts the vacuum state and the coherent state. 36

2.2 Single mode: (a) Squeezed vacuum state and (b) displaced squeezed state 38

2.3 Two mode: Squeezed vacuum state 39

2.4 Hypothesis test 41

2.5 Schematic setup at the basics of balanced homodyne and heterodyne detection 50

3.1 Schematic of the quantum illumination, with a practical receiver based on correlation-to-displacement conversion, in presence of noise and loss. 'het': heterodyne detection. 'PD': photo-detection. 58

3.2 Beamsplitter array with proper weights with each $\hat{a}_{I,m}$ 63

3.3 Behavior of $r_{\mathrm{C}\to\mathrm{D}}^{(\mathrm{LB})}/r_{\mathrm{CS}}$ as a function of $\log_{10}[N_V(1-1/G)]$ with amplification and ideal signal and idler detection, for different values of $\log_{10} N_S$, given $N_B = 1250$ and $\kappa = 0.01$. $N_S = \left\{10^{1}, 10^{0}, 10^{-1}, 10^{-2}, 10^{-3}, 10^{-6}\right\}$ from bottom to top, as indicated by the labels on top of the curves. The plot indicates that the amplification stage provides a factor of advantage greater than 2 (as indicated by the horizontal dashed line) for a range of relevant parameters. This is due to the robust compensation of noise effects achieved by amplifying, as demonstrated by the vertical dashed line at $N_V(1-1/G) = N_B$. 67

3.4 Black lines represent the ratio $r_{\mathrm{C}\to\mathrm{D}}^{(\mathrm{LB})}/r_{\mathrm{CS}}$ as a function of $\log_{10} N_S$, purple ones $r_{\mathrm{C}\to\mathrm{D}}^{(\mathrm{UB})}/r_{\mathrm{CS}}$, dashed gray for the QCB (see chapter 2), and blue ones $r_{\mathrm{CS}}^{(\mathrm{NI})}/r_{\mathrm{CS}}$, where $r_{\mathrm{CS}}^{\mathrm{NI}}$ is obtained by applying the substitution Eq. (3.20). (a) Ideal return detection, no additional signal loss $\eta_S = 1$ and therefore no amplification needed, $G = 1$. (b) Lossy return detection $\eta_S = 0.1$, assuming pure loss $N_{E_1} = 0$. We apply quantum-limited amplification of $G = 100$, $N_V = 0$. (c) Ideal return detection $\eta_S = 1$, and noisy amplification $G = 100$, $N_V = N_B$ at room temperature. (d) Lossy return detection $\eta_S = 0.1$ with noise $N_{E_1} = N_B$ at room temperature. We apply noisy amplification $G = 100$, $N_V = N_B$ at room temperature. The lower bound of the C→D module consistently aligns with the QCB. 72

3.5 The impact of losses and gain on two scenarios: (a) a cool case with $N_V = N_{E_1} = 0.1$ (corresponding to $T_S = 100$ mK) and (b) a warm one with $N_V = N_{E_1} = N_B$ (corresponding to $T_S = 300$ K). The other parameters are fixed at $N_B = 1250$, $\kappa = 0.01$, $N_S = 10^{-3}$, and $\eta_I = 1$ (i.e., we assume the idler is ideally stored). Solid lines represent the ratio $r^{(\mathrm{LB})}_{\mathrm{C}\to\mathrm{D}}/r_{\mathrm{CS}}$ as a function of the gain $\log_{10} G$, for different values of η_S (visible in the legend); dashed lines $r^{(\mathrm{NI})}_{\mathrm{CS}}/r_{\mathrm{CS}}$, where $r^{\mathrm{NI}}_{\mathrm{CS}}$ is obtained by applying the substitution Eq. (3.20). Amplification is not necessary in a cool environment (a), but it is crucial in practical cases characterized by warm environments (b) where $\eta_S < 1/2$: only through amplification can a factor of 2 advantage be achieved. . . . 73

3.6 Comparison of the error exponent ratio r/r_{CS} between the C→D module and the PCR [see Eqs. (3.12), (3.37), and (3.13), respectively] as a function of $\log_{10} N_S$ and $\log_{10} N_B$. The other parameters correspond to the 'cool' case and are set to: $N_V = N_{E_1} = N_{V_{\mathrm{PCR}}} = 0.1$ (corresponding to $T_S = 100$ mK), $N_{E_2} = 4\times10^{-11}$ (corresponding to $T_I = 10$ mK), $G = 100$, $G_{\mathrm{PCR}} = 2$, $\eta_S = 0.1$, and $\eta_I = 0.9$. The red circle represents the parameters used in Fig. 3.7. The C→D module possesses clear better performance, as stated by the wide yellowish areas. 76

3.7 Error probability as a function of the number of copies M in both the non-ideal (solid) and ideal (dashed) case. The non-ideal case is characterised by: $N_S = 10^{-3}$, $N_B = 1250$, $N_{E_2} = 4\times10^{-11}$ (corresponding to $T_I = 10$ mK), $\kappa = 0.01$, $G = 100$, $\eta_S = 0.1$, $\eta_I = 0.9$, and $G_{\mathrm{PCR}} = 2$. (a) Cool case with $N_V = N_{E_1} = N_{V_{\mathrm{PCR}}} = 10^{-1}$ (corresponding to $T_S = 100$ mK), (b) warm one $N_V = N_{E_1} = N_{V_{\mathrm{PCR}}} = 1250$ (corresponding to $T_S = 300$ K). Dashed lines are the performance for each solid colored curve in the ideal scenario ($\eta_S = \eta_I = 1$ and no amplification $G = 1$). The horizontal dashed line marks $P_{\mathrm{E,homo}} = 0.05$. 78

3.8 Comparison based on the error probability ratio $\log_{10}(P_E/P_{\mathrm{E,homo}})$ between (a) the C↛D module (equipped with an on/off Kennedy receiver) and (b) the PCR [see Eqs. (3.35), (3.37), and (3.36), respectively] vs. $\log_{10} N_S$ and $\log_{10} N_B$. The value of M is selected to set $P_{\mathrm{E,homo}} = 0.05$. The other parameters correspond to the 'cool' case and are: $N_V = N_{E_1} = N_{V_{\mathrm{PCR}}} = 0.1$, $N_{E_2} = 4 \times 10^{-11}$, $G = 100$, $G_{\mathrm{PCR}} = 2$, $\eta_S = 0.1$, and $\eta_I = 0.9$. The red circle indicates the parameters used in Fig. 3.7. As shown by the wide dark area, the C↛D module outperforms the PCR. 80

3.9 The saturation of the red line in Fig. 3.7 suggests an improvement, following the lines of Ref. [22], where a variable threshold decision strategy approach has been used for asymptotic analysis. The red curve reproduces the usual Kennedy receiver corresponding to the fixed threshold $n_D = 1$. The dashed grey lines corresponds to the case of fixed, increasing values of n_D. The orange line gives the optimized result in which n_D is adjusted according to M, and therefore to the two states to be discriminated. This latter approach yields results comparable to those of the non-ideal QCB (blue). Parameter values are the same as those of Fig. 3.7. 83

3.10 Comparison of ROC curves. The red line shows the performance of the C↛D module with a PNRD; the black one that of the PCR given by Eq. (3.57); the dashed light gray line depicts the performance of the Gaussian approximation of Eq. (3.51); the full dark grey line gives the non-ideal classical benchmark [using Eq. (3.57) with $d_{\mathrm{PCR}} \to d_{\mathrm{CS}}$ plus Eq. (3.20)]. The parameters used are the same as in Fig. 3.6 and 3.8 (indicated by the red dots there), with $M = 69 \times 10^7$. 85

4.1 Beam Splitter 92

4.2 Bell state preparation 95

4.3 Bell state Teleportation 96
4.4 A circuit to create a perfect W-state involves using the Pauli X-gate and the general unitary gate $U3(\theta, \Phi, \lambda)$. 97
4.5 Silver atoms are heated in an oven with a small opening, allowing some atoms to escape. The emitted atoms pass through a non-homogeneous magnetic field created by pole pieces. 98
4.6 Collapse wavefunction measurement 99
4.7 Cavity QED setup and Spin representation of Bloch sphere 104

5.1 Three protocols illustrated for a system with $N = 4$ qubits. (a) The initial direct product state with one qubit excited and $N - 1$ qubits in the ground state. (b) A flying-qubit protocol where qubit-1 interacts with each of the other qubits in order. (c) A sequential protocol where pairs of neighbouring qubits interact in succession. (d) A divide-and-conquer protocol where the system is arranged hierarchically in units of two qubits. At each stage, interactions act at one level of the hierarchy. 115
5.2 Top: The spiral of Theodorus, constructed as a sequence of right-angled triangles. Bottom: The n^{th} triangle in the spiral, with sides 1, $\sqrt{n}$ and $\sqrt{n+1}$. 117
5.3 The total interaction time t vs. the number of qubits, N for the three protocols discussed here. The lines show the approximate scaling form for large N. 121

List of Tables

3.1 Values of mean thermal photon numbers for a microwave mode at $\omega = 2\pi \times 5$ GHz at temperature values of interest. 62

Declaration

I certify that this thesis is entirely my own work and has not been previously submitted for any academic award. All sources are credited in the References section. When I publish with collaborators, I accept responsibility for the content presented here while giving appropriate credit to my collaborators. Each published item's listed author.

[1] Microwave quantum illumination with correlation-to-displacement conversion, Jacopo Angeletti, Haowei Shi, **Theerthagiri Lakshmanan**, David Vitali, Quntao Zhuang, Phys. Rev. Applied 20, 024030 – Published 11 August 2023.

[2] **Theerthagiri L**., Ganesh R. Spreading entanglement through pairwise exchange interactions. Quantum Inf Process 22, 355 (2023). https://doi.org/10.1007/s11128-023-04104-z

Acknowledgements

I extend my sincere gratitude to the Science and Technology Research Council of Italy for their invaluable support during my research journey. I am deeply thankful to **Prof. David Vitali**, my PhD supervisor, for his consistent guidance and expertise. Without his advice, I wouldn't have developed into the confident and independent researcher I am today, and this thesis wouldn't have been possible.

This thesis is dedicated to **Emeritus Prof. G. Baskaran** from the Condensed Matter Group at the Institute of Mathematical Sciences, Chennai, Tamilnadu, India, and the Perimeter Institute for Theoretical Physics, Canada, as well as **Prof. R. Ganesh** from the Condensed Matter Group at Brock University, St. Catharines, Ontario, Canada. Their contributions and expertise have been invaluable, and I hold them in the highest esteem.

I want to extend my profound gratitude to **Prof. Sergio Ciliberto**, who is part of the Statistical Mechanics group and serves as the Research Director at the CNRS Laboratoire de Physique de l'ENS de Lyon, located at 46 Allée d'Italie, 69364 Lyon, France. His substantial collaboration has greatly contributed to enhancing my independent research skills and fostering critical thinking.

I express my deep appreciation to **Prof. Rita John** from the Condensed Matter Group at the Department of Theoretical Physics, University of Madras, for her constant encouragement and support in pursuing my research aspirations.

Special thanks to **Retired Prof. Ranabir Chakrabarti** from the Department of Theoretical Physics at the University of Madras for his encouragement and guidance in fol-

lowing my research dreams.

I am indebted to **Mr. R. Balan**, Section Officer at the Department of Theoretical Physics, University of Madras, for his motivating presence and continuous support in my research endeavors.

My gratitude goes to **Dr. Yogesh** and **Dr. Balamurugan** from the Department of Theoretical Physics, University of Madras, for their exceptional teaching in theoretical physics and unwavering encouragement to pursue my research goals.

I wish to acknowledge **Mr. Pachiyappan Narayanan** from the Green Mathematical Institute in Chennai for his encouragement in my research career and for sharing his knowledge in pure mathematics.

I am thankful to **Mr. Radhakrishnan P**. for his invaluable assistance in realizing my research aspirations.

I am also appreciative of the unwavering moral support provided by **Niveadhitha S** throughout my research career.

Lastly, I express my deepest gratitude to my parents, **Devagi G**. and **Lakshmanan R**., and friends for their boundless love, support, and sacrifices that have enabled me to pursue my academic pursuits.

Chapter 1

Introduction

In this thesis, I explore two distinct areas of research. The first area delves into quantum illumination involving target detection, while the second area focuses on the synthesis of quantum entangled W states through exchange interactions.

The objective of this chapter is to outline the rationale behind these two distinct research topics. Section 1.1 explores the motivation for generating entanglement through Heisenberg exchange interactions and delves into the concept of quantum illumination with target detection.

Subsection 1.1 examines the conventional pulse-based classical radar system, which is proficient in detecting and gauging a target's range. In classical radar, the signal-to-noise ratio (SNR) signifies the ratio of the transmitted signal strength to the level of background noise received by the radar system.

Section 1.3 delves into the early conceptualization of the quantum illumination narrative. Quantum illumination, a type of quantum sensing, has recently captured substantial attention. Initially presented as quantum radar, it demonstrates the potential to outperform classical radar systems, particularly in situations where classical systems encounter inherent constraints.

Lastly, in Section 1.4, we clarify the concept of microwave quantum illumination and

its associated receivers. The presently accessible receivers include an optical parametric amplifier and a phase-conjugate receiver, both incorporated into an experimental setup. Section 1.7 talks about the outline of my thesis work.

1.1 Motivation

Quantum technologies leverage quantum-mechanical phenomena to achieve outcomes that are not possible with classical means. This field offers numerous practical applications, including quantum computing, quantum cryptography, quantum sensing, and quantum metrology. Before delving into the technological aspects, it is essential to grasp the fundamental principles of synthesizing quantum entanglement across different quantum optical setups. Scientific research has deeply delved into bipartite entanglement, resulting in a thorough comprehension of the properties, creation, and uses of entangled states involving two particles. Lately, there has been an increasing emphasis on examining entanglement in systems with multiple particles. In the realm of multiparticle entanglement [25], researchers have mainly concentrated on two specific categories of states: the GHz class state and the W class state. The GHz state and the W state are distinct and cannot be transformed into each other through stochastic local operations and classical communications (SLOCC) [93, 135]. The GHz state is particularly noteworthy due to its maximal entanglement properties: it strongly violates Bell inequalities, has maximum mutual information in measurement outcomes, and can be used to locally create an EPR state shared by any two of the three parties with certainty. In contrast, even when one of the three particles is traced out, the remaining two particles in the W state still maintain a relatively high level of entanglement. Consequently, the W state demonstrates greater stability in the face of particle losses compared to the GHz state. Each application relies on the entangled states that are prepared initially [149], to achieve this, systematic methods are required to transform direct-product states into the desired superposition states.

These processes must be optimized to minimize operation time and counter the effects of decoherence. Several studies have focused on time-optimized protocols due to this imperative. Simultaneously, ensuring scalability is paramount. Entanglement protocols must be efficient as the number of qubits in quantum devices increases. Optimization balancing operating time and qubit count complexity becomes crucial in this context. Drawing inspiration from these principles, we explore the fundamental task of distributing entanglement, specifically distributing a single excitation uniformly among N qubits [122]. The entanglement of multiple entities, such as qubits within a device, presents intriguing possibilities. Many experiments have successfully generated the W state, and there have been numerous suggestions for its synthesis. Therefore, a key goal in quantum information theory (QIT) is the preparation of entanglement. Various techniques, such as single-photon interference, cavity quantum electrodynamics (QED) [47, 147], parametric down-conversion, ion trap methods, and nuclear magnetic resonance (NMR), have been recently suggested for generating entangled states. Further information on the generation of the W state will be discussed in more detail later in Chapter 4.

To explore these applications of quantum entanglement, researchers study the interactions of quantum systems with each other and external factors, particularly focusing on the interactions between different quantum states. These interactions can lead to the creation of entangled states, which possess quantum correlations that have no classical equivalent. These correlations are essential for achieving rapid quantum information processing and unmatched measurement sensitivity. Leveraging these quantum correlations enables the development of highly sensitive sensors at the nanoscale, surpassing classical limits and scaling proportionally with sensor size. Among various implementations of quantum technologies, practical sensing applications appear to be more attainable in the near future compared to others that require precise control over multiple quantum states simultaneously. Recent advancements have demonstrated the potential of exploiting nonclassical states of radiation in both theoretical and experimental quantum technologies.

One specific example, which is the focus of this thesis, is quantum illumination with a target detection. By leveraging quantum mechanical phenomena, quantum target detection offers a theoretical advantage in detection capabilities. This task is closely related to other quantum sensing protocols such as quantum ranging, quantum metrology, quantum sensing, and quantum illumination (also known as quantum radar). Quantum illumination, being the first microwave-based quantum target detection method, shows significant improvements over classical radar systems and other coherent state protocols. The first three quantum illumination and its applications in microwave quantum target detection.

In order to avoid misunderstandings, it is necessary to define terms like "quantum target detection", "quantum illumination", and "quantum radar" before using them in this thesis. Any protocol based on the principles of quantum mechanics that finds a target or establishes its presence in a designated region of interest is referred to as quantum target detection. All aspects of the protocol are susceptible to quantumness, such as the receiver's decision-making process or the source's probing of the target region. Within the domain of quantum target detection, quantum illumination (QI) is a distinct category that relies on entanglement. In the context of QI, the probing source forms an entangled connection with the receiver, allowing the receiver to glean insights into the interactions of the source through entanglement as decisions are made. Quantum radar refers to a specific application of certain quantum target detection techniques meant for the microwave range. This application is crucial because QI's detection efficiency is increased by significant noise, which is commonly present in the microwave range. Interestingly, QI is not a prerequisite for using quantum radar exclusively; in fact, QI is frequently used in quantum radar research.

1.1.1 Classical Radar

Radar technology has its roots in the early 20th century, stemming from Heinrich Hertz's discovery of radio wave reflection by solid objects in 1886 [107, 108]. The initial pulse-based radar system, capable of detecting and measuring a target's range, was created by the US Naval Research Laboratory in 1934. Since then, major military powers have extensively researched and developed radar technology. Remarkably, the fundamental principles of classical radar systems have remained unchanged for over 50 years.

A radar system is an electrical setup that sends out radiofrequency (RF) electromagnetic waves to a designated area and captures the reflected waves when they bounce off objects in that region. Figure 1.1 shows the key components: transmitting the radar signal, signal propagation through the atmosphere, signal reflection from the target, and receiving the reflected signals. Although radar systems may have different setups, they usually include fundamental parts: a transmitter, an antenna, a receiver, and a signal processor.

The radar system's receiving antenna gathers reflected electromagnetic waves from objects, including both the target and unwanted clutter. The portion of the signal that comes back to the radar antenna is captured and sent to the receiver circuits. Within the receiver, the received signal is amplified, and the radiofrequency (RF) signal is transformed into an intermediate frequency (IF). This signal then goes through an analog-to-digital converter (ADC) and is sent to the signal/data processor. The detector in the receiver is responsible for extracting the modulated target return signal by removing the carrier wave. This process allows the target data to be separated and analyzed by the signal processor. By removing the carrier, the detector enables the extraction and processing of specific information related to the target.

The range, denoted as R, to a detected target can be calculated by considering the time it takes for the electromagnetic (EM) waves to travel to the target and back at the speed of light [79]. Since distance is equal to speed multiplied by time, and the EM waves have

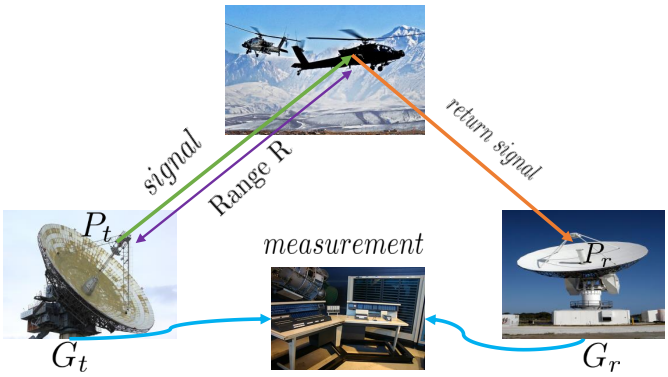

Figure 1.1: Classical Radar

to travel the distance to the target and then back to the radar, which is a total of $2R$. The emitted electromagnetic pulse, after reflection off the target, arrives back at the receiver after a time, Δt, which can be used to compute the target range

$$R = \frac{c\Delta t}{2} \tag{1.1}$$

where c is the speed of light in a vacuum. In general, a significant amount of the emitted energy is lost during the radar pulse propagation process. This energy loss occurs due to various factors, including attenuation in the medium through which the pulse travels and the reflectivity of the target, which is influenced by its material properties and geometry. Consequently, the total power density incident on the target can be expressed as follows:

$$W_T = \frac{P_t G_t F^2}{4\pi R_T^2} \tag{1.2}$$

where the form factor $F \in [0, 1]$ describes the transmissivity of the area between the target and the radar, the electromagnetic pulse of power P_t, target located a distance R_T and transmitter gain G_t.

The reflectivity of the target is quantified by a parameter known as the radar cross-section (RCS), which represents the proportion of incident power that is scattered back

towards the receiver. The power density that arrives back at the receiver can be expressed as follows:

$$W_r = \frac{P_t \sigma G_t F^4}{4\pi R_T^4} = \frac{P_r}{A_r} \tag{1.3}$$

where P_r is the power arriving at the receiver and A_r is the receiver's collecting area. Thus we arrive at the radar equation

$$P_r = \frac{P_t G_t A_r \sigma F^4}{4\pi R_T^4} \tag{1.4}$$

This formulation is used to model the performance of current state-of-the-art classical radar systems.

1.1.2 Signal-to-noise ratio (SNR)

The signal-to-noise ratio (SNR) in radar is the ratio of the transmitted signal strength to the amount of background noise received by the radar system [65, 94]. This noise, known as Johnson-Nyquist noise, is caused by inherent electronic noise in the radar system. Thermal noise affects all radar receivers, limiting the detectable strength of target signals. A higher signal-to-noise ratio (SNR) indicates a stronger signal, which improves the system's ability to identify and isolate targets from background noise. The overall power associated with this noise is as follows:

$$P_m = k_B T B_m F_m, \tag{1.5}$$

where T is the system operating temperature, κ_B is the Boltzmann constant, F_m is a dimensionless constant expressing the variation of the true noise with respect to the purely thermal Johnson noise, and B_n is the receiver bandwidth. The definition of the signal-to-noise ratio defined as

$$SNR = \frac{P_r}{P_m} = \frac{PGA_R \sigma F^4}{(4\pi)^2 R^4 \kappa_B T B_m F_m}. \tag{1.6}$$

Further expressing the collecting area of the receiver, A_r, in terms of the receiver gain, $G_R = 4\pi A_R/\lambda^2$, we are able to write

$$SNR = \frac{P_t G_t G_R A_R \sigma \lambda^2 F^4}{(4\pi)^2 R^4 \kappa_B T B_m F_m}. \tag{1.7}$$

There is a minimum detectable signal, SNR, that must be greater than the system noise [73]. The maximum detection range, for a fixed given minimum SNR_{min} is given by

$$R_{max} \approx \left(\frac{P_t G_t G_R A_R \sigma \lambda^2 F^4}{(4\pi)^2 R^4 \kappa_B T B_m F_m \, SNR_{min}} \right)^{1/4}, \tag{1.8}$$

where SNR_{min} is typically between 10 and 20 dB.

1.1.3 Quantum Radar

Quantum radar, a type of quantum sensing, has gained significant interest in recent years. Initially introduced as quantum illumination (QI) [82, 105, 134], it holds the potential to surpass classical radar systems. This advantage stems from the presence of entanglement, a purely quantum mechanical phenomenon, in the quantum radar system. Quantum radar offers improved performance even in situations where classical radar capabilities are known to be restricted, such as:

(i) For long-range detection, classical radar systems face limitations imposed by their intrinsic electronic noise, leading to a minimum achievable signal-to-noise ratio. Quantum radar, however, shows potential in surpassing these limitations by leveraging its unique properties. It can provide enhanced detection capabilities even at long ranges, outperforming classical radar systems in terms of performance.

(ii) Quantum radar also holds promise in dealing with challenging environments characterized by losses, noise, and various sources of interference. These environments typically include thermal background noise, clutter from surrounding objects, and potential

electronic countermeasure activities. By harnessing the advantages of quantum technologies, quantum radar can mitigate the effects of these environmental factors, allowing for improved detection and target identification capabilities compared to classical radar systems.

1.2 The classical benchmark for quantum radar

In the context of this thesis and the existing literature, the term "classical benchmark" does not refer to the classical radar system described in the following sections . Instead, it pertains to the most ideal classical quantum state within quantum optics, known as the coherent state. Coherent states, which will be extensively discussed in Chapter 2, saturate the Heisenberg uncertainty principle. They can be viewed as maximizing classical behavior within the quantum realm by minimizing uncertainty. Furthermore, coherent states are Gaussian, allowing for straightforward study and modeling within frameworks that resemble those used for true quantum phenomena in quantum optics experiments. This enables a formal definition and isolation of quantum advantages by comparing them to the benchmark of coherent states.

1.3 Types of radar

Although it is commonly assumed that quantum radar exclusively relies on entanglement and quantum information (QI), this is not necessarily the case. The definition of quantum radar and quantum target detection should be understood more broadly as any detection system that utilizes non-classical components to enhance its capabilities. These non-classical components can take the form of a non-classical transmitter, a non-classical receiver, or both. In essence, there are three main types of quantum sensors [73, 140].

- **Type 1:** Quantum radars and quantum LIDAR systems can transmit non-classical

quantum states of light without relying on entanglement between the transmitter and the receiver. This includes the use of single-photon (Fock state) quantum radars as well as traditional LIDAR systems.

• **Type 2:** In this type of system, classical (coherent) states are transmitted, but quantum receivers are employed to enhance the sensitivity of the detection. This category encompasses any quantum-enhanced LIDAR systems where the use of quantum technology in the receiver allows for improved detection capabilities.

• **Type 3:** Quantum states of light are transmitted, and these states are initially entangled with the receiver.

Type 3 quantum sensors involve the use of entangled sources for applications in quantum radar, sensing, and metrology. In this type, entanglement is created between two modes, with one mode serving as the signal and the other mode, known as the idler, being utilized as part of the receiver, in Fig. 1.2.

1.3.1 Lloyd initial single photon quantum illumination proposal

In 2008, Lloyd introduced [83] the concept of quantum information (QI) as a means to improve the detection of distant objects. He initially argued that quantum bits demonstrate heightened sensitivity in detection procedures when the signal is entangled with an anisotropic medium and the measurement of the turning radiation is entangled with the same medium [111]. In this study, we explore the extent of enhancement in detection capabilities and inquire whether entanglement contributes to improved sensitivity in quantum optical processes. Intuitively, if a lone signal photon is dispatched and becomes entangled with an additional photon, it will either generate or identify the original photon upon its return. This intuition remains accurate, even though noise and loss completely disrupt the correlation between signal and noise.

The study compared two protocols: one using N unentangled single-photon states

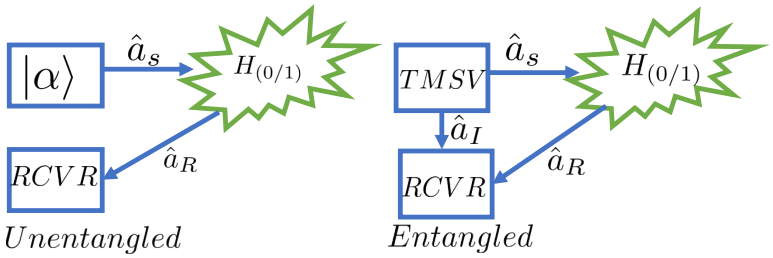

Figure 1.2: Quantum illumination

and the other using two entangled beams (signal and idler). Both scenarios involved illuminating a region of space where a weakly reflecting target could be present or absent, within a thermal background. In both cases, certain assumptions were made.

• Signal comprising N high time-bandwidth product $M = TW \gg 1$, single-photon pulses. Here, T is the detection time window and W is the bandwidth such that the detector can distinguish between M modes per detection event.

• Round-trip transmissivity $0 < \kappa \ll 1$ when the target is present. $\kappa = 0$ when the target is absent.

• Background noise $N_B \ll 1$.

• For each transmitted signal pulse, at most one photon is detected at the receiver such that $MN_B \ll 1$.

These hypotheses led to the identification of two operational regimes "good" and "bad" for the operation of each single-photon and entangled source based on their quantum Chernoff bounds (QCB). The probability of making an error after N trials was discovered to be, in their good regimes,

$$P_{err}^{SP} \leq \frac{1}{2}e^{-\kappa N}, \quad \kappa \gg N_B, \tag{1.9}$$

and

$$P_{err}^{QI} \leq \frac{1}{2}e^{-\kappa N}, \quad \kappa \gg N_B/M. \tag{1.10}$$

In their bad regimes, these bounds are given by

$$P_{err}^{SP} \leq \frac{1}{2}\mathrm{e}^{-\kappa^2 N/8N_B}, \quad \kappa \gg N_B, \tag{1.11}$$

and

$$P_{err}^{QI} \leq \frac{1}{2}\mathrm{e}^{-\kappa^2 NM/8N_B}, \quad \kappa \gg N_B/M, \tag{1.12}$$

resulting in a further expansion of the QI's valid range, with the error probability dramatically decreasing for $M \gg 1$ in comparison to unentangled single-photon sources.

These findings are based on several assumptions that are often unrealistic. Firstly, it assumes the availability of a source that can generate entangled photons with a high time-bandwidth product to probe the target area. Additionally, the receiver is assumed to be optimal, performing an ideal joint measurement on each returning photon and its corresponding idler. Furthermore, it is assumed that the idler storage system remains lossless throughout the entire round-trip time of the signal. These limitations have sparked debates about the feasibility of practical quantum radar systems based on quantum information (QI), and these issues will be discussed in more detail later in the chapter.

It's crucial to remember that Lloyd did not directly compare a quantum scheme with a classical one in his initial comparison. Rather, it contrasted an entanglement-based scheme with a non-entanglement scheme. Even when single photons are used as a source for target detection without entanglement, the data must still be processed and decisions made using quantum photo-detection theory. This method is classified as a Type 1 quantum sensor.

In 2009, Shapiro and Lloyd [121] compared entanglement-based QI to the coherent state, which is currently the standard, at least in the optical domain. The output of an ideal laser can produce minimum-uncertainty classical states, which are discussed in detail in

Chapter 2. The case of a transmitter emitting a coherent state with an average of N photons is covered by the quantum Chernoff bound [134]. This can be accomplished, for instance, by sending a coherent state with an average photon number of unity N times. In this instance, the QCB was found to be

$$P_{err}^{CS} \leq \frac{1}{2}\mathrm{e}^{-N\kappa\left(\sqrt{N_B+1}-\sqrt{N_B}\right)^2}, \quad N_B \geq 0, \tag{1.13}$$

for all values of $0 \leq \kappa \leq 1$ and $N_B \geq 0$. In the low background noise $N_B \ll 1$, this reduces to

$$P_{err}^{CS} \leq \frac{1}{2}\mathrm{e}^{-\kappa N}, \quad N_B \ll 1. \tag{1.14}$$

This output is better than Lloyd's quantum illumination discrete variable transmitter's output in its "bad" regime, and coherent state protocol output is comparable to that transmitter's output in its "good" regime. As of now, no quantum advantage has been identified over the classical benchmark, despite the superior performance of entangled photons compared to their single-photon counterparts.

1.3.2 Gaussian source of Quantum illumination

The findings of Shapiro and Lloyd [121], which indicated limitations in the potential of Quantum Illumination (QI) at the time, did not put an end to research in the field. Tan et al [134]. presented their version of QI at the same time, utilizing a more practical model within the Gaussian state framework. This version, along with the mathematical foundations of Gaussian quantum information and continuous variable theory outlined in Chapter 2, will be the primary focus of this thesis.

Let us consider a resource state that can be represented as a Gaussian two-mode squeezed vacuum (TMSV) state, more details in chapter 2. This state consists of two modes, each containing N_S photons: a signal mode that is sent to a target region and an

idler mode that is kept at the source for a later joint measurement. A few presumptions underlie the Gaussian Quantum Illumination (QI) theory's operation:

• Low-brightness signal $N_S \ll 1$. The signal and idler modes each have an extremely small number of photons.

• High time-bandwidth product, $M = TW \gg 1$.

• Low target reflectivity, $0 \leq \kappa \ll 1$ (with $\kappa = 0$ when the target is absent).

• The average thermal photon number per mode for background noise is extremely high, $N_B \gg 1$.

The Quantum Illumination experimental setup assesses two hypotheses concerning the outcome, as elaborated in Chapter 2. The first hypothesis, labeled H_0, posits the absence of the target, with the returning signal modeled as a noisy background in the form of a thermal state. In this situation, the average number of thermal photons per mode, denoted as N_B, is notably higher ($N_B \gg 1$) than in previous studies, where the assumptions were $N_B \ll 1$ and $MN_B \ll 1$.

The second hypothesis, H_1, corresponds to the presence of a weakly reflective target in the region with a reflectivity parameter $\kappa \ll 1$, indicating a high loss regime.In this scenario, the background is very strong, and the mean number of photons per mode in the return is given by $N_B/(1-\kappa)$. In both cases, the returning signal and the retained idler are no longer entangled.

The decision problem is then focused on distinguishing between the two conditional states, and the ability to do so is quantified by computing various bounds and it will be explained in chapter.2. The choice of a specific bound depends on how the associated costs for different types of errors are weighted. This involves considering symmetric or antisymmetric costing procedures.

Tan et al. adopted the Gaussian state approach with a symmetric cost quantum hypothesis testing (QHT) framework. They determined that the quantum Bhattacharyya bound (QBB) for the quantum information (QI) source takes an asymptotic form.

$$P_{err}^{QI} \leq \frac{1}{2} e^{-M\kappa N_S/N_B} \tag{1.15}$$

in the limits $0 < \kappa \ll 1, N_S \ll 1$ and $N_B \gg 1$.

The statement implies that the coherent state mentioned earlier, which is associated with achieving an optimal classical benchmark, has a Quantum Chernoff Bound (QCB) that can be

$$P_{err}^{CS} \leq \frac{1}{2} e^{-M\kappa N_S(\sqrt{N_B+1}-\sqrt{N_B})^2} \tag{1.16}$$

In the same limitations$0 < \kappa \ll 1, N_S \ll 1$ and $N_B \gg 1$, the coherent-state transmitter QCB is given by

$$P_{err}^{QI} \leq \frac{1}{2} e^{-M\kappa N_S/4N_B} \tag{1.17}$$

In contrast to earlier findings, it is observed that the error exponent of the quantum information (QI) transmitter in this regime has a 4-fold advantage (equivalent to 6 dB) over the corresponding coherent-state transmitter. This means that an optimal QI-based approach provides a 6 dB improvement in the effective signal-to-noise ratio (SNR) compared to coherent light illumination.

Theoretical studies have demonstrated that this 6 dB advantage is maximally achievable when considering optimal collective quantum measurements [29]. However, when restricting the receiver to local operations and classical communications (LOCCs) only, the advantage reduces to 3 dB. It has also been established that the two-mode Gaussian state utilized to achieve these bounds is the optimal quantum state [74].

Additionally, it has been shown that without a quantum memory (the ability to store an idler), the optimal source is a coherent state. Recent research has further demonstrated that this well-known benchmark can be strictly surpassed by employing a squeezed-based protocol where both displacement and squeezing are jointly optimized under a global energy constraint [128].

1.4 Microwave Quantum illumination

Lloyd and Tan et al. conducted research on quantum illumination (QI) that focused on operations in the optical range. They assumed that optical wavelengths would be used, as this is a well-established domain for QI implementation. In the optical range, there are readily available tools such as spontaneous parametric down-conversion (SPDC) sources for generating signals, which naturally produce low-energy modes ($N_S \ll 1$). Additionally, high fidelity single-photon detectors, which have minimal noise associated with their operation and are close to quantum-limited, are widely used.

Lloyd's findings were not affected by this assumption, but Tan et al. discovered a quantum advantage of 6 dB in effective signal-to-noise ratio (SNR) under the assumption that there is a high background mean number of photons per mode ($N_B \gg 1$). However, this assumption does not hold true in the optical wavelength range. In fact, the background mean number of photons per mode (NB) is typically on the order of 10^{-6} or smaller in optical wavelengths.

To address the issue of the low background photon count in the optical domain, a possible solution is to expand the theory of quantum illumination (QI) to the microwave domain [10]. This would take advantage of the naturally occurring thermal microwave background, which provides a background with a high number of photons ($N_B \gg 1$) required for the quantum advantage in QI. Barzanjeh et al. proposes to use an electro-opto-mechanical (EOM) converter for generating an hybrid entangled source with a microwave signal and an optical idler. The microwave signal was then transmitted to the desired target region. Upon its return, another EOM converter was used to reverse the process and convert the microwave signal back into the optical region. A phase-conjugated (PC) joint measurement was performed with the retained optical idler. This microwave extension of QI gained significant attention in the wider scientific community as a potential quantum-mechanical alternative to classical radar. It has the potential to detect stealth tar-

gets while concealing a weak signal within the naturally occurring and strong microwave background.

1.5 Illumination receivers

Creating a receiver for quantum illumination capable of realizing the complete 6 dB enhancement in signal-to-noise ratio (SNR) as predicted by the comprehensive theoretical model presents a significant challenge. In the framework of Gaussian quantum illumination, the operator describing the useful quantum correlation for detecting the target is

$$\hat{O}_{RI}(k) := \hat{a}_{R_k}\, \hat{a}_{I_k}. \tag{1.18}$$

The $k-$th return mode $\hat{a}_{R_k}$ is given by

$$\hat{a}_{R_k} = \sqrt{\eta}\, \hat{a}_{S_k} + \sqrt{1-\eta}\, \hat{a}_{B_k}, \tag{1.19}$$

where $\hat{a}_{S_k}$ is the signal, and $\hat{a}_{I_k}$ idler mode annihilation operator, and $\hat{a}_{B_K}$ is the thermal background noise. Consider the two hypotheses that target absent is H_0 and target present is H_1. The outcome of the cross-correlation is the following: if one sends a two-mode squeezed state (see chapter 2)

$$C_Q^{H_0} = \langle\, \hat{a}_{R_k}\, \hat{a}_{I_k}\, \rangle = 0, \quad C_Q^{H_1} = \langle\, \hat{a}_{R_k}\, \hat{a}_{I_k}\, \rangle = \sqrt{\eta N_S (N_S+1)}. \tag{1.20}$$

Instead, in the case of classically correlated signal and idler modes in the limit $N_S \ll 1$, the cross-correlation is $C_C^{H_1} = \langle\, \hat{a}_{R_k}\, \hat{a}_{I_k}\, \rangle = \sqrt{\eta} N_S$, the value of the quantum correlation exceeds the classical correlation $C_Q > C_C$. In experiments, it is impossible to measure the operator $\hat{O}_{RI}(k)$ directly.

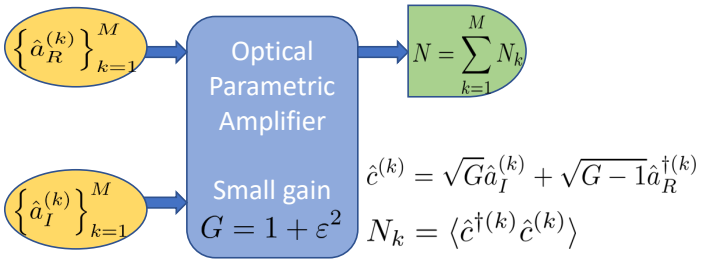

Figure 1.3: Optical parametric amplifier (*OPA*) with gain G, the measurement of the total number of photons, N, is counted. If N is less than a certain threshold η, the receiver collapse to H_0; otherwise, H_1.

1.5.1 Optical parametric amplifier (OPA)

To address the impossibility to measure the phase-sensitive correlation of Eq. (1.20), *Guha* and *Erkmen* [54] proposed a receiver that converts phase-sensitive cross-correlation into photon counting shown in Fig. 1.3.

$$\hat{c}^k = \sqrt{G}\hat{a}_I^{(k)} + \sqrt{G-1}\hat{a}_R^{\dagger(k)}, \tag{1.21}$$

$$\hat{d}^k = \sqrt{G}\hat{a}_R^{(k)} + \sqrt{G-1}\hat{a}_I^{\dagger(k)}, \tag{1.22}$$

where $G = 1 + \varepsilon^2$ is the gain of the *OPA*, $N_k = \langle \hat{c}^{\dagger}_{(k)}\hat{c}_{(k)} \rangle$ counts photons in the amplified idler mode. The mode $\hat{c}_{(k)}$ is in a thermal state under both the H_0 and H_1 hypotheses, $\hat{\rho_c} = \sum_{n=0}^{\infty}[N_m^n/(1+N_m)^{1+n}]|n\rangle\langle n|$, for $m = [0, 1]$, with mean phothon number.

$$\begin{aligned} N_0 &= GN_s + (G-1)(1+N_B), \\ N_1 &= GN_s + (G-1)(1+N_B+\kappa N_s) \\ &\quad + 2\sqrt{G(G-1)}\sqrt{\kappa N_s(N_s+1)}. \end{aligned} \tag{1.23}$$

The best joint quantum measurement for differentiating between the two hypotheses is to count photons on each output mode $c_{(k)}$ and decide between the two hypotheses based on the total photon count N over all M detected modes, using a threshold detector [103].

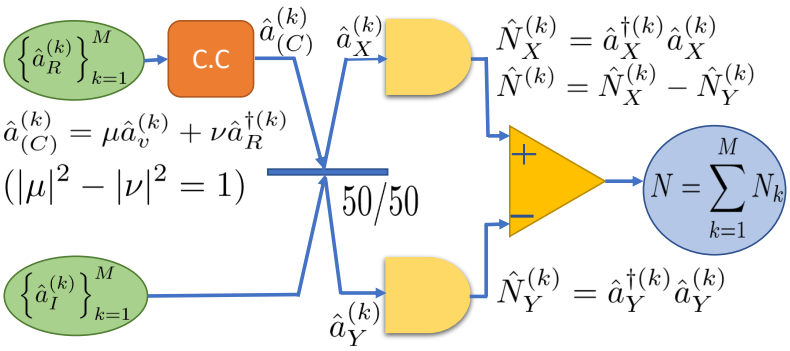

Figure 1.4: The input of the balanced difference detector in the *PCR* are phase-conjugated return and idler modes. The measured total number of photon counts, N, less than a threshold η, the receiver decides H_0; otherwise, H_1.

1.5.2 Phase conjugate receiver (PCR)

Guha and Erkmen's research also presented the idea of utilizing the stored half of the entangled photon pair to perform dual-balanced difference detection after phase-conjugating the returned light. When $N_s \ll 1$, $\kappa \ll 1$, and $N_B \gg 1$ are present, this technique yields the same 3 dB error exponent gain in terms of error probability. It also shows better performance when compared to the OPA (Optical Parametric Amplification) receiver. For $1 \leq k \leq M$, Fig. 1.4 shows the M modes' output from the phase-conjugate receiver.

$$\hat{a}_C^{(k)} = \mu \hat{a}_v^{(k)} + \nu \hat{a}_R^{\dagger(k)}, \tag{1.24}$$

where $\hat{a}_v^{(k)}$ are the vacuum-state operators that secure the commutator. The phase conjugate return and idler modes' outputs are fed into the $50-50$ beam splitter, and the outcome modes are $\hat{a}_X^{(k)} = \left(\hat{a}_C^{(k)} + \hat{a}_I^{\dagger(k)}\right)/\sqrt{2}$ and $\hat{a}_Y^{(k)} = \left(\hat{a}_C^{(k)} - \hat{a}_I^{\dagger(k)}\right)/\sqrt{2}$. The result of the measurement on the unity-gain difference amplifier is,

$$\hat{N}^{(k)} = \hat{N}_X^{(k)} - \hat{N}_Y^{(k)} = \hat{a}_c^{\dagger(k)} \hat{a}_I^{(k)} + \hat{a}_c^{(k)} \hat{a}_I^{\dagger(k)}, \tag{1.25}$$

Where $\hat{N}_X^{(k)} = \hat{a}_X^{\dagger(k)} \hat{a}_X^{(k)}$ and $\hat{N}_Y^{(k)} = \hat{a}_Y^{\dagger(k)} \hat{a}_Y^{(k)}$.

Under hypothesis H_0 [$\hat{a}_C^{(k)} = \mu\hat{a}_v^{(k)} + \nu\hat{a}_R^{\dagger(k)}$], the mode $\hat{a}_c^{(k)}$ and $\hat{a}_I^{(k)}$ are independent and uncorrelated. The decision is based on the sum of the photon counts N over all M modes. The final random variable is $N_T = \sum_{k=1}^{M} N^k$ the N^k are independent, identically distributed (iid) random variables mean and variance given by $\langle N\rangle_0 = 0$ and $\sigma_0^2 = N_s + |\nu|^2(N_B+1)(2N_s+1)$. Under hypothesis H_1 [$\hat{a}_C^{(k)} = \mu\hat{a}_v^{(k)} + \nu\sqrt{\kappa}\hat{a}_s^{\dagger(k)} + \nu\sqrt{1-\kappa}\hat{a}_B^{\dagger(k)}$], $\hat{a}_s$ and $\hat{a}_I$ are in a two-mode squeezed with correlation of the mean and variance are $\langle N\rangle_0 = 2\nu\sqrt{\kappa N_s(N_s+1)}$ and $\sigma_1^2 = N_s + \nu^2\left[(N_B+1)(2N_s+1) + \kappa(2N_s+1)^2 - \kappa(N_s+1)\right]$. Despite the fact that N is not Gaussian in general, we can safely approximate the probability distribution of N with a Gaussian with mean $M\bar{N}_j$ and variance $M\sigma_j^2$ for the two hypotheses, $j = 0, 1$, by using the central limit theorem in the limit $M \gg 1$ that we are assuming. The Gaussian probability distribution function is

$$P_{N|H_{0/1}}(n|H_{0/1}) = \frac{e^{-(n-MN_{0/1})^2/(2M\sigma_{0/1}^2)}}{\sqrt{2\pi M\sigma_{0/1}^2}}. \tag{1.26}$$

In the QI case involving PCR detection, the decision is made by differentiating between two Gaussian distributions, despite the fact that in this instance both the variance and the mean differ between the two cases.

1.6 Experimental studies

The first Quantum Illumination (QI) experiment was carried out by Lopaeva et al [84]. using a 50:50 beam splitter as a model for the target and a spontaneous parametric down-conversion (SPDC) source for photon counting. They demonstrated that, in comparison to a correlated thermal state in a thermal background, an entanglement-breaking channel could achieve a QI-like advantage in effective signal-to-noise ratio (SNR). But employing photon counting with SPDC outputs is a less-than-ideal detection scheme, as previously shown. Furthermore, their choice of the classical benchmark was not the best one ac-

cording to coherent light [36]. Later on Zhang et al [151]. and afterwards used an OPA receiver to put Tan et al.'s Gaussian QI protocol into practice. Their experiment showed a sub-optimal 20% improvement in effective SNR compared to the best classical scheme, which is equivalent to 0.8 dB versus the 3 dB available with OPA receivers.

S. Barzanjeh [10] implemented a digital version of the phase-conjugate receiver in a proof-of-concept Quantum Illumination (QI) experiment in the microwave regime. A Josephson parametric converter (JPC) was used inside a dilution refrigerator to generate entanglement. This method allows the phase-conjugate receiver to be implemented without the use of analog photodetection while fully utilizing the correlations of the JPC output fields. The experiment then compares the signal-to-noise ratio (SNR) with alternative detection strategies at the JPC output, using the same signal path and photon numbers. A Josephson parametric converter (JPC) was used in each of these experiments [10,21,86] to produce entanglement in low-brightness microwave modes. Next, a comparison was made between the obtained results and a radar with classical correlation. Following the JPC's creation of entanglement, the signal was transmitted to the target region and amplified in both modes. Concurrently, the idler was quickly heterodyne identified. The traditional result of this heterodyne detection was digitally saved during post-processing so that it could subsequently be compared to the result of the returning signal that was detected using a heterodyne. A Quantum Illumination (QI)-like advantage over their classical counterparts, which were classically correlated noise radars, was shown in all experiments.

1.7 Thesis outline

The structure of the thesis follows an incremental development, starting with the introduction of the mathematical tools and preliminary concepts necessary for the context of the research. The subsequent chapters are organized based on the publications that present

the contributions made by the research project upon which this thesis is based. These contributions focus on the theory of quantum illumination and quantum target detection, as well as the practical aspects of implementing these concepts, particularly in the microwave domain. Lastly, I will present the theory of entanglement and the synthesis of entangled states using Heisenberg exchange interactions. The thesis is divided into the following chapters:

• **Chapter 2: Preliminary Notations:** This thesis provides a comprehensive overview of the mathematical tools and formalism of continuous variables that are necessary for understanding the subsequent chapters and contributions. The mathematical framework underpinning continuous variables is explained in detail, enabling readers to grasp the essential concepts and techniques used throughout the thesis. These mathematical tools lay the foundation for the exploration and analysis of quantum detection and quantum radar, allowing for a deeper understanding of the research contributions presented in the later chapters.

• **Chapter 3: Publication 1:** At the start of my published research project, Entanglement faces vulnerability to degradation in a noisy sensing environment. Nevertheless, the quantum illumination protocol has surprisingly demonstrated resilience against such conditions, maintaining its advantageous features. However, implementing a measurement system to leverage this advantage proves challenging, given that pertinent information is concealed within weak correlations embedded in noise on the receiver side. Recent progress in correlation-to-displacement conversion modules provides a promising avenue for an optimal protocol in practical microwave quantum illumination. This study extends the conversion module to accommodate common experimental imperfections in microwave systems. To mitigate losses, we propose amplifying the return signals. Under ideal amplification, the entire six-decibel advantage in target detection error can be preserved. However, with noisy amplification, this advantage is reduced to three decibels. We analyze the quantum advantage under various scenarios using a Kennedy receiver in

the final measurement. In the ideal case, performance still achieves optimal results over a significant range with only on-off detection. Photon number-resolving detectors further enhance performance, and their impact is examined using receiver operating characteristic curves. These findings open the door for the practical development of microwave quantum illumination systems.

• **Chapter 4: Introduction of the W state:**

This thesis offers an extensive exploration of the concepts of entanglement and the formalism of qubit representation, which are crucial for comprehending the subsequent chapters and the contributions made. A detailed explanation of the entanglement formalism and qubit representation supporting the generation of the W state is provided, ensuring that readers can comprehend the fundamental principles and methodologies utilized throughout the thesis. These entanglement tools serve as the groundwork for the investigation and examination of the spin system and the synthesis of the many-body W state, facilitating a more profound understanding of the research contributions outlined in the later chapters.

• **Chapter 5: Publication 2:** At the start of my published research project, the phenomenon of entanglement spread holds significant interest, especially in the context of quantum state synthesis. This is particularly relevant when the goal is to transform an initial direct-product state into a highly entangled target state. In devices relying on pairwise exchange interactions, various methods can be employed to optimize this process. As a benchmark scenario, we focus on the challenge of distributing one excitation among N two-level atoms or qubits.

Beginning with an initial state where one qubit is excited, the objective is to achieve a target state where all qubits exhibit the same excitation amplitude—a generalized W-state. This transformation is to be accomplished through suitably chosen pairwise exchange interactions. For instance, in a setup where any pair of qubits can be brought into proximity for a controllable period, we explore three protocols, each with $N-1$ tightly-constrained

steps.

In the first protocol, one atom serves as a flying qubit that sequentially interacts with all others. The second protocol involves qubits interacting pairwise in sequential order. The interaction times in these two cases follow a pattern with an elegant geometric interpretation, corresponding to angles within the spiral of Theodorus—a construction known for over two millennia. The third protocol adopts a divide-and-conquer approach, distributing equally between two qubits at each step.

For large N, the flying-qubit protocol results in a total interaction time scaling as $\sqrt{N}$, while the sequential approach scales linearly with N. The divide-and-conquer approach, on the other hand, has a time lower bound that scales as $\ln N$. Regardless of the protocol, we demonstrate that the phase differences in the final state cannot be independently controlled. For instance, generating a W-state (where all phases are equal) is not achievable through pairwise exchange.

- **Chapter 6: Summary and Conclusion**

Chapter 2

Preliminary Notations

2.1 Introduction

The aim of this chapter is to introduce important definitions and tools that will be used throughout the thesis work. Specifically, Sec. 2.2 covers Gaussian states, which play a fundamental role in many aspects of continuous variable quantum information.

Sec. 2.2.1 discusses the generation and properties of bosonic Gaussian states, including coherent states, two mode squeezed states, and thermal states, which are used in many protocols and enter into the description of quantum illumination which we will study in the following. Sec. 2.3 also introduces quantum hypothesis testing, which is used to evaluate the performance of quantum detection schemes.

Finally, Sec. 2.4 explains the Gaussian positive operator value measurement (POVM) and General-dyne measurement. For readers interested in more details, references and books on continuous variable quantum systems and quantum optics are provided.

2.2 Continuous variable systems, harmonic oscillators and bosonic modes

This section provides an overview of fundamental concepts of continuous variable systems (CV) and notation that will be used throughout the thesis. It begins by examining the Cartesian decomposition of mode operators and phase-space variables. The concept of characteristic function and Wigner function is then introduced. Additionally, the significance of symplectic transformations in describing Gaussian operations in the phase-space is emphasized.

2.2.1 Bosonic modes

The Hamiltonian of a bosonic system corresponding to a single mode of radiation is represented by a harmonic oscillator, with each mode labeled by k [15, 41, 145].

$$\hat{H}_k = \hbar\omega_k \left(\hat{a}_k^\dagger \hat{a}_k + \frac{1}{2}\right). \tag{2.1}$$

The additional $1/2$ term arises from the zero-point energy fluctuations that are associated with the vacuum state, where the photon number operator $\hat{n}_k = \hat{a}_k^\dagger \hat{a}_k$ equals zero. Here, $\hbar\omega_k$ represents the quantization energy of a single photon.

The Fock basis $|n_k\rangle_{n=0}^{\infty}$, which is also known as the number state representation, denotes the orthonornormal set of eigenstates of the photon number or $\hat{n}_k$. These states represent the set of all possible number state vectors for the mode k, where n_k indicates the number of field excitations present in mode k. The bosonic annihilation and creation operators are represented by $\hat{a}_k$ and $\hat{a}_k^\dagger$, respectively, and they are defined by their action on the Fock basis

$$\hat{a}_k |0\rangle = 0, \quad \hat{a}_k |n\rangle_k = \sqrt{n}\, |n-1\rangle_k, \quad (\text{for} \quad n \geq 1), \tag{2.2}$$

specifying the vacuum state as well, and

$$\hat{a}_k^\dagger \, |n\rangle_k = \sqrt{n+1} \, |n+1\rangle_k, \quad (\text{for} \quad n \geq 0) \, . \tag{2.3}$$

The definitions of annihilation and creation operators for bosonic quantum fields demonstrate that the former removes a particle, whereas the latter adds one. These definitions are consistent with the well-known bosonic commutation relation.

$$\left[\hat{a}_k, \hat{a}_l^\dagger\right] = \delta_{kl}. \tag{2.4}$$

We can easily generalize this formalism to describe a system of N modes, with pairs of bosonic field operators, denoted by $\{ \hat{a}_k, \hat{a}_k^\dagger \}_{k=1}^N$, and a tensor product of infinite-dimensional Hilbert space $\mathcal{H}^{\otimes N} = \otimes_{k=1}^N \mathcal{H}_k$.

The free Hamiltonian of the system (non interacting modes) is given by

$$\hat{H}_k = \sum_{k=1}^{N} \hbar\omega_k \left(\hat{a}_k^\dagger \hat{a}_k + \frac{1}{2}\right). \tag{2.5}$$

Position and momentum-like operators for each mode are defined through the Cartesian decomposition of the mode operators,

$$\hat{q}_k := \left(\hat{a}_k + \hat{a}_k^\dagger\right), \quad \hat{p}_k := i\left(\hat{a}_k^\dagger - \hat{a}_k\right), \tag{2.6}$$

satisfying the commutation relations.

$$[\hat{q}_l, \hat{p}_k] = 2i\delta_{lk}. \tag{2.7}$$

We can group together the canonical operators in the vector

$$\hat{\mathbf{X}} = (\hat{q}_1, \hat{p}_2, \ldots, \hat{q}_n, \hat{p}_n)^{\mathbf{T}}, \tag{2.8}$$

which allows us to write in compact form the bosonic commutation relationships between the quadrature phase operators,

$$\left[\hat{X}_i, \hat{X}_l\right] = 2i\Omega_{ij}, \quad (i, j = 1, \ldots, 2N), \tag{2.9}$$

where Ω_{ij} is the symplectic $2N \times 2N$ matrix, defined as the direct sum of identical 2×2 blocks:

$$\Omega := \bigoplus_{k=1}^{N} \omega = diag(\omega, \ldots, \omega), \quad \omega = \begin{pmatrix} 0 & 1 \\ -1 & 0 \end{pmatrix}. \tag{2.10}$$

2.2.2 Phase-space representation

The density operator $\hat{\rho}$ represents the quantum state of an N-mode bosonic system and encodes all of its physical information in its phase-space Wigner distribution which we can define as follows [99, 144].

Given a state $\hat{\rho}$, and the Weyl displacement operator

$$D(\xi) := \exp\left(i\hat{\mathbf{X}}^{\mathbf{T}}\Omega\xi\right), \tag{2.11}$$

where $\xi \in \mathbf{R}^{2N}$, we can define the Wigner (or symmetrically ordered) characteristic function $\chi(\xi)$ as

$$\chi(\xi) := \mathrm{Tr}\left[\hat{\rho}D(\xi)\right]. \tag{2.12}$$

Then, the Wigner function $W(\mathbf{X})$, is a quasi-probability distribution defined over a $2N$-dimensional phase space, which can be obtained by taking the Fourier transform of the

characteristic function associated to the density operator $\hat{\rho}$,

$$W(\mathbf{X}) = \int_{\mathbf{R}^{2N}} \frac{d^{2N}\xi}{(2\pi)^{2N}} \exp\left(-i\mathbf{X}^{\mathbf{T}}\Omega\xi\right)\chi(\xi), \tag{2.13}$$

where $\mathbf{X}^{\mathbf{T}} = (q_1, p_1, \ldots, q_N, p_N) \in \mathbf{R}^{2N}$. The Wigner function is defined on the real symplectic phase space $\mathbf{K} := \left(\mathbf{R}^{2N}, \Omega\right)$, where Ω is the symplectic form. The continuous variables $\mathbf{X} \in \mathbf{R}^{2N}$ span this space.

The vector of first order moments, i.e., the mean values, is represented by the displacement vector.

$$\bar{\mathbf{X}} := \langle\hat{\mathbf{X}}\rangle = \mathrm{Tr}\left(\hat{\rho}\hat{\mathbf{X}}\right) = \int d^{2N}X W(\mathbf{X})\,\mathbf{X}. \tag{2.14}$$

The covariance matrix (CM) $\mathbf{V}$ is a representation of the second moment or covariance of the canonical variables. The elements of this matrix are given by:

$$\mathbf{V}_{ij} := \frac{1}{2}\mathrm{Tr}\left(\left\{\Delta\hat{X}_i, \Delta\hat{X}_j\right\},\ \hat{\rho}\right), \tag{2.15}$$

where $\Delta\hat{X}_i := \hat{X}_i - \langle\hat{X}_i\rangle$. The diagonal elements of the covariance matrix, denoted by $\mathbf{V}_{ii} = \mathbf{V}(\hat{X}_i)$ and $\mathbf{V}\left(\hat{X}_i\right) := \langle\hat{X}_i^2\rangle - \langle\hat{X}_i\rangle^2$, represent the variances of each individual quadrature operator. The symbol $\{\ldots\}$ refers to the anti-commutator.

For canonically conjugate variables, the Heisenberg uncertainty relations can be recast as a constraint on the covariance matrix (CM) $\hat{\mathbf{V}}$ [32, 126],

$$\mathbf{V} + i\,\mathbf{\Omega} \geq 0. \tag{2.16}$$

This pasitivity condition implies the typical Heisenberg relation for position and momentum,

$$V(\hat{q}_k)V(\hat{p}_k) \geq 1. \tag{2.17}$$

The inequality of Eq. (2.16) represent a necessary condition for the covariance matrix

of any quantum state in order to be physically acceptable.

For a specific class of states, the first and second order moments are sufficient for their complete characterization, i.e., we can write $\hat{\rho} = \hat{\rho}\left(\bar{\mathbf{X}}, \mathbf{V}\right)$. This is the case of the Gaussian states. By definition, these are bosonic states with Gaussian Wigner representations (χ or W), i.e.,

$$\chi(\xi) = \exp\left[-\frac{1}{2}\xi^{\mathbf{T}}\left(\Omega\mathbf{V}\Omega^{\mathbf{T}}\right)\xi - i\left(\Omega\bar{\mathbf{X}}\right)^{\mathbf{T}}\xi\right], \tag{2.18}$$

or

$$W(X) = \frac{1}{(2\pi)^N\sqrt{\det\mathbf{V}}}\exp\left[-\frac{1}{2}\left(\mathbf{X}-\bar{\mathbf{X}}\right)^{\mathbf{T}}\mathbf{V}^{-1}\left(\mathbf{X}-\bar{\mathbf{X}}\right)\right]. \tag{2.19}$$

It is interesting to note that a pure state is Gaussian if and only if its Wigner function in non-negative, that is, the only pure states with non-negative Wigner function are Gaussian states.

Moreover, the Heisenberg inequality Eq. (2.16) becomes a necessary and sufficient condition for a Gaussian state to be physically acceptable. Williamson's theorem [118], is an essential tool for manipulating Gaussian states. According to this theorem, it is possible to find a symplectic matrix $\mathbf{S}$ (that is, such that $\mathbf{S}^{\mathbf{T}}\Omega\mathbf{S} = \Omega$), such that any covariance matrix $\mathbf{V}$ can be transformed into its Williamson form.

$$\mathbf{V} = \mathbf{S}\mathbf{W}\mathbf{S}^{\mathbf{T}}, \tag{2.20}$$

where,

$$\mathbf{W} = \bigoplus_{k=1}^{N} \nu_k\mathbf{I}, \quad \mathbf{I} = diag(1,1). \tag{2.21}$$

The collection of symplectic eigenvalues $\{\nu_1, \ldots, \nu_N\}$ represents the symplectic spectrum of the matrix $\mathbf{V}$, while the matrix $\mathbf{W}$ denotes the Williamson form of $\mathbf{V}$. The uncertainty principle implies that each symplectic eigenvalue must satisfy the condition $\nu_k \geq 1$. Moreover, if all symplectic eigenvalues are equal to 1, then the corresponding Gaussian state is pure.

For example: a two-mode Gaussian state's symplectic spectra can be determined by using its first and second-order moments. The state's covariance matrix (CM) can be represented in a block form to facilitate this calculation.

$$\mathbf{V} = \begin{pmatrix} \mathbf{A} & \mathbf{C} \\ \mathbf{C}^{\mathbf{T}} & \mathbf{B} \end{pmatrix}, \tag{2.22}$$

where $\mathbf{A} = \mathbf{A}^{\mathbf{T}}$, $\mathbf{B} = \mathbf{B}^{\mathbf{T}}$ and $\mathbf{C}$ are 2×2 real matrices. Then, the Williamson form is simply $\mathbf{W}^{\oplus} = (\nu_{-}\mathbf{I}) \bigoplus (\nu_{+}\mathbf{I})$, where the symplectic spectrum $\{\nu_{-}, \nu_{+}\}$ is given by

$$\nu_{\pm} = \sqrt{\frac{\Delta \pm \sqrt{\Delta^2 - 4\,\mathbf{det}(\mathbf{V})}}{2}}, \tag{2.23}$$

where Δ is defined as $\Delta := \mathbf{det}(\mathbf{A}) + \mathbf{det}(\mathbf{B}) + 2\,\mathbf{det}(\mathbf{C})$. In this two-mode case, the uncertainty principle can be expressed in terms of the bona-fide conditions.

$$\mathbf{V} > 0, \quad \text{and} \quad \Delta \leq 1 + \mathbf{det}(\mathbf{V}). \tag{2.24}$$

The CM of a generic two-mode Gaussian state of Eq. (1.22) can always be put, by means of a proper symplectic transformation, into its "standard form",

$$\mathbf{V}_{SF} = \begin{pmatrix} a\mathbf{I} & \mathbf{C} \\ \mathbf{C} & b\mathbf{I} \end{pmatrix}, \quad \mathbf{C} = \begin{pmatrix} c_1 & 0 \\ 0 & c_2 \end{pmatrix}. \tag{2.25}$$

When $c_1 = -c_2 = c \geq 0$, the symplectic eigenvalues can be simply obtained as $\nu_{\pm} = \frac{1}{2}\left(\sqrt{y} \pm (b-a)\right)$, where y is given by $(a+b)^2 - 4c^2$. The symplectic transformation $\mathbf{S}$ for

arriving at the standard form in this special case, that is $\mathbf{V}_{SF} = \mathbf{SVS^T}$, is given by

$$\mathbf{S} = \begin{pmatrix} \omega_+\mathbf{I} & \omega_-\mathbf{Z} \\ \omega_-\mathbf{Z} & \omega_+\mathbf{I} \end{pmatrix}, \quad \omega_\pm = \sqrt{\frac{a+b \pm \sqrt{y}}{2\sqrt{y}}}. \tag{2.26}$$

The following text aims to provide the reader with a general understanding of the essential examples of Gaussian states used in quantum illumination, which will be frequently mentioned in this thesis.

2.2.3 Coherent State

A coherent state is just obtained as a phase-space-displaced vacuum Fock state,

$$|\alpha\rangle = \hat{D}(\alpha)\ |0\rangle, \tag{2.27}$$

where $\hat{D}(\alpha)$ is a displacement operator

$$\hat{D}(\alpha) = \exp\left(\alpha\hat{a}^\dagger - \alpha^*\hat{a}\right). \tag{2.28}$$

Coherent states $|\alpha\rangle$ are characterized by a complex amplitude $\alpha = (q + ip)/2$, as shown in Fig. 2.1. These states are eigenfunctions of the annihilation operator $\hat{a}$ with eigenvalue α. As a consequence of its definition, a coherent state has the same covariance matrix of the vacuum state ($\mathbf{V} = \mathbf{I}$) and mean values $X = (q, p)^\mathbf{T}$.

The coherent state represents the classical state of a radiation field which can be generated by a standard coherent radiation source such as a laser. It represents the state of the radiation which is sent to a target in order to verify its presence in a classical illumination scenario.

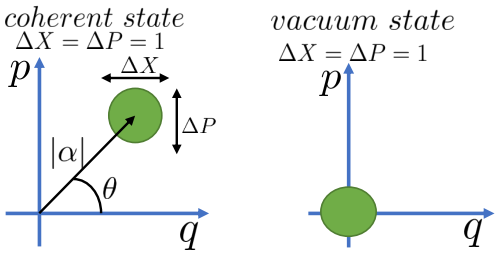

Figure 2.1: Depicts the vacuum state and the coherent state.

2.2.4 Photon statistics of coherent states

The coherent states $|\alpha\rangle$ can be expressed as a sum of number states $|n\rangle$ with complex coefficients given by the Poisson distribution. This expansion allows us to calculate the expectation value of the photon number $\hat{n} = \hat{a}^{\dagger}\hat{a}$ in a coherent state, which turns out to be equal to the square of the coherent state amplitude, $\langle\hat{n}\rangle = |\alpha|^2$,

$$\langle\alpha|\hat{n}|\alpha\rangle = |\alpha|^2 = \bar{n}.$$

The probability of observing a certain number of photons, n, in a coherent state $|\alpha\rangle$ is given by

$$P_n = |\langle n|\alpha\rangle|^2 = e^{-|\alpha|^2}\frac{|\alpha|^{2n}}{n!} = e^{-\bar{n}}\frac{\bar{n}^n}{n!}, \tag{2.29}$$

which corresponds to a Poisson-distribution with mean number of photons $\bar{n} = |\alpha|^2$.

2.2.5 Thermal State

Thermal states define the state in which the mode is at thermal equilibrium T, $\hat{\rho} \propto \exp(-\beta\hat{H})$, where $\beta = 1/K_B T$,

$$\hat{\rho}(T) = \sum_{n=1}^{\infty}\frac{N_T^n}{(N_T+1)^{n+1}}|n\rangle\langle n|, \tag{2.30}$$

where the average number of photons N_T,

$$N_T = \left[\exp\left(\frac{\hbar\omega}{K_B T}\right) - 1\right]^{-1} \equiv \mathrm{Tr}\left[\hat{a}^\dagger \hat{a}\hat{\rho}\right]. \tag{2.31}$$

Thermal states are Gaussian states with a Wigner function with mean $\langle X\rangle = (0,0)$ and a covariance matrix $\mathbf{V} = (2N_T + 1)\,\mathbf{I}_{2\times 2}$. While at room temperature, $N_T \approx 0$ for optical frequencies, it is significantly greater than one for microwave frequencies. In quantum illumination, thermal states are used to describe the noise background, which is therefore always very large in microwave radar applications. This explains why in most QI studies one focuses only onto the case $N_T \gg 1$.

2.2.6 Single mode Squeezed State

When a bright laser is used to pump a nonlinear crystal, some of the pump photons at frequency 2ω are split into pairs of photons at frequency ω. When the conditions for a degenerate optical parametric amplifier (OPA) are met, the output mode ideally consists of a superposition of even-number states ($|2m\rangle$). To generate photon pairs, the interaction Hamiltonian must include a term $\hat{a}^{\dagger 2}$ to create pairs of photons and a term $\hat{a}^2$ to ensure Hermiticity. This interaction is associated with the one-mode squeezing operator, which is a Gaussian unitary transformation defined as

$$\hat{S}(r) = \exp\left[\frac{1}{2}\left(r^*\hat{a}^2 - r\hat{a}^{\dagger 2}\right)\right], \tag{2.32}$$

where $r = |r|e^{i\theta}$ is called the squeezing parameter. Its action the operators $\hat{a}$ and $\hat{a}^\dagger$ is the following linear transformation

$$\begin{aligned} \hat{a} &\to S^\dagger(r)\hat{a}S(r) = \mu\hat{a} - \nu a^\dagger, \\ \hat{a}^\dagger &\to S^\dagger(r)\hat{a}^\dagger S(r) = \mu\hat{a}^\dagger - \nu^* a, \end{aligned} \tag{2.33}$$

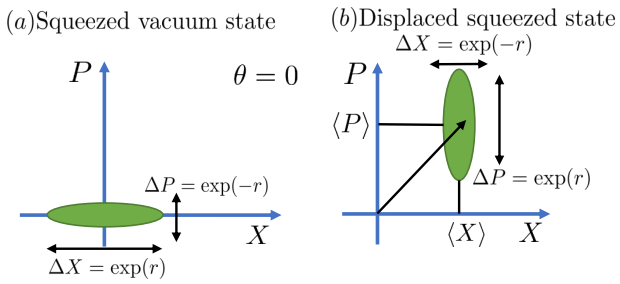

Figure 2.2: Single mode: (a) Squeezed vacuum state and (b) displaced squeezed state

where

$$\mu = \cosh(|r|), \quad \nu = e^{i\theta}\sinh(|r|). \tag{2.34}$$

By applying the squeezing operator to the vacuum state we generate a squeezed vacuum state $|r,0\rangle = S(r)|0\rangle$, as shown in Fig. 2.2, whose covariance matrix (in the special case $\theta = 0$) is given by

$$\mathbf{V} = \begin{pmatrix} e^{-2r} & 0 \\ 0 & e^{2r} \end{pmatrix}. \tag{2.35}$$

This covariance matrix exhibits varying quadrature noise-variances, meaning that one variance is squeezed below the quantum shot-noise level, while the other variance is anti-squeezed and exceeds the shot-noise level.

2.2.7 Two mode Squeezed State

A two-mode squeezed state is a quantum state that can exist between two electromagnetic field modes, such as two optical modes in a cavity. This state is achieved through a process called parametric down-conversion, where a nonlinear crystal is irradiated with a strong pump beam. In the non-degenerate optical parametric amplifier (OPA) regime, we generate pairs of photons in two distinct modes, namely the idler and the signal.

The squeezing parameter characterizes the amount by which fluctuations in one mode

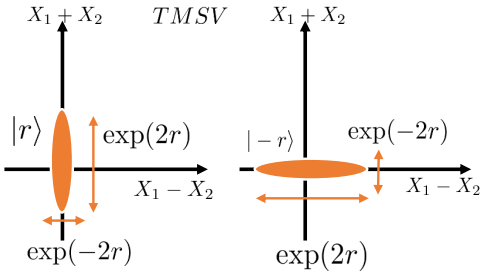

Figure 2.3: Two mode: Squeezed vacuum state

are reduced at the expense of the other mode, as shown in Fig. 2.3. The squeezing parameter can be changed by altering the pump beam or the nonlinear crystal. The process can be described by a bilinear interaction Hamiltonian, and the corresponding Gaussian unitary operator is known as the "two-mode squeezing operator" (TMS). The TMS is defined as follows:

$$\hat{Q}(r) = \exp\left[r\hat{a}^{\dagger}\hat{b}^{\dagger} - r^{*}\hat{a}\hat{b}\right], \tag{2.36}$$

where again $r = |r|\exp(i\theta)$ is the squeezing parameter, which now quantifies the degree of two-mode squeezing in a two-mode squeezed state.

Applying the two-mode squeezing transformation $Q(r)$ to the vacuum state of both modes results in the two-mode squeezed vacuum state (TMSV),

$$\hat{Q}(r)|0,0\rangle = \sqrt{1-\lambda^2}\sum_{n=0}^{\infty}\left(e^{i\theta}\lambda\right)^{n}|n\rangle_S|n\rangle_I, \tag{2.37}$$

where $\lambda = \tanh|r| \in [0,1]$.

It is easy to verify from Eq. (2.37) that the mean number of photons of the idler and signal modes is the same, and it is given by

$$\langle a^{\dagger}a\rangle = \langle b^{\dagger}b\rangle = \sinh^2|r| = N_s. \tag{2.38}$$

The two mode squeezed vacuum state is a Gaussian states with zero mean $\langle X \rangle = 0$ and covariance matrix $\mathbf{V}$

$$\mathbf{V} = \begin{pmatrix} \nu\mathbf{I} & \sqrt{\nu^2 - 1}\mathbf{Z} \\ \sqrt{\nu^2 - 1}\mathbf{Z} & \nu\mathbf{I} \end{pmatrix}, \tag{2.39}$$

where $\nu = \cosh 2r$ measures the quadrature's noise variance.

2.3 Quantum Hypothesis testing

Quantum state discrimination mirrors the statistical problem of hypothesis testing in the quantum realm. The objective is to differentiate between two arbitrary quantum states after they have undergone a quantum channel [20, 104]. This task involves identifying which version of a quantum state aligns with a specific hypothesis. Accuracy and a low error rate in this process are vital for selecting the correct hypothesis.

In the realm of quantum illumination theory, the challenge is to detect the presence or absence of a target based on measurements from a quantum channel's output. This can be tackled using either the asymmetric hypothesis testing approach (Neyman-Pearson method) or the symmetric hypothesis testing method employing the Bayes criterion. Both methods aim to enhance the precision of quantum state discrimination.

2.3.1 Bayes Symmetric Hypothesis test

In a Bayes test, two fundamental assumptions are made [60]. Firstly, prior probabilities, $P_1(\mathbf{R})$ and $P_0(\mathbf{R})$, are assigned to the hypotheses H_1 (target present) and H_0 (target absent) respectively. These probabilities reflect the observer's knowledge of the source before conducting the experiment. Secondly, each possible action incurs a specific cost. The costs associated with the four potential actions are denoted as C_{00}, C_{10}, C_{01}, and C_{11}, where the first subscript signifies the chosen hypothesis and the second subscript indicates

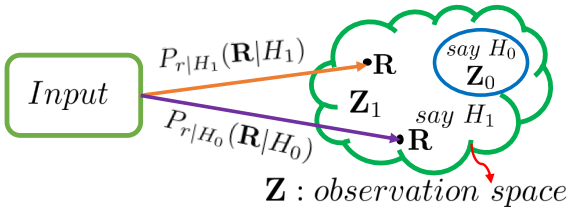

Figure 2.4: Hypothesis test

the true hypothesis.

The expected cost, often denoted as the risk R, quantifies the anticipated cost of making an incorrect decision depending on the chosen hypothesis. To calculate the risk, one multiplies the cost of each potential action by its respective probability and then sums up these values. By comparing the risks associated with different decisions, it is possible to identify the optimal course of action. Mathematically, the risk is expressed as follows:

$$\begin{aligned} R = C_{00}\, P_0 \int_{\mathbf{Z}_0} P\,(r|H_0)\; dr + C_{10}\, P_0 \int_{\mathbf{Z}_1} P\,(r|H_0)\; dr \\ + C_{01}\, P_1 \int_{\mathbf{Z}_0} P\,(r|H_1)\; dr + C_{11}\, P_1 \int_{\mathbf{Z}_1} P\,(r|H_1)\; dr, \end{aligned} \tag{2.40}$$

where r represents a real observable $\mathbf{r} \in \mathbf{Z}$ a set of N observations: $\mathbf{r} = \{r_1, r_2, \ldots r_N\}$. Each set can be conceptualized as a point in an N-dimensional space, denoted as $\mathbf{r} := [r_1, r_2, \ldots, r_N]^{\mathbf{T}}$.

The decision space $\mathbf{Z}$ is a real space, and it is divided into two regions, $\mathbf{Z}_0$ and $\mathbf{Z}_1$, for the purpose of choosing between the two hypotheses, H_0 and H_1, as shown in Fig. 2.4. If $\mathbf{R}$ belongs to $\mathbf{Z}_0$, we conclude that H_0 is valid. Conversely, if $\mathbf{R}$ belongs to $\mathbf{Z}_1$, we conclude that H_1 is valid. The way in which the regions $\mathbf{Z}_0$ and $\mathbf{Z}_1$ are constructed to minimize the error in determining which hypothesis is correct is known as the decision strategy.

We can express risk in an equivalent way by saying that

$$\begin{aligned} R = {} & C_{00}\, P_0\, \mathrm{Pr}_1\,(\text{say } H_0|H_0 \text{ true}) + C_{10}\, P_0\, \mathrm{Pr}_2\,(\text{say } H_1|H_0 \text{ true}) \\ & + C_{11}\, P_1\, \mathrm{Pr}_3\,(\text{say } H_1|H_1 \text{ true}) + C_{01}\, P_1\, \mathrm{Pr}_4\,(\text{say } H_0|H_1 \text{ true})\,. \end{aligned} \tag{2.41}$$

In the context of hypothesis testing, the outcomes can be classified as either correct decisions or errors. Mistakes or errors include type-I and type-II errors, which are represented by outcomes 2 and 4 respectively, while outcomes 1 and 3 represent correct decisions.

In the case of quantum illumination, H_0 indicates the absence of a target, and H_1 represents the presence of a target. The decision strategy is particularly useful in situations where false alarms (type-I errors) and miss detection (type-II errors) occur, corresponding to outcomes 2 and 4 respectively.

$$\begin{aligned} P_F &= P(H_1|H_0) = \mathrm{Pr}_2\,(\text{say } H_1|H_0 \text{ true})\,, \\ P_M &= P(H_0|H_1) = \mathrm{Pr}_4\,(\text{say } H_0|H_1 \text{ true})\,. \end{aligned} \tag{2.42}$$

Consider a simple experiment with binary outcomes. The positive and negative outcomes will be represented by the null hypothesis, H_0, and the alternative hypothesis, H_1. Let $p = \{p_\mu \mid \mu \in \{0, 1\}\}$ be the prior probability of hypothesis H with 0 and 1 such that

$$\begin{aligned} H_0 \;:\quad & \hat{\rho} = \hat{\rho}_0, \quad p = p_0, \\ H_1 \;:\quad & \hat{\rho} = \hat{\rho}_1, \quad p = p_1. \end{aligned} \tag{2.43}$$

The probability of receiving a false positive or false negative result in our determination is then given by

$$\begin{aligned} P\,(\mu = 1 \mid \hat{\rho} = \hat{\rho}_0) &= P\,(H_1|H_0)\,, \\ P\,(\mu = 0 \mid \hat{\rho} = \hat{\rho}_1) &= P\,(H_0|H_1)\,. \end{aligned} \tag{2.44}$$

The probability of getting an error, of any kind, in our discrimination process is overall

$$P_{err} = p_1 \, P(H_0 \mid H_1) + p_0 \, P(H_1 \mid H_0) \, . \tag{2.45}$$

In the realm of quantum mechanics, where it's impossible to perfectly distinguish between non-orthogonal states, various metrics have been devised to measure the distinctions between these states. One of these metrics is minimum error discrimination, which permits the imperfect differentiation of non-orthogonal states by accounting for the probability of making errors.

In the context of quantum hypothesis testing, the two hypotheses correspond to two possible quantum system states, ρ_0 and ρ_1. Bob performs a dichotomous POVM on this system with Π_μ and $\mu = 0, 1$ as its value. The objective is to minimize the error probability in quantum state discrimination using Bob's POVM $\{\Pi_0, \Pi_1\}$,

$$P_{err} = p_0 \mathrm{Tr}\left(\Pi_1 \, \hat{\rho}_0\right) + p_1 \mathrm{Tr}\left(\Pi_0 \, \hat{\rho}_1\right) . \tag{2.46}$$

2.3.2 Helstrom Bound

The Helstrom bound is a method to determine how well Bob can differentiate between two states, $\hat{\rho}_0$ and $\hat{\rho}_1$, with probabilities p_0 and p_1, respectively, while minimizing the probability of error. In other words, it helps Bob to determine the optimal way to distinguish between two quantum hypotheses. Let us define the Helstrom matrix γ.

$$\gamma := p_0 \, \hat{\rho}_0 - p_1 \, \hat{\rho}_1, \tag{2.47}$$

whose spectral decomposition in terms of its eigenvalues and eigenvectors is

$$\gamma = \sum_\mu \gamma_\mu |\mu\rangle\langle\mu|. \tag{2.48}$$

The optimal POVM for Bob, denoted by $\{\Pi_0, \Pi_1 = \mathbf{I} - \Pi_0\}$, consists of a projector Π_0 onto the positive part of the Helstrom matrix, denoted as γ_+. This POVM is referred to as the "Helstrom POVM." To construct this optimal detection scheme, we use the spectral decomposition of the Helstrom matrix and define the POVM $\{\Pi_0, \Pi_1 = \mathbf{I} - \Pi_0\}$, where Π_0 is the projector

$$P(\gamma_+) = \sum_{\gamma_\mu^+} |\mu\rangle\langle\mu|, \tag{2.49}$$

onto the eigenspace associated to the positive positive eigenvalues γ_+ of γ. The minimum probability of error is,

$$P_{err}^{min} = \frac{1}{2}\left(1 - \|\gamma\|_1\right), \tag{2.50}$$

where

$$\|\gamma\|_1 = \mathrm{Tr}|\gamma|, \quad |\gamma| = \sum_\mu |\gamma_\mu|\, |\mu\rangle\langle\mu|. \tag{2.51}$$

From this point forward, we assume that the probabilities of the two states $\hat{\rho}_0$ and $\hat{\rho}_1$ are equal, i.e., $p_0 = p_1 = 1/2$. This implies that both quantum hypotheses are equiprobable.

$$\begin{aligned} H_0 \ : \quad & \hat{\rho} = \hat{\rho}_0, \quad p_0 = \frac{1}{2}, \\ H_1 \ : \quad & \hat{\rho} = \hat{\rho}_1, \quad p_1 = \frac{1}{2}. \end{aligned} \tag{2.52}$$

In this case the Helstrom matrix is given by

$$\gamma = \frac{1}{2}\left(\hat{\rho}_0 - \hat{\rho}_1\right). \tag{2.53}$$

The minimum error probability takes the form

$$P_{err}^{min} = \frac{1}{2}\left[1 - \|\frac{1}{2}\left(\hat{\rho}_0 - \hat{\rho}_1\right)\|_1\right] = \frac{1}{2}\left[1 - D(\rho_0,\, \rho_1)\right]. \tag{2.54}$$

The formula for the Helstrom bound can be used to determine the minimum error probability $P_{err}^{\min}$ in distinguishing between two equiprobable pure states (kets) $|\varphi_0\rangle$ and $|\varphi_1\rangle$. For $D = 0$, the two states are the same and $P_{err}^{min} = 1/2$ (random guessing), while for $D = 1$, the two states are orthogonal and $P_{err}^{min} = 0$ (perfect discrimination).

2.3.3 Quantum chernoff Bound (QCB)

The Helstrom bound can sometimes be challenging to calculate [7], but there are alternative bounds that can give an approximation of the minimum error probability P_{min}^{err}. The most significant of these is the quantum Chernoff (QC) bound, which provides an upper bound.

$$P_{\text{err}}^{\min} \leq P_{QC}, \tag{2.55}$$

which is defined as

$$P_{QC} := \frac{1}{2} \inf_{s \in [0,1]} C_s, \tag{2.56}$$

where the generalized overlap C_s is given by

$$C_s := \text{Tr}\left(\rho_0^s \rho_1^{1-s}\right). \tag{2.57}$$

Due to the possibility of discontinuities in the generalized overlap C_s at the border points $s = 0, 1$ where $C_0 = C_1 = 1$, the QC bound is defined using an infimum in $[0, 1]$ rather than a minimum. When one of the two states is pure, this does indeed occur. For instance, suppose we

$$\rho_0 = |\varphi_0\rangle\langle\varphi|, \tag{2.58}$$

then

$$\inf_s C_s = \lim_{s\to 0^+} C_s. \tag{2.59}$$

Furthermore, in this special case, the QC bound is directly related to the quantum fidelity by the formula

$$P_{QC} = \frac{1}{2} F\left(|\varphi_0\rangle,\ \rho_0\right), \tag{2.60}$$

where

$$F\left(|\varphi_0\rangle, \rho_0\right) = \langle\ \varphi_0\ |\ \rho_1\ |\ \varphi_0\ \rangle. \tag{2.61}$$

2.3.4 Quantum Battacharyya Bound

The Quantum Battacharyya Bound (QB) bound is obtained by setting $s = 1/2$ and ignoring the minimization. This simplification makes the bound easier to compute and useful in discriminating mixed states.

$$P_{QC} \leq P_{QB} := \frac{1}{2} C_{\frac{1}{2}} = \frac{1}{2} \mathrm{Tr}\left[\ \sqrt{\rho}_0\ \sqrt{\rho}_1\right]. \tag{2.62}$$

Fidelity Bounds

Quantum fidelity is a measure of the similarity between two quantum states, given by the square root of the overlap between them. It is defined as follows:

$$F = \left[\mathrm{Tr}\left(\ \sqrt{\sqrt{\rho}_0\ \rho_1\ \sqrt{\rho}_0}\ \right)\right]^2, \tag{2.63}$$

where ρ_1 and ρ_2 are two quantum states. Fidelity satisfies the following properties: $0 \leq F(\rho_1,\ \rho_2) \leq 1$, where $F = 0$ indicates the states are orthogonal and $F = 1$ indicates the states are identical. Fidelity is symmetric: $F(\rho_1,\ \rho_2) = F(\rho_2,\ \rho_1)$ Fidelity is contractive: for any quantum operation $\mathcal{E}$, $F(\mathcal{E}(\rho_1),\ \mathcal{E}(\rho_2)) \leq F(\rho_1,\ \rho_2)$. The quantum fidelity can be used to derive additional bounds on the error probability in state discrimination, such as

the Chernoff bound. It is possible to prove the two following inequalities for two arbitrary states ρ_0 and ρ_1:

$$P_{QB} \leq F_+ := \frac{1}{2}\sqrt{F}, \tag{2.64}$$

and

$$F_- := \frac{1-\sqrt{1-F}}{2} \leq P_{\text{err}}^{\min}, \tag{2.65}$$

so that, we have a chain of inequalities

$$F_- \leq P_{\text{err}}^{\min} \leq P_{QC} \leq P_{QB} \leq F_+. \tag{2.66}$$

2.3.5 Formulas for Gaussian states

The generalized overlap between two equiprobable Gaussian states, $\hat{\rho}_0$ and $\hat{\rho}_1$, can be computed using a closed formula.

$$P_{\text{QCB}} = \frac{1}{2}\left(\inf_{s\in[0,1]} C_s\right), \quad C_s := \text{Tr}\left(\hat{\rho}_0^s\,\hat{\rho}_1^{1-s}\right), \tag{2.67}$$

which is involved in the definitions of the QC bound and QB bound.

Consider the general case of two n-mode Gaussian states $\hat{\rho}_0\left(\bar{X}_0, \mathbf{V}_0\right)$ and $\hat{\rho}_1\left(\bar{X}_1, \mathbf{V}_1\right)$ where their CMs can be decomposed via a sympletic decomposition

$$\begin{aligned}
\mathbf{V}_0 &= \mathbf{S}_0\left(\bigoplus_{k=1}^{n} \nu^{k_0}\mathbf{I}\right)\mathbf{S}_0^{\mathbf{T}}, \\
\mathbf{V}_1 &= \mathbf{S}_1\left(\bigoplus_{k=1}^{n} \nu^{k_1}\mathbf{I}\right)\mathbf{S}_1^{\mathbf{T}},
\end{aligned} \tag{2.68}$$

where $\{\nu_k^0\}$ is the symplectic spectrum of $\mathbf{V}_0$, $\{\nu_k^1\}$ is the symplectic spectrum of $\mathbf{V}_1$, and $\mathbf{S}_0$, $\mathbf{S}_1$ are symplectic matrices.

In order to compute the generalized overlap C_s between two equiprobable Gaussian

states, $\hat{\rho}_0$ and $\hat{\rho}_1$, we can express it in terms of the mean values $\bar{X}_0$ and $\bar{X}_1$ and the sympletic eigenvalues $\mathbf{V}_0$ and $\mathbf{V}_1$. To derive this formulation, we introduce the real functions called

$$\begin{aligned} G_s(x) &= \frac{2^s}{(x+1)^s - (x-1)^s}, \\ \Lambda_s(x) &= \frac{(x+1)^s + (x-1)^s}{(x+1)^s - (x-1)^s}. \end{aligned} \tag{2.69}$$

which are positive for any $x \geq 1$. Then, we also define the "symplectic action" of Λ_s over an arbitrary CM

$$\mathbf{V} = \mathbf{S}\left(\bigoplus_{k=1}^{n} \nu_k \mathbf{I}\right)\mathbf{S}^{\mathbf{T}}, \tag{2.70}$$

as

$$\Lambda_s(\mathbf{V})_* = \mathbf{S}\left[\bigoplus_{k=1}^{n} \Lambda_s(\nu_k)\mathbf{I}\right]\mathbf{S}^{\mathbf{T}} \tag{2.71}$$

Given these preliminaries, we can now write the formula. For any $s \in [0, 1]$, the generalized overlap has the Gaussian expression

$$C_s = \frac{\Pi_s}{\sqrt{\det \Sigma_s}} \exp\left[-\frac{\mathbf{d}^{\mathbf{T}}\Sigma_s^{-1}\mathbf{d}}{2}\right], \tag{2.72}$$

where

$$\mathbf{d} := \bar{X}_0 - \bar{X}_1, \tag{2.73}$$

and

$$\Sigma_s := \Lambda_s(\mathbf{V}_0)_* + \Lambda_{1-s}(\mathbf{V}_1)_*, \tag{2.74}$$

and finally

$$\Pi_s := 2^n \Pi_{k=1}^{n} G_s\left(\nu_k^0\right) G_{1-s}\left(\nu_k^1\right). \tag{2.75}$$

A particular case of interest is the discrimination of zero-mean Gaussian states, where both states have a mean value of zero ($\bar{X}_0 = \bar{X}_1 = 0$). In this case, the previous formula

simplifies to the expression

$$C_s = \frac{\Pi_s}{\sqrt{\det \Sigma_s}}. \tag{2.76}$$

If we consider single-mode states ($n = 1$), the symplectic spectra consist of a single eigenvalue. In this case, we can write the symplectic decompositions as

$$\begin{aligned} \mathbf{V}_0 &= \mathbf{S}_0 \left(\nu^0 \mathbf{I}\right) \mathbf{S}_0^{\mathbf{T}} = \nu^0 \mathbf{S}_0 \mathbf{S}_0^{\mathbf{T}}, \\ \mathbf{V}_1 &= \mathbf{S}_1 \left(\nu^1 \mathbf{I}\right) \mathbf{S}_1^{\mathbf{T}} = \nu^1 \mathbf{S}_1 \mathbf{S}_1^{\mathbf{T}}. \end{aligned} \tag{2.77}$$

Then, we have

$$\begin{aligned} \Sigma_s &= \Lambda_s \left(\nu^0 \mathbf{I}\right) \mathbf{S}_0 \mathbf{S}_0^{\mathbf{T}} + \Lambda_{1-s} \left(\nu^1 \mathbf{I}\right) \mathbf{S}_1 \mathbf{S}_1^{\mathbf{T}}, \\ \Pi_s &= 2^s G_s \left(\nu^0\right) G_{1-s} \left(\nu^1\right), \end{aligned} \tag{2.78}$$

and

$$F\left(\hat{\rho}_0, \hat{\rho}_1\right) = \frac{2}{\sqrt{\Delta + \delta} - \sqrt{\delta}} \exp\left[-\frac{1}{2} \mathbf{d}^{\mathbf{T}} \left(\mathbf{V}_0 + \mathbf{V}_1\right)^{-1} \mathbf{d}\right], \tag{2.79}$$

where

$$\Delta := \det\left(\mathbf{V}_0 + \mathbf{V}_1\right), \quad \delta := \det\left(\mathbf{V}_0 - 1\right) \det\left(\mathbf{V}_1 - 1\right). \tag{2.80}$$

2.4 Measurement Detectors

The class of non-deterministic maps includes well-known detection methods in quantum optics such as homodyne and heterodyne detection. In Fig. 2.5 the two types of detection techniques make use of a balanced beam splitter. Consider a $50:50$ beam splitter with the reflection R and transmission T coefficients equal to $1/\sqrt{2}$. The two input modes are

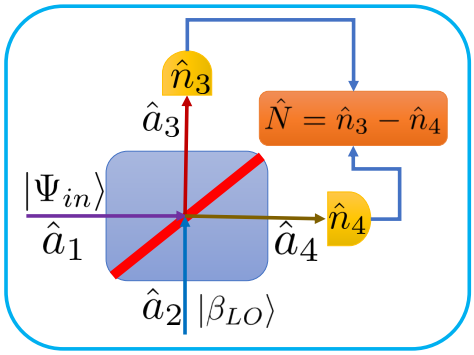

Figure 2.5: Schematic setup at the basics of balanced homodyne and heterodyne detection

$\hat{a}_1$ and $\hat{a}_2$. The two output modes $\hat{a}_3$ and $\hat{a}_4$ given by

$$\hat{a}_3 = \frac{\hat{a}_1 + \hat{a}_2}{\sqrt{2}}, \quad \hat{a}_4 = \frac{\hat{a}_2 - \hat{a}_1}{\sqrt{2}}. \tag{2.81}$$

The signal is determined by the disparity in photon number counts and is calculated as the difference $\hat{N}$ in signals recorded by photodetectors $\hat{n}_3 = \hat{a}_3^\dagger \hat{a}_3$ and $\hat{n}_4 = \hat{a}_4^\dagger \hat{a}_4$.

$$\hat{N} = \hat{n}_3 - \hat{n}_4 = \hat{a}_1^\dagger \hat{a}_2 + \hat{a}_2^\dagger \hat{a}_1. \tag{2.82}$$

Mode 2 is the "local oscillator", that is, it corresponds to an intense and stabilized coherent source (laser or mode), well described by a coherent state $|\beta_{LO}\rangle$, with $\beta_{LO} = |\beta_{LO}|\ e^{i\theta}\ e^{-i\omega_{LO}t}$ where ω_{LO} is the frequency of the local oscillator. Since $|\beta_{LO}| \gg 1$ we can neglect its quantum fluctuations and treat $\hat{a}_2$ as a complex function of time, $\hat{a} \to |\beta_{LO}| e^{i\theta - i\omega_{LO}t}$, where ω_{LO} is the frequency of the local oscillator field.

As a consequence, the output of the detection of Fig. 2.5. is a photocurrent proportional to the operator.

$$\hat{a}_1^\dagger e^{i\theta - i\omega_{LO}t} + \hat{a}_1 e^{-i\theta + i\omega_{LO}t}. \tag{2.83}$$

The operator $\hat{a}_1$ is the annihilation operator of a photon of a field rapidly oscillating at frequency close to the "carrier" frequency ω_1, so that it is convenient to rewrite it in term

of a slowly varying operator $\hat{\tilde{\boldsymbol{a}}}$, that is, $\hat{a} \rightarrow \tilde{\hat{\boldsymbol{a}}}_1 \mathrm{e}^{-i\omega_1 t}$, so that Eq. (2.83) becomes

$$\hat{I}_{\Delta,\,\theta}\,(t) = \tilde{\hat{\boldsymbol{a}}}_1\,\mathrm{e}^{-i\theta}\,\mathrm{e}^{i\Delta t} + \tilde{\hat{\boldsymbol{a}}}_1^{\dagger}\mathrm{e}^{i\theta}\,\mathrm{e}^{-i\Delta t}, \tag{2.84}$$

where $\Delta = \omega_{LO} - \omega_1$.

The photocurrent operator $\hat{I}_{\Delta,\,\theta}\,(t)$ is then filtered, that is, it is modulated by an oscillating current at frequency ω_{mod}, and integrated over a time τ,

$$\begin{aligned}\hat{J}^{\tau}_{\Delta,\,\theta}\,(\omega_{mod},\ t) &= \frac{1}{\tau}\int_{t-\tau}^{t} ds\ \cos\left(\omega_{mod}\ s\right)\hat{I}_{\Delta,\,\theta}\,(s)\\ &= \mathrm{e}^{-i\theta}\bar{\boldsymbol{a}}_{\tau}(\Delta+\omega_{mod},\ t) + \mathrm{e}^{i\theta}\bar{\boldsymbol{a}}^{\dagger}_{\tau}(-\Delta-\omega_{mod},\ t),\\ &+ \mathrm{e}^{-i\theta}\bar{\boldsymbol{a}}_{\tau}(\Delta-\omega_{mod},\ t) + \mathrm{e}^{i\theta}\bar{\boldsymbol{a}}^{\dagger}_{\tau}(-\Delta+\omega_{mod},\ t)\end{aligned} \tag{2.85}$$

where we have defined the filtered field operator

$$\bar{a}_{\tau}(\omega,\ t) = \frac{1}{2\tau}\int_{t-\tau}^{t} ds\ \hat{a}_1(s)\ \mathrm{e}^{i\omega s}. \tag{2.86}$$

We first consider homodyne detection, i.e, when $\omega_1 = \omega_{LO} \Longleftrightarrow \Delta = 0$. In this case the integrated photocurrenct is

$$\begin{aligned}\hat{J}^{\tau}_{\Delta,\,\theta}\,(\omega_{mod},\ t) &= \mathrm{e}^{-i\theta}\bar{\boldsymbol{a}}_{\tau}(\omega_{mod},\ t) + \mathrm{e}^{i\theta}\bar{\boldsymbol{a}}^{\dagger}_{\tau}(-\omega_{mod},\ t)\\ &+ \mathrm{e}^{-i\theta}\bar{\boldsymbol{a}}_{\tau}(-\omega_{mod},\ t) + \mathrm{e}^{i\theta}\bar{\boldsymbol{a}}^{\dagger}_{\tau}(\omega_{mod},\ t)\\ &= \hat{X}_{\theta,\tau}\,(\omega_{mod},\ t) + \hat{X}_{\theta,\tau}\,(-\omega_{mod},\ t),\end{aligned} \tag{2.87}$$

that is, the two quadratures at the two spectral components $\pm\omega_{mod}$ around the reference frequency ω_{LO}.

Therefore, when $\Delta = 0$, the detection system performs a measurement of a field quadrature; in the limit $\tau \rightarrow \infty$ and in the case of perfect detection, one gets a real number X_θ, and this corresponds to a projection onto the corresponding quadrature eigenstate $|X_\theta\rangle$.

We then consider heterodyne detection, i.e, when $\Delta \neq 0$ and $|\Delta| \gg \Omega_{sig}$= typical frequency of the field signal. In this case we take $\omega_{mod} = \Delta - \Omega_{sig}$

$$\begin{aligned}\hat{J}^{\tau}_{\Delta,\,\theta}\,(\Delta - \Omega_{sig},\ t) &= \mathrm{e}^{-i\theta}\bar{\boldsymbol{a}}_{\tau}(2\Delta - \Omega_{s},\ t) + \mathrm{e}^{i\theta}\bar{\boldsymbol{a}}^{\dagger}_{\tau}(-2\Delta + \Omega_{s},\ t) \\ &\quad + \mathrm{e}^{-i\theta}\bar{\boldsymbol{a}}_{\tau}(\Omega_{sig},\ t) + \mathrm{e}^{i\theta}\bar{\boldsymbol{a}}^{\dagger}_{\tau}(-\Omega_{sig},\ t) \\ &\approx \hat{X}_{\theta,\tau}\,(\omega_{sig},\ t),\end{aligned} \tag{2.88}$$

the first two terms are negligible because they oscillate at a frequency where there is no signal, but only added vacuum noise. So in this case only the quadrature of a given frequency Ω_{sig} is measured, differently from the homodyne case. Moreover the second term, $\mathrm{e}^{i\theta}\bar{a}^{\dagger}_{\tau}\,(-\Omega_{sig},\ t)$ is more relevant than the first one, and this is why we can think of heterodyne as measurement of the first operator, $\mathrm{e}^{-i\theta}\bar{a}^{\dagger}_{\tau}\,(\Omega_{sig},\ t)$ and a given measurement provides in the ideal case, a projection onto the corresponding coherent state $|\alpha\rangle\langle\alpha|$.

2.4.1 General-dyne measurement

Coherent states, which are called the "most classical" quantum states in the quantum optical domain, belong to a particular class of Gaussian states [118]. These states are the eigenvectors of the annihilation operators $\hat{a}$ and their covariance matrix is given by the 2×2 identity matrix. In Eq. (2.27), in a system with n modes, the coherent states represent a resolution of the identity operator.

$$\frac{1}{(2\pi)^{n}} \int_{\mathbf{R}^{2n}} d^{2n}X \hat{D}_{-X}\,|0\rangle\langle 0|\,\hat{D}_{X} = \mathbf{I}. \tag{2.89}$$

This equation implies that the collection of projections on coherent states $\hat{D}_{-X}\,|0\rangle\langle 0|\,\hat{D}_{X}$ is related to a positive operator-valued measure (POVM). In practice, this corresponds to a physical measurement setup; one well-known example of such a measurement is the heterodyne detection scheme, described in the previous paragraph. We now consider a

unitary transformation S which is a purely quadratic operation that corresponds to the symplectic transformation S,

$$\frac{1}{(2\pi)^n}\int_{\mathbf{R}^{2n}} d^{2n}X\hat{S}\,\hat{D}_{-X}\,|0\rangle\langle 0|\,\hat{D}_X\hat{S}^\dagger = \frac{1}{(2\pi)^n}\int_{\mathbf{R}^{2n}} d^{2n}X\hat{D}_{-\bar{X}}\hat{S}\;|0\rangle\langle 0|\,\hat{S}^\dagger\hat{D}_{\bar{X}} = \mathbf{I}, \tag{2.90}$$

where $\hat{S}\,\hat{D}_X\hat{S}^\dagger = \hat{D}_{\bar{X}}$ is still a displacement operator with displacement $\bar{X}$ which is the displacement transformed by the symplectic transformation S.

Upon observation of the measurement result, the measurement processes outlined in these identity resolutions map onto projections onto a fully generic pure Gaussian state $\hat{D}_X\hat{S}|0\rangle$ generalizing the previous examples of heterodyne and homodyne detection,

$$|\Psi_G\rangle = \hat{D}_{\bar{X}}\hat{S}^\dagger|0\rangle. \tag{2.91}$$

They are called "general-dyne" measurement, which, can also approximate the homodyne detection scheme which is a projection onto eigenstates of quadrature operators when the symplectic transformation S becomes a squeezing operator with an infinite squeezing parameter $S = diag(z, 1/z)$ for $z \to \infty$. The uncertainty associated with one of the quadrature operators approaches zero, while the uncertainty associated with its conjugate counterpart approaches infinity. It is easy to understand that the state onto which the system is projected is an eigenstate of the quadrature operator in this case.

2.4.2 Conditional general-dyne measurement

A conditional general-dyne measurement [88, 124], which involve projections onto pure Gaussian states $|\Psi_G\rangle$, would imply that the measurement procedure is contingent on certain observed outcomes or predetermined conditions. For instance, in quantum communication protocols or quantum information processing, a conditional general-dyne measurement can entail modifying the measurement plan in response to past measurement

outcomes or the quantum system's state at a particular stage of the procedure. This "conditional" part suggests a customized measurement strategy that considers particular information gathered during the experiment.

Consider a bipartite system, A with n modes and B with m modes, with the system's initial Gaussian state divided into subsystems A and B, each with covariance matrix and mean

$$\mathbf{V} = \begin{pmatrix} \mathbf{V}_A & \mathbf{V}_{AB} \\ \mathbf{V}_{AB}^{\mathbf{T}} & \mathbf{V}_B \end{pmatrix}, \quad \bar{\boldsymbol{X}} = \begin{pmatrix} \bar{\boldsymbol{X}}_A \\ \bar{\boldsymbol{X}}_B \end{pmatrix}. \tag{2.92}$$

A projective measurement involving a collection of pure Gaussian states $|\Psi\rangle_G$ as shown in Eq. (2.91), each characterized by mean $\bar{\boldsymbol{X}}_m$ and covariance $\mathbf{V}_m$ measurements, can effectively represent a general-dyne measurement on subsystem B. It's important to note that the outcome of the measurement, denoted by $\boldsymbol{X}_m$, is just a label. In such a measurement, the other subsystem yields a Gaussian state conditioned on the measurement outcome, conforming to a Gaussian distribution. We now provide a concise derivation of the measurement outcomes distribution and the resultant Gaussian state.

Any quantum state $\hat{\rho}$ can be written in the basis of displacement operator as shown in Eq. (2.11) using the Fourier-Weyl relation as

$$\hat{\rho} = \frac{1}{(2\pi)^{n+m}} \int_{\mathbf{R}^{2(n+m)}} d^{2n}X \, \chi(X) \, \hat{D}(-X), \tag{2.93}$$

where the displacement operator $D(\xi) := \exp\left(i\hat{\mathbf{X}}^{\mathbf{T}}\Omega\xi\right)$ and satisfies orthogonal relation $\mathrm{Tr}\left[D(\xi)\, D(\xi')\right] = \pi^{n+m}\delta(\xi + \xi')$. For Gaussian states with covariance matrix $\boldsymbol{V}$ and mean $\bar{\boldsymbol{X}}$, the Wigner characteristic function has the Gaussian form

$$\chi(X) := \mathrm{Tr}\left[\hat{\rho}\, D(X)\right] = \exp\left[-\frac{1}{2} X^{\mathbf{T}} \left(\Omega \boldsymbol{V} \Omega^{\mathbf{T}}\right) X - i\left(\Omega\bar{\boldsymbol{X}}\right)^{\mathbf{T}} X\right]. \tag{2.94}$$

We now perform the general-dyne measurement which projects subsystem B onto the Gausssian state $|\Psi_G\rangle_B$. As a consequence, the state of subsystem A conditioned to the measurement result $\bar{\boldsymbol{X}}_m$ becomes

$$\begin{aligned}\mathrm{Tr}_B\left[\hat{\rho}_G\,\hat{\rho}\right] = {}_B\langle\Psi_G|\,\hat{\rho}\,|\Psi_G\,\rangle_B = \frac{1}{(2\pi)^{n+m}}\int_{\mathbf{R}^{2(n+m)}} dX_B \exp\left(-\frac{1}{4}i\boldsymbol{X}^{\mathbf{T}}\boldsymbol{\Omega}^{\mathbf{T}}\mathbf{V}\boldsymbol{\Omega}\boldsymbol{X} + i\boldsymbol{X}^{\mathbf{T}}\boldsymbol{\Omega}^{\mathbf{T}}\boldsymbol{X}'\right)\\ {}_B\langle\Psi_G|\hat{D}\,(-X)\,|\Psi_G\rangle_B,\end{aligned} \tag{2.95}$$

where we have used $\mathrm{Tr}_B\left[\hat{\rho}_G\,\hat{D}_{-\boldsymbol{X}_B}\right] = {}_B\langle\Psi_G|\hat{D}\,(-X)\,|\Psi_G\rangle_B$. By explicitly calculating the multivariate Gaussian integral,

$$\begin{aligned}{}_B\langle\,\Psi_G\,|\hat{\rho}|\Psi_G\rangle_B = \frac{e^{\frac{1}{2}(\bar{\boldsymbol{X}}_m-\bar{\boldsymbol{X}}_B)^{\mathbf{T}}\frac{1}{(\boldsymbol{V}_B+\boldsymbol{V}_m)}(\bar{\boldsymbol{X}}_m-\bar{\boldsymbol{X}}_B)}}{(2\pi)^n\sqrt{(\boldsymbol{V}_B+\boldsymbol{V}_m)}}\\ \int dX_A e^{\boldsymbol{X}_A^{\mathbf{T}}\left(\boldsymbol{V}_A-\boldsymbol{V}_{AB}\frac{1}{(\boldsymbol{V}_B+\boldsymbol{V}_m)}\boldsymbol{V}_{AB}^{\mathbf{T}}\right)\boldsymbol{X}_A}e^{-\boldsymbol{X}_A^{\mathbf{T}}\left(\boldsymbol{X}_A-\boldsymbol{V}_{AB}\frac{1}{(\boldsymbol{V}_B+\boldsymbol{V}_m)}(\bar{\boldsymbol{X}}_m-\bar{\boldsymbol{X}}_B)\right)}\hat{D}\left(\boldsymbol{\Omega}^{\mathbf{T}}\boldsymbol{X}_A\right).\end{aligned} \tag{2.96}$$

We get the final characteristics function subsystem A, yielding the mean and covariance matrix of the subsystem A, as well as the probability distribution of measurement outcomes.

$$\begin{aligned}V_A' &= V_A - V_{AB}\frac{1}{(V_B+V_m)}V_{AB}^{\mathbf{T}},\\ \bar{X}_A^{'} &= \bar{X}_A^{'} + V_{AB}\frac{1}{(V_B+V_m)}\left(\bar{X}_m-\bar{X}_B\right),\\ p\left(\bar{X}_m\right) &= \frac{e^{\frac{1}{2}\left(\bar{X}_m-\bar{X}_B\right)^{\mathbf{T}}\frac{1}{(V_B+V_m)}\left(\bar{X}_m-\bar{X}_B\right)}}{(2\pi)^m\sqrt{\det\left(V_B+V_m\right)}}.\end{aligned} \tag{2.97}$$

Notice that the measurement outcome affects only the mean values of the state, while the covariance matrix does not depend upon it and it is the same for any measurement outcome.

Chapter 3

Microwave quantum illumination with correlation-to-displacement conversion

This chapter incorporates material from the following publications: ([1] Microwave quantum illumination with correlation-to-displacement conversion, Jacopo Angeletti, Haowei Shi, **Theerthagiri Lakshmanan**, David Vitali, Quntao Zhuang, Phys. Rev. Applied 20, 024030 – Published 11 August 2023.)

3.1 Introduction

Quantum illumination (QI) is an entanglement-assisted sensing scheme that enhances the precision and sensitivity of target detection [83, 120, 134], via entangling the signal probes with locally stored idlers. Originally developed to simply detect the presence or absence of a target, QI offers a 6-decibel improvement in error exponent due to entanglement [134]. In recent years, QI has been extended to improve target range and angle detection [152, 153], demonstrating an even greater advantage over classical counterparts in the intermediate signal-to-noise-ratio (SNR) region, thanks to the threshold phenomena of nonlinear parameter estimation [153].

Despite these theoretical advancements in QI, its experimental realization in the microwave domain, which is the natural scenario for its application, has faced several limitations. One of the practical challenges is the need for extensive cooling for microwave quantum-limited detection, due to the high natural noise background, and the lack of developed photon-counting detection technology [6, 31]. To address these issues, a solution for QI based on optical-microwave transduction has been proposed [9]. This approach utilizes an optical idler mode for noiseless storage at room temperature, and up-converts the microwave return mode to the optical domain for quantum-limited joint detection of optical photons. However, the current state-of-the-art efficiency in optical-microwave transduction [8, 16, 39, 56, 80, 112] falls short of what is required to sustain this transduction-based scheme in the near future.

In addition to the practical challenges, a fundamental limitation of QI is the receiver design problem. Currently, practical receivers such as the optical parametric amplifier receiver (OPAR) and the phase-conjugate receiver (PCR) can only attain half of the error exponent advantage [54]. The optimal receiver would require unit-efficiency sum-frequency-generation at the single photon level [154], which is highly challenging to realize experimentally. The problem of optimal receiver design seems to necessitate nonlinear processes and joint operations on the idler and return modes, making it difficult to implement in practice.

Previous in-principle demonstrations of QI target detection have been hindered by the aforementioned limitations. One example is an optical domain simulation, which injected noise to mimic a microwave scenario and utilized a sub-optimal OPAR [151]. This approach achieved approximately 20% of the error exponent advantage. Another demonstration in the microwave domain used a digitally reconstructed PCR [10], but was unable to surpass the performance of the classical benchmark represented by an ideal coherent state source with the same mean number of photons and homodyne detection. More recently, the OPAR scheme was adapted to the microwave domain, overcoming

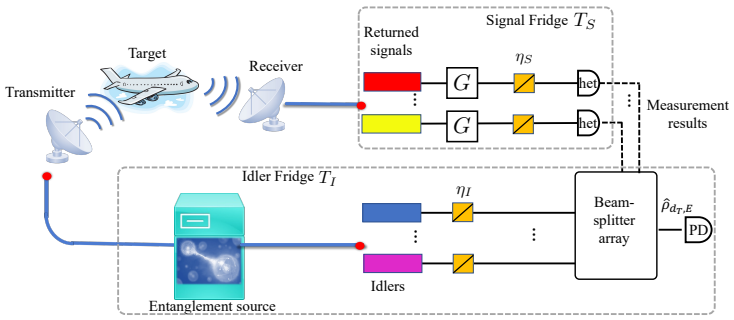

Figure 3.1: Schematic of the quantum illumination, with a practical receiver based on correlation-to-displacement conversion, in presence of noise and loss. 'het': heterodyne detection. 'PD': photo-detection.

several challenges in microwave photon processing [6] and again yielding roughly 20% of the error exponent advantage.

A recent development in the field of optimal receiver design is the correlation-to-displacement ('C↛D') conversion proposal, which suggests that the optimal receiver design can be achieved by heterodyne-detecting the return mode separately and processing the associated conditional idler field [123]. Upon heterodyne detection of the return modes, the idler modes collapse to coherent states embedded in weak thermal noise. With the help of well-established coherent state discrimination protocols, the C↛D receiver design can attain the optimal error probability of QI [96]. This receiver design requires only programmable linear optics [75, 87] and photon detection, making it more feasible for experimental realization. Additionally, it eliminates the need for mode-matching between the noisy return fields at room temperature and the cooled idler fields, avoiding technical difficulties.

In this study, we evaluate the feasibility of the C↛D receiver design in the microwave domain. We account the lossy antenna coupling to the detection in real radar systems, by introducing loss $1 - \eta_S \leq 1$ in the return mode prior to heterodyne detection. To mitigate this loss, we suggest using parametric amplification with gain $G \geq 1$. Our results show that the full optimal six-decibel error-exponent advantage can be retained when

$G\eta_S \gg 1$ if the amplifier is quantum limited. Even if the amplifier introduces noise at room temperature, the C↛D receiver still provides a three-decibel advantage over the ideal classical system. Furthermore, we consider the case of limited detection capability in the idler modes. Instead of the complex Dolinar receiver, we consider the simpler Kennedy receiver and still observe the optimal error exponent advantage. Finally, we compare the practical C↛D receiver design with both the classical coherent-state homodyne detection and the PCR (which is more effective than the OPAR [125]).

In this chapter is organized as follows. Sec. 3.2 describes the protocol, while Sec. 3.3 recalls the basic properties and tools of QI. Sec. 3.4 provides a brief review of the C↛D receiver and its performance under ideal conditions. Sec. 3.5 discusses relevant experimental limitations in the case of microwave QI, and Sec. 3.6 shows the performance of the C↛D module in the presence of such realistic scenarios. Sec. 3.7 compares the performance of the C↛D module with that of classical QI based on coherent state and homodyne detection and that of the PCR. In Sec. 3.8, we consider performance enhancement if we further allow number-resolving detection. Finally, Sec. 3.8.2 presents the Neyman-Pearson framework and receiver operating characteristic (ROC) curves.

3.2 Overall protocol

As shown in Fig. 3.1, in a target detection scenario, the transmitter sends signals to the target, and then the receiver collects return signals and performs measurement to infer about target's presence or absence. To benefit from entanglement, a source generates pairs of idler-signal entangled pulses. The idlers are stored locally and used to assist joint measurements with the return signals. In QI, such signal-idler entanglement provides a six-decibel error exponent advantage, despite being destroyed by extremely lossy transmission and high noise background.

Our proposed receiver system adapts the C↛D conversion approach to practical re-

ceiver operating conditions. While the idlers are cooled to $T_I \sim 10$ mK to enable quantum advantage, the returned signal part is cooled to a much higher temperature T_S for experimental convenience. Such a layout is possible as the C↛D conversion module only feeds the classical heterodyne measurement results on the 'warm' and noisy returned signals, to perform conditional linear optical transforms on the 'cool' idler alone (indicated by the dashed line), avoiding idler contamination. Finally, photo-detection is performed on the transformed idler, and a decision on the target's presence or absence is made according to the measurement result. To compensate for additional loss $1 - \eta_S$ at the receiver antenna, amplification of gain G is performed. However, the loss $1 - \eta_I$ on the idler needs to be minimized and cannot be compensated. The photo-detection can be realized via coupling the microwave idler modes to transmon qubits, as demonstrated in Refs. [6, 31].

3.3 Quantum illumination for target detection

QI is a quantum-based remote sensing technique that leverages the entanglement between signal (a_S) and idler (a_I) modes. The signal mode probes a target region, while the idler one is kept at the emission station.

$$|\Psi\rangle_{SI} = \sum_{n=0}^{\infty} \sqrt{\frac{N^n}{(N+1)^{n+1}}}\, |n\rangle_S\, |n\rangle_I. \tag{3.1}$$

By performing a joint measurement on the signal and idler modes, the quantum correlations of the transmitted state are exploited at the receiving station. The problem is framed as a binary decision-making task, where the two hypotheses are: 'target absent' (H_0) and 'target present' (H_1). The asymptotic optimal input state is a two-mode squeezed vacuum (TMSV) state, a bipartite Gaussian state characterized by its covariance matrix

(CM) [96, 100]

$$\mathbf{V}_{SI} = \begin{pmatrix} (2N_S + 1)\,\mathbf{I} & 2\sqrt{N_S\,(N_S + 1)}\mathbf{Z} \\ 2\sqrt{N_S\,(N_S + 1)}\mathbf{Z} & 2\,(N_S + 1)\,\mathbf{I} \end{pmatrix}, \tag{3.2}$$

where $\mathbf{Z} = \mathrm{diag}\{1, -1\}$, $\mathbf{I} = \mathrm{diag}\{1, 1\}$, and $\left\langle a_S^\dagger a_S \right\rangle = N_S$ is the signal brightness. While the idler is stored for later detection, the signal is transmitted through a phase-shift thermal-loss channel $\Phi_{\kappa,\theta}$, whose action on its mode when the target is present is described by

$$a_R = \mathrm{e}^{\mathrm{i}\theta}\sqrt{\kappa}a_S + \sqrt{1-\kappa}a_B, \tag{3.3}$$

while the absence of a target corresponds to the case $\kappa = 0$, i.e., where the channel is $\Phi_{0,0}$. Upon the channel $\Phi_{\kappa,\theta}$, the CM Eq. (3.2) becomes

$$\mathbf{V}_{RI} = \begin{pmatrix} [2\,(\kappa N_S + N_B) + 1]\,\mathbf{I} & 2\sqrt{\kappa N_S\,(N_S + 1)}\mathbf{RZ} \\ 2\sqrt{\kappa N_S\,(N_S + 1)}\mathbf{Z}\mathbf{R}^T & (2N_S + 1)\,\mathbf{I} \end{pmatrix}, \tag{3.4}$$

where $\mathbf{RZ} = \Re\left[\mathrm{e}^{\mathrm{i}\theta}\,(\mathbf{Z} + \mathrm{i}\mathbf{X})\right]$ (with $\Re$ indicating the real part and $\mathbf{X}$ the Pauli-X matrix), such that $\mathbf{R}$ denotes a phase rotation of $-\theta$,

and $\left\langle a_B^\dagger a_B \right\rangle = N_B/\,(1-k)$ is the mean number of thermal background photons. Tab. 3.1 shows the mean thermal photon number for a typical microwave field at $\omega = 2\pi \times 5$ GHz at temperatures of interest. The signal and return modes propagate at room temperature, while—depending upon the chosen device—detectors and amplifiers can be operated at temperature T_S equaling either the room temperature, a few Kelvins, or ideally close to the Josephson parametric amplifier generating the TMSV state at microwave frequency [3,43], which is typically placed in the cold plate of a dilution refrigerator at about

$\omega/2\pi$ [GHz]	T [K]	$N \sim$
5	3×10^2	1.25×10^3
	10^2	4.15×10^2
	10	40
	4	15
	1	4
	10^{-1}	10^{-1}
	10^{-2}	4×10^{-11}
	4×10^{-3}	9×10^{-27}

Table 3.1: Values of mean thermal photon numbers for a microwave mode at $\omega = 2\pi \times 5$ GHz at temperature values of interest.

10 mK [6, 10, 21]. The idler is always stored in the dilution refrigerator at about $T_I \sim 10$ mK [6, 10, 21], to enable quantum advantages.

3.4 Correlation-to-displacement conversion in the ideal case

Ref. [123] proposes a conversion module for capturing and transforming quantum correlation into coherent quadrature displacement, to enable the optimal receiver design for various entanglement-enhanced protocols. The module is based on heterodyne and programmable passive linear optics, see Fig. 3.2, where the explicit implementation of the array is shown, and maps the multi-mode quantum detection problem to the semi-classical detection problem of a single-mode noisy coherent state, allowing for explicit measurements to achieve the optimal performance. The input modes of the array are the idler modes conditioned to the result of the corresponding heterodyne meausurement. Each idler pulse is stored in a quantum memory and properly delayed so that they are sent pro-

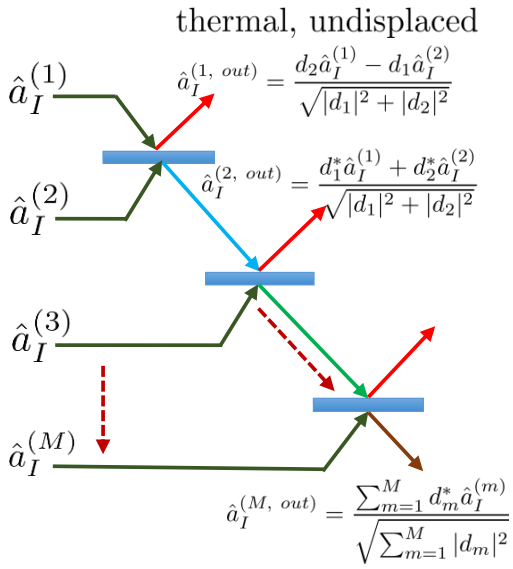

Figure 3.2: Beamsplitter array with proper weights with each $\hat{a}_{I,m}$

gressively to each beam splitter of the array (see Fig. 3.2). The result of the heterodyne measurement determines the trasmissivity of each beam splitter in order to accumulate the coherent amplitute of the conditioned idler modes onto a single collective idler mode. The other $M - 1$ output modes of the array are instead in an effective thermal state of no interest. The module provides a paradigm for processing noisy quantum correlations for near-term implementation and can be applied to a wide range of entanglement-enhanced protocols, including quantum illumination, phase estimation, classical communication, target ranging, and thermal-loss channel pattern classification.

3.4.1 Heterodyne measurement

Now, we possess a module specifically created to convert the phase-sensitive cross-correlation among M signal-idler pairs into the complex displacement amplitude of a single-mode coherent state. This module effectively transforms the semi-classical challenge of coherent state processing into the quantum realm of receiver design.

Chapter 2 provides a detailed explanation of the return-idler mode pairs $\{\hat{a}_{R_m}, \hat{a}_{I_m}\}$ in Fig. 3.1, each $\hat{a}_{R_m}$ undergoes an individual heterodyne measurement, producing the complex measurement result M_m. In this case, we can assume that the covariance matrix $V_m = (N_B + \kappa N_S + 1)/2$, the first moments $\bar{X}_m = (q_m, p_m)$ are specified as a two-dimensional vector consisting of the position q_m and momentum p_m, and the first moments of subsystem return mode (R) and Idler (I) mode are both equal to zero, i.e., $\bar{X}_R = \bar{X}_I = 0$.

In this scenario, the conditional evolution of second moments does not depend on the measurement outcome, and we can use this fact to determine various properties of the $TMSV$ system, such as its entanglement and squeezing properties. This property of Gaussian states is useful in practical applications of quantum information processing, such as quantum communication, quantum illumination, and quantum cryptography.

$$\begin{aligned} V_R &= (2\kappa N_S + 2N_B + 1)\,\mathbf{I}_{2\times 2}, \\ V_I &= (2N_S + 1)\,\mathbf{I}_{2\times 2}, \\ V_{RI} &= \left(2\sqrt{N_S(N_S+1)}\right)\mathbf{I}_{2\times 2}\mathbf{RZ}, \mathbb{RZ} \end{aligned} \tag{3.5}$$

where $\mathbf{RZ} = \Re\left[e^{i\theta}(\mathbf{Z} - i\mathbf{X})\right]$ (with $\Re$ indicating the real part and $\mathbf{X}$ the Pauli-X matrix), such that $\mathbf{R}$ denotes a phase rotation of $-\theta$,

$$\mathbf{RZ} = \begin{pmatrix} cos\theta & sin\theta \\ sin\theta & -cos\theta p_{\Pi} \end{pmatrix}. \tag{3.6}$$

By applying the general-dyne formulas of the previous chapter 2 in the special case of heterodyne meausrement and therefore a projection onto a coherent state on subsystem I of the $TMSV$ system R and I, we can obtain the mean and covariance matrix for the conditional Gaussian measurement outcomes. The mean value is given by $\bar{X}_m = \mathbf{Tr}\left[\hat{\rho}_m \hat{X}_I\right]$, where $\hat{X}_I$ is the vector of quadrature operators for subsystem I. The covariance matrix

is given by $\boldsymbol{V}_m = \mathbf{Tr}\left[\hat{\rho}_m \left(\hat{X}_I - \bar{X}_m\right)\left(\hat{X}_I - \bar{X}_m\right)^T\right]$. Note that these values depend on the specific choice of the general-dyne detection $\boldsymbol{V}_m$ and first moments $\bar{\boldsymbol{X}}_m$.

$$
\begin{aligned}
V_I' &= \left(2\frac{(1-\kappa+N_B)\,N_S}{\kappa N_S + N_B + 1} + 1\right)\mathbf{I}_{2\times 2}, \\
\overline{X}_I &= \frac{\sqrt{\kappa N_S(N_S+1)}}{\kappa N_S + N_B + 1}\begin{pmatrix} cos\theta q_\Pi + sin\theta p_\Pi \\ \\ sin\theta q_\Pi - cos\theta p_\Pi \end{pmatrix}, \\
p\left(\overline{X}_m\right) &= \frac{\exp\left(\dfrac{-|\overline{X}_m|^2}{4\,(\kappa N_S + N_B + 1)}\right)}{4\,(\kappa N_S + N_B + 1)}.
\end{aligned}
\tag{3.7}
$$

These formulas imply that the state of the idler conditioned to the heterodyne measurement on the return mode is a displaced thermal state, with a mean value of $\bar{X}_I$ and a thermal photon number of $E = (1-\kappa+N_B)N_S/(\kappa N_S + N_B + 1)$. We can represent this state using the density operator $\hat{\rho}_{\bar{X}_I,E}$, which is a sum over all photon number states $n = 0, 1, 2, ...$ weighted by a displacement operator $\hat{D}(\bar{X}_I)$ and a thermal distribution. Specifically, we have

$$
\hat{\rho}_{\bar{X}_I,E} \equiv \sum_{n=0}^{\infty} \hat{D}(\bar{X}_I)\frac{E^n}{(1+E^n)^{n+1}}|n\rangle\langle n|\hat{D}^\dagger(\bar{X}_I), \tag{3.8}
$$

where $\bar{X}_I$ represents the displacement parameter, and E is the thermal photon number. The mean thermal photon number E can be expressed in terms of the system and bath parameters, where N_S and N_B are the average photon numbers of the system and the bath, respectively.

Each $\hat{a}_{I_m}$, given the output M_m, is in a displaced thermal state $\hat{\rho}_{d_m,E}$, with an average thermal photon number $E \leq N_S$ and a mean $d_m = (C_p/2V_m)\,\mathrm{e}^{i\theta}M_m^*$. As shown in Fig. 3.2, there are different approaches to measure the idler modes in this context in order to extract information. For a given state $\hat{\rho}_{d_T,E}$, a passive linear optical transformation (beamsplitter

array with weights appropriately chosen) can combine all outputs into a single mode with a mean $d_T = |d_T|e^{i\theta}$ and thermal noise E. The amplitude square has $2M$ degrees of freedom and is expressed as $|d_T|^2 = \sum_{m=1}^{M} |d_m|^2$. It follows a χ^2 distribution.

QI for target detection considers the discrimination between two channels, $\Phi_{(0,0)}$ and $\Phi_{(\kappa,0)}$. In the ideal case, the conversion module produces the displaced thermal states ρ_{0,N_S} (target absent, H_0) and $\rho_{\sqrt{x},E}$ (target present, H_1), where $x \sim P^{(M)}(\cdot;\xi_{\text{Ideal}})$ obeys a (generalized) χ^2 distribution with $\xi_{\text{Ideal}} \equiv \kappa N_S(N_S+1)/2(\kappa N_S + N_B + 1)$. Here the probability density function for the χ^2 distribution parameterized by ξ is given by

$$P^{(M)}(x;\xi) = \frac{x^{M-1}e^{-x/(2\xi)}}{(2\xi)^M \Gamma(M)}, \tag{3.9}$$

where $\Gamma(M) = (M-1)!$ is the gamma function. This leads to the error probability performance limit

$$P_{\text{C}\to\text{D}} = \int_0^{+\infty} dx\, P^{(M)}(x;\xi)\, P_{\text{H}}\left(\rho_{0,N_S}, \rho_{\sqrt{x},E}\right), \tag{3.10}$$

where P_{H} is the Helstrom limit [58–60]

$$P_{\text{H}}(\rho_1,\rho_2) = \frac{1}{2}\left(1 - \frac{1}{2}\text{Tr}\left[|\rho_1 - \rho_2|\right]\right), \tag{3.11}$$

in the case of equal prior probability. As shown in Ref. [123], even though the exact solution of Eq. (3.10) is challenging, we can obtain lower (LB) and upper bounds (UB) for the error exponent $r_{\text{C}\to\text{D}} = -\lim_{M\to\infty} \ln(P_{\text{C}\to\text{D}})/M$. The upper bound can be achieved by approximating $\rho_{\sqrt{x},E}$ as a coherent state and ρ_{0,N_S} as vacuum. In the respect of the asymptotic analysis, the Helstrom limit approaches $P_{\text{H}}\left(\rho_{0,N_S}, \rho_{\sqrt{x},E}\right) \sim e^{-x}/4$, which—combined with Eq. (3.10)—gives the upper bound $r_{\text{C}\to\text{D}}^{(\text{UB})} = 2\xi$. On the other hand, a lower bound of the conversion module performance can also be obtained as [123]

$$r_{\text{C}\to\text{D}}^{(\text{LB})} = 2\xi\left(\sqrt{N_S+1} - \sqrt{N_S}\right)^2. \tag{3.12}$$

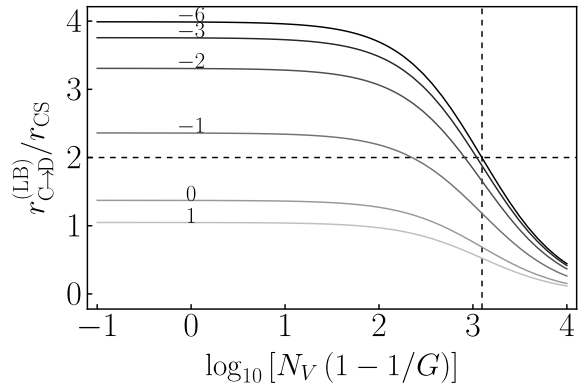

Figure 3.3: Behavior of $r^{(\mathrm{LB})}_{\mathrm{C}\to\mathrm{D}}/r_{\mathrm{CS}}$ as a function of $\log_{10}[N_V(1-1/G)]$ with amplification and ideal signal and idler detection, for different values of $\log_{10} N_S$, given $N_B = 1250$ and $\kappa = 0.01$. $N_S = \left\{10^1,\ 10^0,\ 10^{-1}, 10^{-2},\ 10^{-3},\ 10^{-6}\right\}$ from bottom to top, as indicated by the labels on top of the curves. The plot indicates that the amplification stage provides a factor of advantage greater than 2 (as indicated by the horizontal dashed line) for a range of relevant parameters. This is due to the robust compensation of noise effects achieved by amplifying, as demonstrated by the vertical dashed line at $N_V(1-1/G) = N_B$.

In comparison, the optimal classical case, achieved when a coherent-state with mean photon number N_S is sent to the target, has the error exponent

$$r_{\mathrm{CS}} = \kappa N_S \left(\sqrt{N_B+1} - \sqrt{N_B}\right)^2. \tag{3.13}$$

In the $N_S \ll 1$ and $N_B \gg 1$ limit, one finds that $r^{(\mathrm{UB})}_{\mathrm{C}\to\mathrm{D}} \simeq r^{(\mathrm{LB})}_{\mathrm{C}\to\mathrm{D}} \simeq 4r_{\mathrm{CS}}$, which achieves the optimal advantage.

3.5 Practical microwave detection scenario

Regardless of the technology or setup employed, non-idealities or imperfections will always exist in practical systems, affecting their performance. To mitigate this, we propose the use of a pre-detection amplifier, which can compensate for additional coupling loss. Our results demonstrate that this approach can effectively improve the performance of binary hypothesis testing and enhance the accuracy of state discrimination.

Before detection, the returned mode is amplified using a quantum amplifier, leading to the amplified mode

$$a_A = \sqrt{G}a_R + \sqrt{G-1}a_V^\dagger, \tag{3.14}$$

where $\left\langle a_V^\dagger a_V \right\rangle = N_V$ is the mean photon number of the amplifier noise mode. The amplified a_A and the idler a_I modes share the CM

$$\mathbf{V}_{AI} = \begin{pmatrix} (2N_A+1)\,\mathbf{I} & V_{12}\mathbf{RZ} \\ V_{12}\mathbf{ZR}^T & (2N_S+1)\,\mathbf{I} \end{pmatrix}, \tag{3.15}$$

where

$$\begin{aligned} N_A &= \left\langle a_A^\dagger a_A \right\rangle \\ &= G\left[\kappa N_S + N_B + (1-1/G)\,(N_V+1)\right], \\ V_{12} &= 2\sqrt{G\kappa N_S\,(N_S+1)}. \end{aligned} \tag{3.16}$$

Microwave amplifiers with gain $G \sim 100$ and excess noise of $N_V \sim 10$ photons have been successfully utilized in various microwave QI experiments [10]. Additionally, superconducting quantum computers employ microwave quantum-limited amplifiers that exhibit added noise levels of about half a photon [1]. The behavior of such experimental systems can be accurately described by the phase-insensitive linear amplifier model presented in Eq. (3.14).

It should be noted how, comparing Eq. (3.15) with the one without any amplification Eq. (3.4), the performance lower bound Eq. (3.12) applies also to the case with the amplifier, as long as one replaces the parameters $\kappa \to G\kappa$ and $N_B \to N_A - G\kappa N_S$. Furthermore, we see that if $(1-1/G)\,(N_V+1) \ll N_B$, the performance of the conversion module does not change asymptotically. This is verified in Fig. 3.3 via calculating $r_{\mathrm{C}\to\mathrm{D}}^{(\mathrm{LB})}/r_{\mathrm{CS}}$ vs $\log_{10}\left[N_V\,(1-1/G)\right]$, where the factor of four (6 dB) advantage is seen at the $N_S \ll 1$

limit.

The same analysis can also be applied to the non-ideal scenario of imperfect heterodyne detection of the amplified mode and imperfect idler detection. Heterodyne detection efficiency in the microwave regime typically ranges from 40% to 70% depending on the input power. However, in the scope of our analysis, η_S represents the overall channel efficiency, which is dependent on the specific experiment and may be much lower, with realistic values around 10% or even less (down to 1%).

For simplicity, we assume the non-ideal heterodyne detection to be symmetric in the quadratures, resulting in the input-output relation

$$a'_A = \sqrt{\eta_S}\, a_A + \sqrt{1-\eta_S}\, a_{E_1}, \tag{3.17}$$

where we set $\left\langle a^\dagger_{E_1} a_{E_1} \right\rangle = N_{E_1}$. By performing the analysis through channel composition [see Eqs. (3.3), (3.14), and (3.17)], one can obtain

$$\begin{aligned} a'_A &= \mathrm{e}^{\mathrm{i}\theta} \sqrt{\eta_S G \kappa}\, a_S + \sqrt{1-\eta_S G \kappa}\, \tilde{a}, \\ \tilde{a} &= \frac{\sqrt{\eta_S G\,(1-\kappa)}\, a_B + \sqrt{\eta_S\,(G-1)}\, a_V^\dagger + \sqrt{1-\eta_S}\, a_{E_1}}{\sqrt{1-\eta_S G \kappa}}, \end{aligned} \tag{3.18}$$

with $\left[\tilde{a}, \tilde{a}^\dagger\right] = 1$, and

$$\left\langle \tilde{a}^\dagger \tilde{a} \right\rangle = \frac{\eta_S G N_B + \eta_S\,(G-1)\,(N_V+1) + (1-\eta_S)\, N_{E_1}}{1-\eta_S G \kappa}. \tag{3.19}$$

With this composition, the channel is now characterised by the parameters

$$\begin{aligned} \kappa &\to \eta_S G \kappa, \\ N_B &\to \eta_S G \left[N_B + (1 - 1/G)\,(N_V+1) + \frac{1-\eta_S}{\eta_S G} N_{E_1} \right]. \end{aligned} \tag{3.20}$$

If we combine this reparameterization with an imperfect idler detection

$$a'_I = \sqrt{\eta_I} a_I + \sqrt{1-\eta_I} a_{E_2}, \tag{3.21}$$

with $\left\langle a^\dagger_{E_2} a_{E_2} \right\rangle = N_{E_2}$, the CM of these two non-ideal modes a'_A and a'_I can be expressed as

$$\mathbf{V}'_{AI} = \begin{pmatrix} \left(2N'_A + 1\right)\mathbf{I} & V'_{12}\mathbf{RZ} \\ V'_{12}\mathbf{ZR}^T & \left(2N'_I + 1\right)\mathbf{I} \end{pmatrix}, \tag{3.22}$$

where we call

$$\begin{aligned} N'_A &= \eta_S G \left[\kappa N_S + N_B + (1 - 1/G)(N_V + 1) + \frac{1-\eta_S}{\eta_S G} N_{E_1} \right], \\ V'_{12} &= 2\sqrt{\eta_S \eta_I G \kappa N_S (N_S + 1)}, \\ N'_I &= \eta_I \left(N_S + \frac{1-\eta_I}{\eta_I} N_{E_2} \right). \end{aligned} \tag{3.23}$$

It is worth noting how the dominance of N'_A by N_B in Eq. (3.23) suggests that excess noise from the electronics may not play a significant role.

3.6 Correlation-to-displacement conversion in practice

Since the procedure has been extensively discussed in Ref. [123], we will not delve into it in this paper. By heterodyning mode a'_A, one obtains

$$\begin{aligned} \mathbf{V}'^{(Het)}_{I|A} &= (2E' + 1)\mathbf{I}, \\ E' &= N'_I - \frac{\eta_S \eta_I G \kappa N_S (N_S + 1)}{N'_A + 1}. \end{aligned} \tag{3.24}$$

Correspondingly, with measurement result $\overline{\mathbf{x}}_\Pi = (q_\Pi, p_\Pi)^T$, the mean of the non-ideal idler becomes

$$\overline{\mathbf{x}}_I' = \frac{\sqrt{\eta_S \eta_I G \kappa N_S \left(N_S + 1\right)}}{N_A' + 1} \begin{pmatrix} q_\Pi \cos\theta + p_\Pi \sin\theta \\ \\ q_\Pi \sin\theta - p_\Pi \cos\theta \end{pmatrix}. \tag{3.25}$$

With the imperfections in consideration, the distribution of the measurement outcomes is given by

$$p\left(\overline{\mathbf{x}}_\Pi\right) = \frac{\exp\left(-\frac{\left|\overline{\mathbf{x}}_\Pi\right|^2}{4\left(N_A'+1\right)}\right)}{4\pi\left(N_A' + 1\right)}, \tag{3.26}$$

from which the distribution of $\mathcal{M}_m = \left(q_{\Pi_m} + \mathrm{i} p_{\Pi_m}\right)/2$

$$p\left(\mathcal{M}_m\right) = \frac{\exp\left(-\frac{|\mathcal{M}_m|^2}{N_A'+1}\right)}{\pi\left(N_A' + 1\right)}. \tag{3.27}$$

Finally, by utlizing the displacement conditional on the heterodyne measurement result in the idler complex plane

$$d_m = \frac{\sqrt{\eta_S \eta_I G \kappa N_S \left(N_S + 1\right)} \mathrm{e}^{\mathrm{i}\theta} \mathcal{M}_m^\star}{N_A' + 1}, \tag{3.28}$$

we can express the total displacement of the collective idler mode at the output of the programmable beam splitter array, through a change of variables, as

$$\begin{aligned} |d_T|^2 &= \sum_{m=1}^{M} |d_m|^2 = \xi \sum_{m=1}^{M} z_i^2, \quad z_i \sim \mathcal{N}\left(0, 1\right), \\ \xi &= \frac{\eta_S \eta_I G \kappa N_S \left(N_S + 1\right)}{2\left(N_A' + 1\right)}, \end{aligned} \tag{3.29}$$

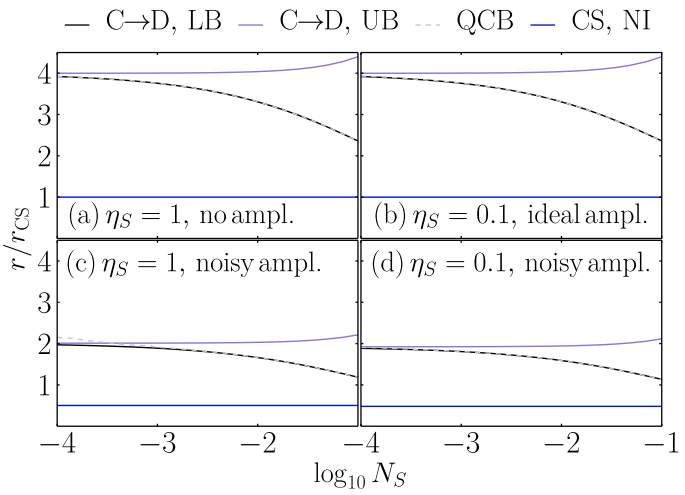

Figure 3.4: Black lines represent the ratio $r^{(\mathrm{LB})}_{\mathrm{C}\to\mathrm{D}}/r_{\mathrm{CS}}$ as a function of $\log_{10} N_S$, purple ones $r^{(\mathrm{UB})}_{\mathrm{C}\to\mathrm{D}}/r_{\mathrm{CS}}$, dashed gray for the QCB (see chapter 2), and blue ones $r^{(\mathrm{NI})}_{\mathrm{CS}}/r_{\mathrm{CS}}$, where $r^{\mathrm{NI}}_{\mathrm{CS}}$ is obtained by applying the substitution Eq. (3.20). (a) Ideal return detection, no additional signal loss $\eta_S = 1$ and therefore no amplification needed, $G = 1$. (b) Lossy return detection $\eta_S = 0.1$, assuming pure loss $N_{E_1} = 0$. We apply quantum-limited amplification of $G = 100$, $N_V = 0$. (c) Ideal return detection $\eta_S = 1$, and noisy amplification $G = 100$, $N_V = N_B$ at room temperature. (d) Lossy return detection $\eta_S = 0.1$ with noise $N_{E_1} = N_B$ at room temperature. We apply noisy amplification $G = 100$, $N_V = N_B$ at room temperature. The lower bound of the C→D module consistently aligns with the QCB.

where $\mathcal{N}(0, 1)$ denotes a Gaussian distribution with zero mean and unit variance. In the following sections, we will make extensive use of the parameter ξ, which plays a critical role in our analysis. We note that $|d_T|^2$ satisfies the χ^2 distribution Eq. (3.9), with mean $2M\xi$ and variance $4M\xi^2$. Furthermore, Eq. (3.24) can be conveniently rephrased as $E' = N'_I - 2\xi$.

3.6.1 Performance limits of the conversion module in practice

The comparison between the error exponent of the C→D module [see Eq. (3.12) and that for the upper bound, which is within the text] and the one obtained from the Quantum Chernoff Bound (QCB) (see chapter 2 for further details) can be seen in Fig. 3.4, showing that even in the worst case scenario of lossy amplification and imperfect detection, there is a factor of 2 improvement compared to the classical case Eq. (3.13). Furthermore, it is

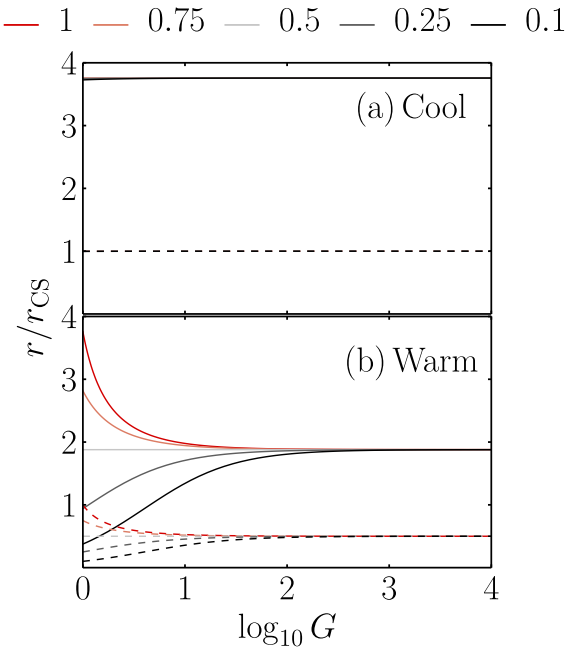

Figure 3.5: The impact of losses and gain on two scenarios: (a) a cool case with $N_V = N_{E_1} = 0.1$ (corresponding to $T_S = 100$ mK) and (b) a warm one with $N_V = N_{E_1} = N_B$ (corresponding to $T_S = 300$ K). The other parameters are fixed at $N_B = 1250$, $\kappa = 0.01$, $N_S = 10^{-3}$, and $\eta_I = 1$ (i.e., we assume the idler is ideally stored). Solid lines represent the ratio $r^{(\mathrm{LB})}_{\mathrm{C}\to\mathrm{D}}/r_{\mathrm{CS}}$ as a function of the gain $\log_{10} G$, for different values of η_S (visible in the legend); dashed lines $r^{(\mathrm{NI})}_{\mathrm{CS}}/r_{\mathrm{CS}}$, where $r^{\mathrm{NI}}_{\mathrm{CS}}$ is obtained by applying the substitution Eq. (3.20). Amplification is not necessary in a cool environment (a), but it is crucial in practical cases characterized by warm environments (b) where $\eta_S < 1/2$: only through amplification can a factor of 2 advantage be achieved.

worth noting that the lower bound of the conversion module consistently exhibits a close alignment with the QCB.

The plots in Fig. 3.5 provide evidence for the importance of an amplification stage in the microwave domain, where losses from detection may be challenging to overcome. It compares the ratio $r^{(\mathrm{LB})}_{\mathrm{C}\to\mathrm{D}}/r_{\mathrm{CS}}$ with $r^{(\mathrm{NI})}_{\mathrm{CS}}/r_{\mathrm{CS}}$ versus $\log_{10} G$, in two different temperature conditions (cool and warm). It can be seen that amplification is not necessary in a cool environment, but it is crucial in practical cases characterized by warm environments where $\eta_S < 1/2$: only through amplification can a factor of 2 advantage be achieved, with the emergence of an optimal value of G. In the later part of the paper, we will refer to the parameter setting above as either the 'cool case' or the 'warm case', referring to the

processing temperature of the returned signal.

3.6.2 Kennedy receiver

Let us now study the performance of the C↛D module in the case of a specific detection scheme of the conditional idler state. A simple idler's detection scheme is the classical Kennedy receiver, described by the set of POVMs $\Pi_0 = |0\rangle\langle 0|$ and $\Pi_1 = \mathbb{1} - \Pi_0$, where $\mathbb{1}$ is the identity operator and $|0\rangle\langle 0|$ represents the absence of a photon. The receiver operates in the on/off mode and distinguishes between the presence or absence of a photon.

A practical approach to implement such a receiver is described in Ref. [6], where the authors introduce a method based on a photo-current and photo-counting discriminator. While the calibration and measurement of every parameter in their system are rather complex, the basic idea is to use a dispersive qubit to read out single photons in a regime where the probability of having more than one photon is low.

We present a simple approach that provides useful insights and motivates the adoption of a Kennedy receiver, but we will not employ it for our analysis. In the limit where the number of signal photons $N_S \ll 1$ is low, the receiver (neglecting experimental limitations) accurately selects $|0\rangle$ as the measurement outcome. However, the uncertainty in the decision arises from the fluctuations in the coherent state $|\alpha\rangle$. When the least probable classical situation $p_0 = p_1 = 1/2$ is considered, the error probability can be calculated as [123]

$$p_e = \frac{1}{2}\langle\alpha|\,\Pi_1\,|\alpha\rangle = \frac{1}{2}\mathrm{e}^{-|\alpha|^2} \sim 2P_{\mathrm{H}} \Rightarrow P_K \sim 2P_{\mathrm{C}\not\to\mathrm{D}}, \tag{3.30}$$

when $|\alpha| \gg 1$ [see Eq. (3.10)] .

Nevertheless, the idler photon counting formula Eq. (3.30) only considers the ideal case of vacuum versus coherent state. To account for deviations from this ideal scenario, we introduce a Kennedy receiver that attempts to discriminate between two differently displaced thermal states at finite N_S. In the P-representation, the two density operators to

be distinguished are described by [50]

$$\rho_{th}(\delta) = \int_{\mathbb{C}} \frac{d^2\beta}{\pi N_T} \exp\left[-\frac{|\beta-\delta|^2}{N_T}\right] |\beta\rangle\langle\beta|, \tag{3.31}$$

where $\delta = \left\{0, \sqrt{x}\right\}$ is the phase-space displacement, and $N_T = N_I' - \{0, 2\xi\}$ represents the average number of photons produced by thermal noise, with N_I' and ξ defined in Eqs. (3.23) and (3.29), respectively. The error probability can then be calculated using the two POVMs as

$$\begin{aligned} p_e &= p_0 \mathrm{Tr}\left[\Pi_1 \rho_{th}(0)\right] + p_1 \mathrm{Tr}\left[\Pi_0 \rho_{th}(\alpha)\right] \\ &= p_0 \left\{\mathbb{1} - \mathrm{Tr}\left[\Pi_0 \rho_{th}(0)\right]\right\} + p_1 \mathrm{Tr}\left[\Pi_0 \rho_{th}(\alpha)\right], \end{aligned} \tag{3.32}$$

where $\mathrm{Tr}\left[\Pi_0 \rho_{th}(\delta)\right] = \exp\left(-\frac{|\delta|^2}{N_T+1}\right) / (N_T+1)$ [see Eq. (E1) of Ref. [125]]. Applied to our case, the least classical probability situation $p_0 = p_1 = 1/2$ yields

$$p_e = \frac{1}{2}\left[1 + \frac{\exp\left(-\frac{x}{N_I'+1-2\xi}\right)}{N_I'+1-2\xi} - \frac{1}{N_I'+1}\right]. \tag{3.33}$$

Finally, the error probability of the Kennedy receiver is given by

$$P_K = \int_0^{+\infty} dx\, P^{(M)}(x;\, \xi)\, p_e, \tag{3.34}$$

with $P^{(M)}(x;\, \xi)$ given in Eq. (3.9). In other words

$$P_K = \frac{1}{2\left(N_I'+1\right)}\left[\left(1 + \frac{2\xi}{N_I'+1-2\xi}\right)^{1-M} + N_I'\right]. \tag{3.35}$$

While we have adopted the Kennedy receiver in this work, it is worth noting that further performance improvements can be achieved by optimizing the displacement amplitude and consider the improved Kennedy receiver [132].

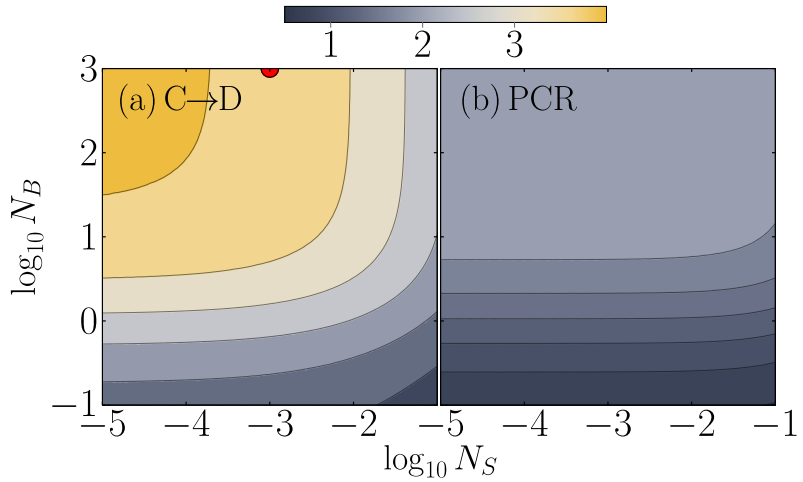

Figure 3.6: Comparison of the error exponent ratio r/r_{CS} between the C↛D module and the PCR [see Eqs. (3.12), (3.37), and (3.13), respectively] as a function of $\log_{10} N_S$ and $\log_{10} N_B$. The other parameters correspond to the 'cool' case and are set to: $N_V = N_{E_1} = N_{V_{\mathrm{PCR}}} = 0.1$ (corresponding to $T_S = 100$ mK), $N_{E_2} = 4 \times 10^{-11}$ (corresponding to $T_I = 10$ mK), $G = 100$, $G_{\mathrm{PCR}} = 2$, $\eta_S = 0.1$, and $\eta_I = 0.9$. The red circle represents the parameters used in Fig. 3.7. The C↛D module possesses clear better performance, as stated by the wide yellowish areas.

3.7 Performance benchmarks

In order to assess the performance of the C↛D module, we compare it with a classical benchmark based on coherent states and homodyne detection. The error probability of homodyne detection is given by [134]

$$P_{\mathrm{E,\,homo}} = \frac{1}{2}\,\mathrm{erfc}\left[\sqrt{\frac{\kappa M N_S}{2\,(2N_B+1)}}\right], \tag{3.36}$$

where $\mathrm{erfc}[z] = \left(2/\sqrt{\pi}\right)\int_z^{+\infty} dt\, e^{-t^2}$ is the complementary error function.

Besides the classical scheme, we also benchmark with known practical receivers for QI such as the PCR scheme [54, 123], whose error probability in the QI scenario is simply given by

$$
\begin{aligned}
P_{\mathrm{E,PCR}} &= \frac{1}{2}\,\mathrm{erfc}\left(\sqrt{R_{\mathrm{PCR}}M}\right), \\
R_{\mathrm{PCR}} &= \frac{\mu_1^2}{4}\Big[2N_I' + (G_{\mathrm{PCR}}-1)\,(2N_I'+1)\left(N_A' + N_{A,\,\kappa=0}' + 2\right) \\
&\quad + \mu_1^2/2 + 2G_{\mathrm{PCR}}N_{V_{\mathrm{PCR}}}\Big]^{-1},
\end{aligned}
\tag{3.37}
$$

where μ_1 is given by Eqs. ((3.53)), and G_{PCR} and $N_{V_{\mathrm{PCR}}}$ correspond to the gain and mean number of added photons of the phase conjugator, respectively. Fig. 3.6 shows a comparison between the performance limits of the C↛D module and PCR in terms of error exponents [see Eqs. (3.12) and (3.37), respectively]. Although we only present the performance analysis for the cool case of return signal processing, it is noteworthy that the C↛D module exhibits superior performance compared to the PCR, as evidenced by a significantly larger region of parameter space with better performance, as indicated by the yellow coloration.

The scaling of major error probabilities with the number of copies M is shown in Fig. 3.7, for both the warm and cool cases. Note that the parameter setting of Fig. 3.7 corresponds to the red dot in Fig. 3.6. Specifically, we focus on the performance of the C↛D module with Kennedy receiver (red lines), which is almost comparable to that of the QCB (blue) and outperforms any other practical scheme considered. The saturation of the C↛D performance is due to the on-off detection of Kennedy receiver, as we will resolve in Sec. 3.8. We also present the comparison to the Nair-Gu lower bound [96] (light gray), which shows similar scaling of the QCB. In Fig. 3.6, the dashed curves are the performance curves of the receivers assuming all equipment become ideal, instead the solid curves where imperfections are considered (the same color coding of the curves are adopted for both dashed and solid, as indicated by the legend). To provide a comparison between the C↛D module equipped with an on/off Kennedy receiver and the PCR, Fig. 3.8 presents the error probability ratio $\log_{10}\left(P_E/P_{\mathrm{E,\,homo}}\right)$ for the cool case, where M is chosen

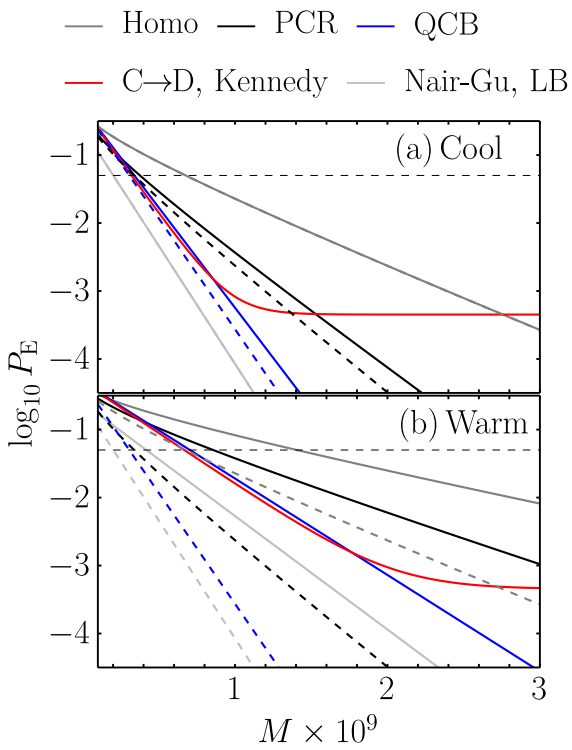

Figure 3.7: Error probability as a function of the number of copies M in both the non-ideal (solid) and ideal (dashed) case. The non-ideal case is characterised by: $N_S = 10^{-3}$, $N_B = 1250$, $N_{E_2} = 4 \times 10^{-11}$ (corresponding to $T_I = 10$ mK), $\kappa = 0.01$, $G = 100$, $\eta_S = 0.1$, $\eta_I = 0.9$, and $G_{\mathrm{PCR}} = 2$. (a) Cool case with $N_V = N_{E_1} = N_{V_{\mathrm{PCR}}} = 10^{-1}$ (corresponding to $T_S = 100$ mK), (b) warm one $N_V = N_{E_1} = N_{V_{\mathrm{PCR}}} = 1250$ (corresponding to $T_S = 300$ K). Dashed lines are the performance for each solid colored curve in the ideal scenario ($\eta_S = \eta_I = 1$ and no amplification $G = 1$). The horizontal dashed line marks $P_{\mathrm{E,\,homo}} = 0.05$.

such that the homodyne error probability is fixed at $P_{\mathrm{E,\,homo}} = 0.05$. As shown by the wide dark area, the C→D module clearly outperforms the PCR in the $N_B \gg 1$, $N_S \ll 1$ parameter regime.

3.8 Enhanced performance with number-resolving detection

So far we have adopted the Kennedy receiver with on-off detection, which leads to the saturation of error probability (red lines) in Fig. 3.7 at large M. To obtain better perfor-

mance, in this section we generalize the Kennedy receiver to a photon number resolving detector (PNRD) on the idler.

As already analyzed, the decision between the presence or absence of the target is equivalent to discriminating between two states of the final idler mode after the beamsplitter array: the thermal state $\rho_{0,N_I'}$ when the target is absent, and the displaced thermal state $\rho_{\sqrt{x},E'}$ when it is present. Recall that N_I' is defined by Eq. (3.23), E' by Eq. (3.24), and x is a random variable associated with the results of M heterodyne measurements on the return modes, distributed according to Eq. (3.9), with ξ given by Eq. (3.29). With a PNRD detection, we can now compare the photon number probability distributions for the two hypotheses: $p_n^{(0)} = \langle n|\rho_{0,N_I'}|n\rangle$ and $p_n^{(1)}(x) = \langle n|\rho_{\sqrt{x},E'}|n\rangle$. The presence of the target is declared when the outcome of the photon number measurement is greater than a predetermined threshold value, $n \geq n_D \geq 1$.

To prepare our analyses for the ROC curve, we consider the false alarm probability P_F and the detection probability P_D for a fixed decision threshold n_D as

$$P_F = \sum_{n=n_D}^{+\infty} \langle n|\rho_{0,N_I'}|n\rangle\,, \tag{3.38}$$

$$P_D = \sum_{n=n_D}^{+\infty} \int_0^{+\infty} dx\, P^{(M)}(x;\xi)\,\langle n|\rho_{\sqrt{x},E'}|n\rangle\,, \tag{3.39}$$

where we average over the random variable x.

The evaluation of P_F is simple and one has

$$P_F(n_D) = \left(\frac{N_I'}{N_I'+1}\right)^{n_D}, \tag{3.40}$$

while that of P_D is more involved. We start by using the following result for the photon

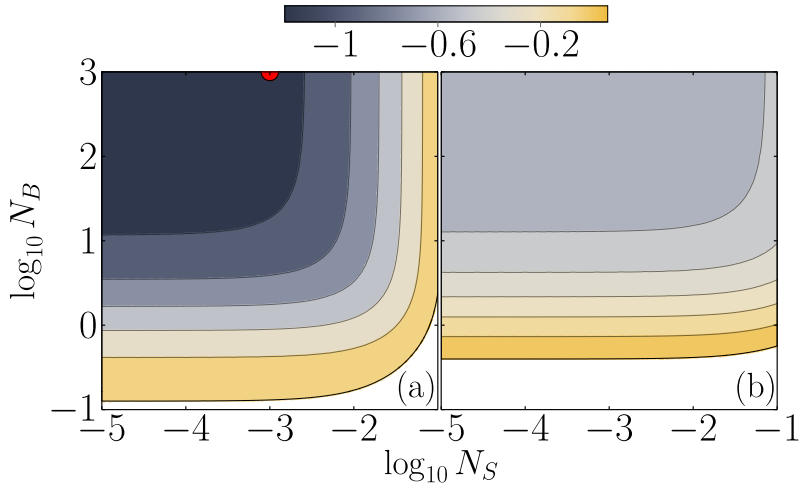

Figure 3.8: Comparison based on the error probability ratio $\log_{10}(P_E/P_{\mathrm{E,homo}})$ between (a) the C↛D module (equipped with an on/off Kennedy receiver) and (b) the PCR [see Eqs. (3.35), (3.37), and (3.36), respectively] vs. $\log_{10} N_S$ and $\log_{10} N_B$. The value of M is selected to set $P_{\mathrm{E,homo}} = 0.05$. The other parameters correspond to the 'cool' case and are: $N_V = N_{E_1} = N_{V_{\mathrm{PCR}}} = 0.1$, $N_{E_2} = 4 \times 10^{-11}$, $G = 100$, $G_{\mathrm{PCR}} = 2$, $\eta_S = 0.1$, and $\eta_I = 0.9$. The red circle indicates the parameters used in Fig. 3.7. As shown by the wide dark area, the C↛D module outperforms the PCR.

statistics of a displaced thermal state for a given x [77, 89]

$$p_n^{(1)}(x) = \frac{\exp\left(-\frac{x}{E'+1}\right)}{E'+1}\left(\frac{E'}{E'+1}\right)^n L_n\left[-\frac{x}{E'(E'+1)}\right], \tag{3.41}$$

where $L_n[\cdot]$ is the n-th Laguerre polynomial. Next, one can perform the average over the probability distribution Eq. (3.9) to obtain the average photon number probability distribution when the target is present

$$\begin{aligned}\bar{p}_n^{(1)}(M;\xi) = {} & \frac{(E'+1)^{M-n-1}E'^n}{(E'+1+2\xi)^M} \\ & \times {}_2F_1\left[M, -n, 1, -\frac{2\xi}{E'(E'+1+2\xi)}\right],\end{aligned} \tag{3.42}$$

where ${}_2F_1(a, b, c, z)$ is the Gaussian hypergeometric function. Consequently, the detec-

tion probability $P_D(n_D)$ can be exactly determined as

$$P_D(n_D) = 1 - \sum_{n=0}^{n_D-1} \bar{p}_n^{(1)}(M;\, \xi)\,. \tag{3.43}$$

3.8.1 Bayesian error probability

To begin with, we consider the symmetric error $P_E = (P_F + 1 - P_D)/2$ and evaluate the performance. Here the results are similar to that of Ref. [22]. This is because, given the choice of photon counting, random phase does not change the performance anymore. From Eqs. (3.42) and (3.40), we have the error probability P_E as a function of the threshold n_D. We compare this optimal decision strategy with a variable threshold n_D, and quantify the error of probability using

$$P_{\mathrm{C}\to\mathrm{D}}^{(n_D)} = \frac{1}{2}\left[1 - \sum_{n=0}^{n_D-1} \gamma_n(2M;\, \xi)\right], \tag{3.44}$$

where the function

$$\begin{aligned}\gamma_n(M;\, \xi) = {} & \frac{N_I'^n}{\left(N_I' + 1\right)^{n+1}} \\ & - \frac{(E'+1)^{M-n-1}E'^n}{(E'+1+2\xi)^M}\,{}_2F_1\left[M,\, -n,\, 1,\, -\frac{2\xi}{E'(E'+1+2\xi)}\right].\end{aligned} \tag{3.45}$$

Although the above equation is exact, to enable efficient numerical evaluation in all parameter region of interest, we further make an approximation at the $M \gg 1$ limit and obtain

$$\begin{aligned}\gamma_n(M;\, \xi) \simeq {} & \frac{N_I'^n}{\left(N_I' + 1\right)^{n+1}} \\ & - \frac{E'^n}{(E'+1)^{n+1}} \mathrm{e}^{-2M\xi/E'}\,{}_1F_1\left[n+1,\, 1,\, \frac{2M\xi}{E'\,(E'+1)}\right].\end{aligned} \tag{3.46}$$

The precision of such an approximation is sufficient for our evaluation, as verified in Ref. [22]. The optimal performance is then given by a minimization of the error probability over the threshold n_D,

$$P_{\mathrm{C}\to\mathrm{D}}^{(opt)} = \min_{n_D \geq 1} P_{\mathrm{C}\to\mathrm{D}}^{(n_D)}. \tag{3.47}$$

Note that $P_{\mathrm{C}\to\mathrm{D}}^{(1)} \equiv P_K$ [see Eq. (3.35)], as expected.

Fig. 3.9 shows the results of our analysis, using the same parameter values as in Fig. 3.7. We observe that the optimized approach (orange) produces results that are comparable to those of the non-ideal QCB (blue). Specifically, the irregular trend in the data is well described by a variable threshold decision strategy approach, which is represented by the dashed lines in the figure. Our findings suggest that the optimized approach can effectively discriminate between the two states of interest, even in the presence of noise and other imperfections.

3.8.2 Receiver operating characteristic

Conversion module and photon-number resolving detector

Let us now analyse the performance of the C→D module within the Neyman-Pearson framework, using ROC curves. In this approach, a chosen false alarm probability P_F is fixed, and the goal is to maximize the detection probability P_D. By gradually reducing the threshold value n_D from a high (ideally infinite) value to zero, a concave ROC curve can be obtained, plotting P_D versus P_F, starting from $P_F = P_D = 0$ and ending at $P_F = P_D = 1$.

To gain a clearer understanding of the behavior of the ROC curve, we derive an analytical expression based on a Gaussian approximation. When $x \gg 1$, the probability distribution $p_n^{(1)}(x)$ Eq. (3.41) can be represented by a Gaussian distribution with mean $\langle n(x)\rangle = E' + x$, and variance $\sigma_n^2(x) = \left\langle n^2(x)\right\rangle - \langle n(x)\rangle^2 = E'^2 + E' + x\,(2E' + 1)$. As a re-

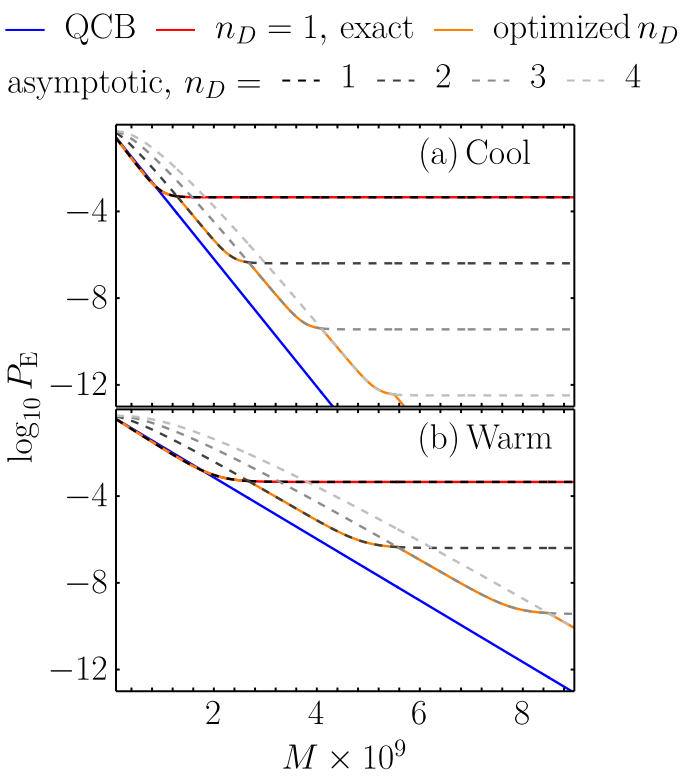

Figure 3.9: The saturation of the red line in Fig. 3.7 suggests an improvement, following the lines of Ref. [22], where a variable threshold decision strategy approach has been used for asymptotic analysis. The red curve reproduces the usual Kennedy receiver corresponding to the fixed threshold $n_D = 1$. The dashed grey lines corresponds to the case of fixed, increasing values of n_D. The orange line gives the optimized result in which n_D is adjusted according to M, and therefore to the two states to be discriminated. This latter approach yields results comparable to those of the non-ideal QCB (blue). Parameter values are the same as those of Fig. 3.7.

sult, in this limit, the average probability distribution Eq. (3.42) can also be approximated by a Gaussian distribution with properly averaged mean and variance, and we have

$$\bar{p}_n^{(1)}(M;\xi) \sim \frac{1}{\sqrt{2\pi\sigma_n^2}} \exp\left[-\frac{(n-\bar{n})^2}{2\sigma_n^2}\right], \tag{3.48}$$

with

$$\begin{aligned} \bar{n} &= E' + \bar{x} \\ &= E' + 2M\xi, \end{aligned} \tag{3.49}$$

$$\begin{aligned} \sigma_n^2 &= E'^2 + E' + \bar{x}\,(2E' + 1) + \sigma_x^2 \\ &= E'^2 + E' + 2M\xi\,(2\xi + 2E' + 1)\,, \end{aligned} \tag{3.50}$$

taking into account that the distribution Eq. (3.9) has mean $\bar{x} = 2M\xi$, and variance $\sigma_x^2 = 4M\xi^2$. A necessary condition for the validity of such a Gaussian treatment is that $\bar{x} = 2M\xi \gg 1$. By using the Gaussian approximation Eq. (3.48), and eliminating the threshold n_D with the aid of Eq. (3.40), one gets the following approximate expression for the ROC curve of the C↛D module

$$P_D\,(P_F) \sim \frac{1}{2}\,\mathrm{erfc}\left[\frac{1}{\sigma_n\sqrt{2}}\left(\frac{\log P_F}{\log\left(\frac{N_I'}{N_I'+1}\right)} - \bar{n}\right)\right]. \tag{3.51}$$

This approximation provides a satisfactory description of the ROC curves for moderate values of P_D and P_F as long as $2M\xi > 1$. Although the average probability distribution $\bar{p}_n^{(1)}\,(M;\,\xi)$ resembles a Gaussian distribution around the peak centered at its average value, it decays exponentially, not Gaussianly, for $P_F \to 0 \Rightarrow P_D \to 0$, i.e., $n_D \to \infty$. As a result, Eq. (3.51) tends to underestimate the value of P_D for high threshold values n_D.

The ROC curve in the case of the PCR

As discussed in chapter 2 (see also Ref. [127]), when $M \gg 1$, the photo-count difference of the PCR, $N = N_+ - N_-$, according to the central limit theorem, follows a Gaussian

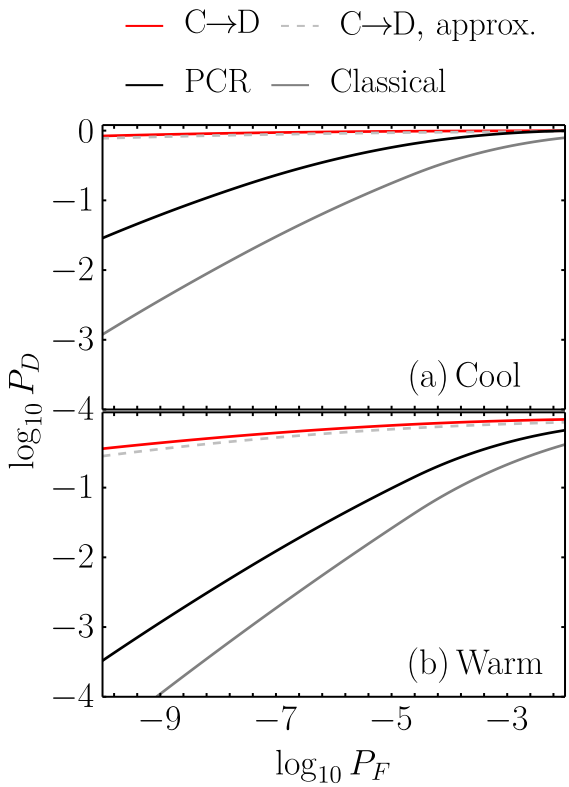

Figure 3.10: Comparison of ROC curves. The red line shows the performance of the C→D module with a PNRD; the black one that of the PCR given by Eq. (3.57); the dashed light gray line depicts the performance of the Gaussian approximation of Eq. (3.51); the full dark grey line gives the non-ideal classical benchmark [using Eq. (3.57) with $d_{\mathrm{PCR}} \to d_{\mathrm{CS}}$ plus Eq. (3.20)]. The parameters used are the same as in Fig. 3.6 and 3.8 (indicated by the red dots there), with $M = 69 \times 10^7$.

distribution with a probability density for the two hypotheses

$$P_{N|H_{0/1}}(n|H_{0/1}) = \frac{\exp\left[-\frac{(n-M\mu_{0/1})^2}{2M\sigma^2_{0/1}}\right]}{\sqrt{2\pi M\sigma^2_{0/1}}}, \tag{3.52}$$

where the two mean values $\mu_{0/1}$ and the two variances $\sigma^2_{0/1}$.

The discrimination between two Gaussian distributions with different means and variances can be obtained by using the extended van Trees approximation [119], and it can be

expressed in terms of the auxiliary function

$$\mu(s) = \ln\left\{\frac{\sigma_1^{1-s}\sigma_0^s}{\sqrt{s\sigma_0^2 + (1-s)\,\sigma_1^2}} \times \exp\left\{-\frac{M\,(\mu_0-\mu_1)^2\,s\,(1-s)}{2\left[s\sigma_0^2 + (1-s)\,\sigma_1^2\right]}\right\}\right\}, \tag{3.53}$$

where s is a threshold parameter. The false alarm and detection probabilities are then respectively given by

$$\begin{aligned} P_F &= \frac{1}{2}\mathrm{erfc}\left[s\sqrt{\frac{\ddot{\mu}(s)}{2}}\right], \\ P_D &= 1 - \frac{1}{2}\mathrm{erfc}\left[(1-s)\sqrt{\frac{\ddot{\mu}(s)}{2}}\right], \end{aligned} \tag{3.54}$$

where $\ddot{\mu}(s) \equiv d^2\mu/ds^2$.

However, one can get a simpler and clearer expression by taking into consideration that the variances for the two hypothesis, σ_0^2 and σ_1^2, are nearly identical for the typical parameter values in a microwave QI experiment, that is, when $\kappa \ll 1$, $N_S \ll 1$, and $N_B \gg 1$.

$$\begin{aligned} \frac{\sigma_1^2 - \sigma_0^2}{\sigma_0^2} &= \eta_S G\,(G_{\mathrm{PCR}} - 1)\,\kappa N_S\,\left[2N_I' + 1 + 2\eta_I\,(N_S + 1)\right] \\ &\times \left[N_I' + (G_{\mathrm{PCR}} - 1)\,(2N_I' + 1)\left(N_{A,\,\kappa=0}' + 1\right) + G_{\mathrm{PCR}} N_{V_{\mathrm{PCR}}}\right]^{-1}, \end{aligned} \tag{3.55}$$

which scales as $\kappa N_S/N_B \ll 1$ when $N_B \gg N_S$. As a result, one has $\ddot{\mu}(s) = M\mu_1^2/\sigma_1^2 \equiv d_{\mathrm{PCR}}^2$

in Eqs. (3.54), which can be rewritten as

$$\begin{aligned} P_F &= \frac{1}{2}\mathrm{erfc}\left[\frac{1}{\sqrt{2}}\left(\frac{\ln\eta}{d_{\mathrm{PCR}}}+\frac{d_{\mathrm{PCR}}}{2}\right)\right], \\ P_D &= \frac{1}{2}\mathrm{erfc}\left[\frac{1}{\sqrt{2}}\left(\frac{\ln\eta}{d_{PCR}}-\frac{d_{\mathrm{PCR}}}{2}\right)\right], \end{aligned} \tag{3.56}$$

where we introduce the new threshold parametrization as $\ln\eta = (s-1/2)\,d_{\mathrm{PCR}}^2$. By eliminating this threshold parameter, the analytical expression of the ROC curve for the PCR can be obtained as

$$P_D = \frac{1}{2}\mathrm{erfc}\left[\mathrm{erfc}^{-1}\left(2P_F\right) - \frac{d_{\mathrm{PCR}}}{\sqrt{2}}\right], \tag{3.57}$$

where $\mathrm{erfc}^{-1}(z)$ is the inverse of the complementary error function. We notice that the ROC curve for the PCR is analytically identical to that of the optimal classical benchmark of using coherent states and homodyne detection. Both have the same form as in Eq. (3.57), but the replacement $d_{\mathrm{PCR}} \to d_{\mathrm{CS}} = 2\sqrt{M\kappa N_S/(2N_B+1)}$ [127].

Fig. 3.10 presents the behavior of the ROC curve for the C↛D module in both warm and cool cases, considering losses and amplification in the detection scheme. The results are compared to the corresponding Gaussian approximation Eq. (3.51), the PCR Eq. (3.57), and the non-ideal classical benchmark [using Eq. (3.57) with $d_{\mathrm{PCR}} \to d_{\mathrm{CS}}$ and Eq. (3.20)], all obtained under the same experimental conditions.

When the Neyman-Pearson decision strategy is considered, it can be observed that the C↛D module exhibits excellent performance in both the cool and warm cases. In particular, its ROC curve is significantly larger than those obtained with the PCR and the classical approach for the same experimental conditions.

Chapter 4

Synthesis of Entanglement

The aim of this chapter is to introduce the spin system and important definitions that will be used throughout the thesis work. Specifically, Sec. 4.1 covers quantum entanglement , which plays a fundamental role in many aspects of the rest of the chapter.

Sec. 4.7 discusses the generation and properties of photon states, mainly qubit representation, which are used in many protocols and enter into the description of quantum W state which we will study in the following. Mainly focusing on the W state generation circuit QED setup.

Sec. 4.5 also introduces the spin system, which is used to represent the qubit and used in many body system particularly generation of W state. Finally, Sec. 4.6 explains the generation of W state atom-photon interaction in the Dicke model cavity QED setup. For readers interested in more details, references and books on Dicke model, synthesis of W state in quantum computer and quantum information theory and quantum optics are provided.

The rest of the chapter discusses the W state that has been generated successfully and the various proposals that have been made for its synthesis. The preparation of entanglement is therefore a central objective of quantum information theory (QIT). Recently, several methods for producing entangled states have been proposed, including nuclear

magnetic resonance (NMR), parametric down-conversion, cavity quantum electrodynamics (QED), single-photon interference, and ion trap techniques. This chapter focuses on two different W state generation setups, specifically circuit QED setup [61,143] and Dicke model cavity QED setup [48,66].

4.1 Quantum Entanglement

In quantum mechanics, quantum entanglement arises when two or more particles become interconnected to the extent that the state of one particle immediately influences the state of the others, regardless of their spatial separation. Entangled particles, like photons, electrons, or atoms, exhibit interdependent properties, making it impossible to describe one particle's state in isolation from the others. This phenomenon has garnered significant interest due to its profound implications and practical applications in quantum computing, quantum communication, and quantum cryptography. It challenges traditional notions of particle independence. Many studies are still being conducted on the existence of entangled, inseparable states, especially in relation to quantum information theory and the EPR paradox [35,63]. This phenomenon can be seen in correlation experiments, such as those involving the Bell theorem, which states that classical correlations cannot account for the probabilities of outcomes obtained from specific quantum states when measured properly.

In Chapter 2, we explored the continuous variable theory and its applications in various areas involving entanglement. Now, in this chapter, our focus shifts to discrete variable entanglement theory. The fundamental challenge in quantum entanglement theory is identifying which states are entangled and which are not. Few situations provide a straightforward answer to this question. Pure bipartite states represent one of the few cases where the scenario is relatively simple. In the case of a bipartite pure state, a state is considered entangled if and only if it cannot be expressed as the product of two vectors

corresponding to the Hilbert spaces of the individual subsystems. That is, as the smaller of $|\Psi\rangle_{AB} \in H_{AB} = H_A \otimes H_B$:

$$|\Psi\rangle_{AB} = |\phi\rangle_A \otimes |\psi\rangle_B. \tag{4.1}$$

The vector $|\Psi\rangle_{AB}$ is written in any set of orthonormal product basis $\{ |e\rangle_A^m \otimes |e\rangle_B^n \}$,

$$|\Psi\rangle_{AB} = \sum_{m=0}^{d_A-1} \sum_{n=0}^{d_B-1} A_{mn}^{\Psi} |e\rangle_A^m \otimes |e\rangle_B^n, \tag{4.2}$$

It becomes a product state if and only if the coefficient matrix can be factorized $A^{\Psi} = \{ A_{mn}^{\Psi} \}$ is of rank 1. In general, the rank $r(|\Psi\rangle) \leq k = \min[d_A, d_B]$ of this matrix is called the Schmidt rank of vector Ψ and it is equal to either of the ranks of the reduced density matrices $\rho_A^{\Psi} = Tr_A [|\Psi\rangle_{AB}\langle\Psi|]$ and $\rho_B^{\Psi} = Tr_B [|\Psi\rangle_{AB}\langle\Psi|]$. The vector takes the Schmidt decomposition,

$$|\Psi\rangle_{AB} = \sum_{j=0}^{r(|\Psi\rangle)} C_j \, |\tilde{e}\rangle_A^j \otimes |\tilde{e}\rangle_B^j \tag{4.3}$$

In this case, the nonzero singular eigenvalues of matrix A_{mn} are represented by the positive numbers $C_j = \sqrt{p_j}$, where p_j are the nonzero elements obtained from the reduced density matrix's spectrum. Quantum entanglement remains unchanged regardless of product unitary operations $U_A \otimes U_B$. In a pure bipartite state represented by a projector $|\Psi\rangle_{AB}\langle\Psi|$, the coefficients C_j are the only parameters unaffected by these operations and determine the entanglement of a bipartite pure state.

4.2 Density Operator

In the case of a mixed state, i.e., with purity less than one, one has to use the density operator formalism. The density operator representing a set of states and probabilities

$\{\Psi_i,\ p_i\}$ is

$$\rho = \sum_{i=1}^{n} p_i |\Psi_i\rangle\langle\Psi_i|. \tag{4.4}$$

If the state of a system is known exactly, we say it is pure state. This is a state where a single $p_i = 1$, and all others are zero. This means that the density operator for a pure state $|\psi\rangle$ can be written as

$$\rho = |\psi\rangle\langle\psi|. \tag{4.5}$$

This is a projection operator, so in the case of a pure state, the density operator satisfies $\rho^2 = \rho$. A mixed state is a collection of different pure states, each occurring with given probability.

4.3 Entanglement Entropy

In Eqn, (4.3), the Schmidt decomposition theorem is an extremely helpful tool to find the entanglement entropy for the subsystem. Assuming we have a system AB in a pure state $|\Psi\rangle$, given by the Schmidt decomposition of Eq. (4.3) we can evaluate the so-called entanglement entroy S_A, coinciding with the von Neumann entropy of the reduced density matrix of system A and B

$$S_A = -\sum_j C_j^2 \log C_j^2, \tag{4.6}$$

The entanglement entropy iszero for unentangled states and maximal when all the C_j are equal, it is convex: $S_{A_1 \cup A_2} \leq S_{A_1} + S_{A_2}$.

4.4 Qubit representation

In Chapter 2, we explored number states in coherent states and two-mode squeezed states derived from harmonic oscillators photon number state $|n\rangle$. Similar to classical bits (0 and

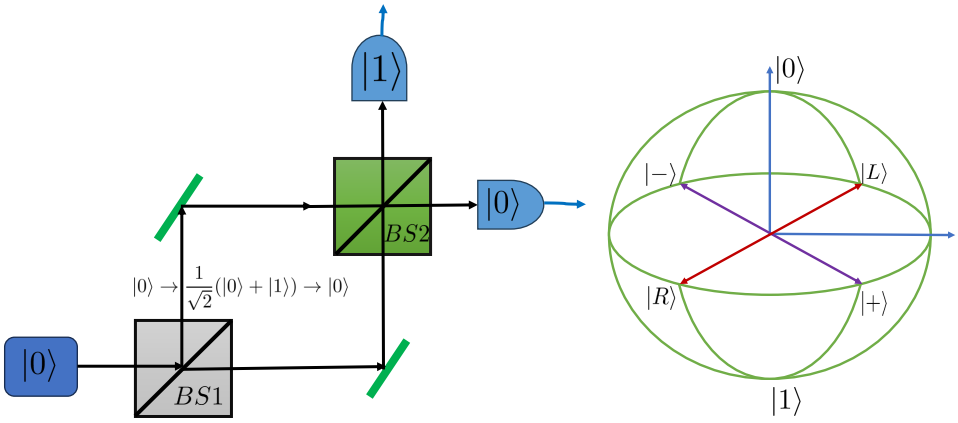

Figure 4.1: Beam Splitter

1), qubits are fundamental units in quantum computing and quantum information theory. Qubits, also known as quantum bits, can exist in states analogous to $|0\rangle$ and $|1\rangle$ photon path or polarization states and two level spin system $|\uparrow\rangle$ and $|\downarrow\rangle$, akin to their classical counterparts [98]. The representation of qubits are:

$$|1\rangle \equiv \begin{pmatrix} 1 \\ \\ 0 \end{pmatrix}, |0\rangle \equiv \begin{pmatrix} 0 \\ \\ 1 \end{pmatrix} \tag{4.7}$$

Qubits, in contrast to classical bits, are capable of existing in superpositions $|\psi\rangle = \alpha|0\rangle + \beta|1\rangle$, where $|\alpha|^2 + |\beta|^2 = 1$ and simultaneously representing 0 and 1. In Fig. 4.1, superposition states can be created by a beam splitter, a fundamental optical device in quantum optics. When quantum particles, such as photons, collide with a beam splitter, a probabilistic process determines whether they are transmitted or reflected. This probabilistic nature allows superposition states to form. Take a single photon incident upon a balanced beam splitter, for instance. The quantum superposition principle allows a photon in the state of $|0\rangle$, which is the absence of the photon, to simultaneously be transmitted ($|0\rangle$) and reflected ($|1\rangle$) when it comes into contact with the beam splitter. In terms of

Bloch sphere representation in Fig. 4.1, this is represented as:

$$|\pm_{photon}\rangle = \frac{1}{\sqrt{2}}(|0\rangle \pm |1\rangle). \tag{4.8}$$

This illustrates how a photon can create a superposition state in which it is simultaneously in two different "path encoded" states.

4.4.1 Two-level system

The simplest system that can exist for a single atom is the isolation of two states, which turns the atom into a pseudo spin-1/2. Then, there are only two states that make up the basis: $|0\rangle$ and $|1\rangle$. The atomic wavefunction then exists in a superposition.

$$|\psi\rangle = \alpha|0\rangle + \beta|1\rangle = \begin{pmatrix} \alpha \\ \\ \beta \end{pmatrix}, \tag{4.9}$$

where α and β are complex numbers that satisfies the $|\alpha|^2 + |\beta|^2 = 1$. More generally, it exists in some density matrix which is hermitian, positive and with trace equal to one.

$$\hat{\rho} = \begin{pmatrix} C_{00} & C_{01} \\ \\ C_{10} & C_{11} \end{pmatrix}, \tag{4.10}$$

where for the pure state

$$\hat{\rho} = |\psi\rangle\langle\psi| = \begin{pmatrix} |\alpha|^2 & \alpha\beta^* \\ \\ \alpha^*\beta & |\beta|^2 \end{pmatrix}. \tag{4.11}$$

Any non trivial hermitian operator acting on the state for a spin-1/2 particle can be

described by a combination of the Pauli operators,

$$\begin{aligned}
\hat{\sigma}_x &= |0\rangle\langle 1| + |1\rangle\langle 0| = \begin{pmatrix} 0 & 1 \\ 1 & 0 \end{pmatrix} \\
\hat{\sigma}_y &= i\left(|0\rangle\langle 1| - |1\rangle\langle 0|\right) = \begin{pmatrix} 0 & i \\ -i & 0 \end{pmatrix} \\
\hat{\sigma}_z &= |1\rangle\langle 1| - |0\rangle\langle 0| = \begin{pmatrix} -1 & 0 \\ 0 & 1 \end{pmatrix}.
\end{aligned} \tag{4.12}$$

These matrices each have two eigenvectors and eigenvalues ± 1.

$$\begin{aligned}
|x_\pm\rangle &= \frac{1}{\sqrt{2}}(|0\rangle \pm |1\rangle) \\
|y_\pm\rangle &= \frac{1}{\sqrt{2}}(|0\rangle \mp |i1\rangle) \\
|z_-\rangle &= |0\rangle, \quad |z_+\rangle = |1\rangle.
\end{aligned} \tag{4.13}$$

The way each pair of eigenvectors spans the operator space is similar to how the Pauli operators span the state space. An alternative method involves connecting these three sets to a unit-radius sphere's axes, thereby projecting the state onto it. There is explicit mention of the sphere's condition, as shown in Fig. 4.1

$$|\psi\rangle = \sin\left(\frac{\theta}{2}\right)|0\rangle + \mathrm{e}^{i\phi}\cos\left(\frac{\theta}{2}\right)|1\rangle, \tag{4.14}$$

where the spherical coordinate variables ϕ and θ are defined. The state represented in this manner is the Bloch vector, and this is the Bloch sphere.

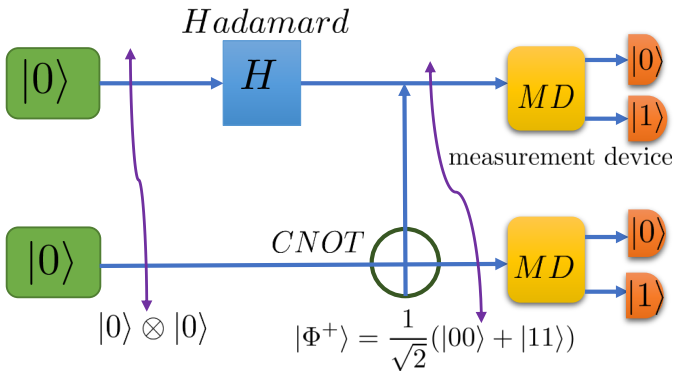

Figure 4.2: Bell state preparation

4.4.2 Bell state

Quantum gates are utilized to manipulate various physical systems, such as superconducting circuits and atoms, in order to perform quantum computations [98, 155]. Leveraging superconducting circuits enables the creation of maximally entangled states [69, 92]. In the two-bit context is shown in Fig. 4.2, this entangled state is referred to as a Bell state.

$$
\begin{aligned}
|\Phi^{\pm}\rangle &= \frac{1}{\sqrt{2}}\left(|00\rangle \pm |11\rangle\right) \\
|\Psi^{\pm}\rangle &= \frac{1}{\sqrt{2}}\left(|10\rangle \pm |01\rangle\right).
\end{aligned}
\tag{4.15}
$$

In quantum technology, the use of maximally entangled Bell states has significant advantages [146]. These states, for example, are critical in understanding quantum teleportation, demonstrating the advantages of entanglement over classical bits. In Fig. 4.2, two initially independent $|0\rangle$ states are prepared in the direct product state, with the first qubit undergoing a Hadamard gate operation and the second qubit undergoing a CNOT gate operation. As a result, the final state becomes maximally entangled. In the case where Alice measures the first qubit and Bob measures the second, both measurements have a 50% chance of being detected. Even when these qubits are separated by great distances, such as Alice on Earth and Bob on the Moon, the results of their measurements remain

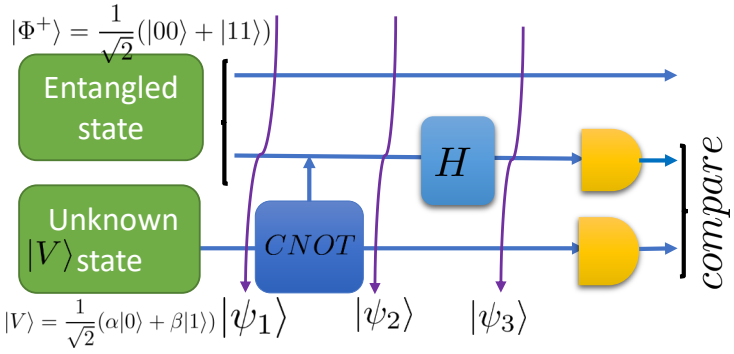

Figure 4.3: Bell state Teleportation

the same, Alice strings: 0010110001101011 and Bob strings: 0010110001101011 in the measurement outcome. In the second scenario, as shown in Fig. 4.3, the unknown state $|V\rangle$ is provided along with an entangled Bell state. These states undergo quantum gate operations, leading to a final state. Measurement outcomes are determined based on this process. The initial direct product state $|\psi_1\rangle$,

$$\begin{aligned} |\psi_1\rangle &= \left\{\frac{|0\rangle|0\rangle + |1\rangle|1\rangle}{\sqrt{2}}\right\} \otimes \frac{1}{\sqrt{2}}(\alpha|0\rangle + \beta|1\rangle) \\ &= \frac{1}{\sqrt{2}}\{\alpha|0\rangle|0\rangle|0\rangle + \beta|0\rangle|0\rangle|1\rangle + \alpha|1\rangle|1\rangle|0\rangle + \beta|1\rangle|1\rangle|1\rangle\} \end{aligned} \tag{4.16}$$

Action of $CNOT$ gate,

$$\begin{aligned} |\psi_2\rangle &= \frac{1}{\sqrt{2}}\{\alpha|0\rangle|0\rangle|0\rangle + \beta|0\rangle|0\rangle|1\rangle + \alpha|1\rangle|1\rangle|0\rangle + \beta|1\rangle|1\rangle|1\rangle\} \\ &= |0\rangle(\alpha|0\rangle|0\rangle + \beta|0\rangle|1\rangle) + |1\rangle(\alpha|1\rangle|1\rangle + \beta|1\rangle|0\rangle) \\ |\psi_3\rangle &= \frac{1}{2}\{(\alpha|0\rangle|00\rangle + \beta|1\rangle) + (\alpha|1\rangle + \beta|0\rangle))|01\rangle \\ &\quad + (\alpha|0\rangle + \beta|0\rangle))|10\rangle + (\alpha|1\rangle + \beta|0\rangle))|11\rangle\}. \end{aligned} \tag{4.17}$$

The Bob's measurement outcome of $|00\rangle$ occurs with a 25% probability. In Alice's case, if the outcome is $|00\rangle$, the unknown qubit is represented as $(\alpha|0\rangle + \beta|1\rangle)$, and if the outcome is $|01\rangle$, the unknown qubit is $(\alpha|1\rangle + \beta|0\rangle)$. Likewise, the outcomes $|00\rangle$ and $|00\rangle$

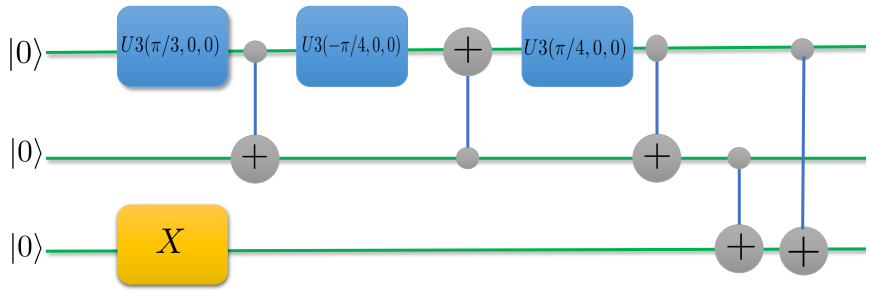

Figure 4.4: A circuit to create a perfect W-state involves using the Pauli X-gate and the general unitary gate $U3(\theta, \Phi, \lambda)$.

each occur with a 25% probability.

Similarly, we can generate the W state in the three-qubit system's circuit QED setup. We will study in the following how to generate W states for spin systems.

4.4.3 W state synthesis

The W-state is a type of multipartite entangled state that is well-known for its ability to withstand particle loss. The following is the usual expression for the W-state:

$$|W\rangle = \sum p_l \, |1_l, \{0\}\rangle, \quad \sum |p_l|^2 = 1. \tag{4.18}$$

If $p_l = \frac{1}{\sqrt{N}}$ (N is the number of qubits) is chosen, the resulting state is known as the maximally entangled W state, which is denoted as,

$$|W\rangle = \frac{1}{\sqrt{N}} \left(|100\ldots0\rangle + |010\ldots0\rangle + \ldots\cdots + |0\ldots001\rangle\right). \tag{4.19}$$

The maximally entangled W-state has been successfully created in experimental settings [72, 81, 150] and numerous theoretical proposals [4, 33, 130]. The three-qubit entangled perfect W-state given in Eq. (4.19) has been successfully produced in a variety of experimental setups as shown in Fig. 4.19, using IBM's five-qubit quantum computers [38, 51, 67, 90, 148].

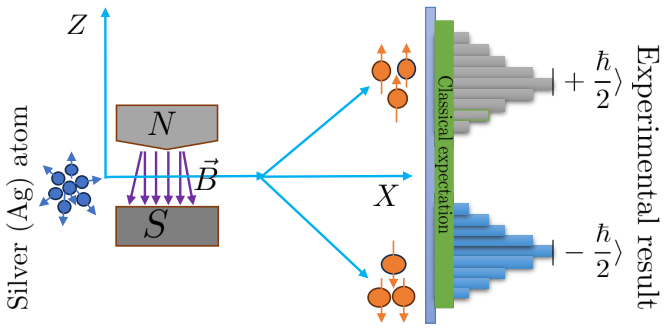

Figure 4.5: Silver atoms are heated in an oven with a small opening, allowing some atoms to escape. The emitted atoms pass through a non-homogeneous magnetic field created by pole pieces.

4.5 Spin system

We discussed photon entangled states and the implications they carry in the qubit representation. These entangled states are similar to maximally entangled spin-related qubit states. The fundamental concept underlying the Stern-Gerlach experiment's observation of spin behavior. In Fig. 4.5, a well-known physics experiment used to show how particle spin is quantized is the Stern-Gerlach experiment. In this experiment, an inhomogeneous magnetic field produced by a set of magnetic poles is passed through by a beam of particles, typically silver atoms or other particles with magnetic moments [113]. The beam is deflected into discrete, distinct lines as a result of the experiment, suggesting that the magnetic moments of the particles are quantized and can only have particular orientations. Important support for the quantized character of intrinsic angular momentum, or spin, in quantum mechanics was given by this observation.

An atom's initial wavefunction can be used to write a superposition state,

$$|\psi_{spin}\rangle = \frac{1}{\sqrt{2}}(|\uparrow\rangle + |\downarrow\rangle). \tag{4.20}$$

The Sequential Stern-Gerlach experiment poses intriguing questions. In Fig. 4.6.(a) setup, the remaining particles with S_z+ spin component pass through a second SG_z ap-

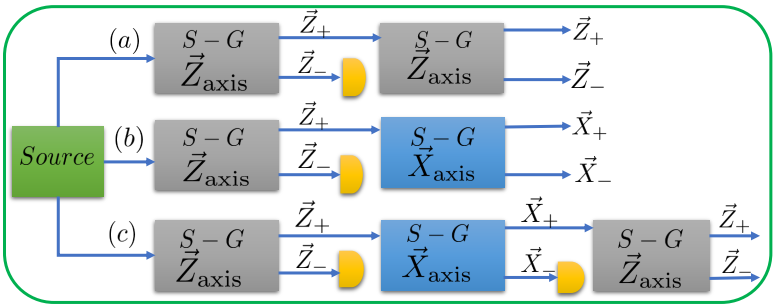

Figure 4.6: Collapse wavefunction measurement

paratus, while those with S_z- spin component are blocked after the first apparatus. As anticipated, only the S_z+ component emerges from the second apparatus. This outcome is unsurprising, given that without external influences, the spins of atoms are expected to remain unchanged between the first and second SG_z apparatuses.

The setup depicted in the Fig. 4.6.(b) adds an intriguing twist to the experiment. In this configuration, the first apparatus (SG_z) remains the same, but the second one (SGX :) features an inhomogeneous magnetic field in the x-direction. When the S_z+ beam enters the second apparatus (SGX :), it splits into two components: an S_x+ component and an S_x- component, each with equal intensities. One might wonder if this implies that 50% of the atoms in the S_z+ beam from the first apparatus (SG_z) possess both S_z+ and S_x+, while the remaining 50% have both S_z+ and S_x-. However, this interpretation encounters challenges, as we will explore below. Moving forward, we delve into a third step, as illustrated in the subsequent Fig. 4.6, which vividly highlights the peculiar nature of quantum-mechanical systems.

In this scenario, a third apparatus of the SGz type is added to the setup depicted in the Fig. 4.6.(c). Surprisingly, the experiment reveals that two components emerge from this third apparatus: one with an S_z+ component and another with an S_z- component. This outcome is unexpected because efforts were made to block the S_z-component after the atoms passed through the first apparatus. The reappearance of the S_z-component raises the question of how it could persist despite our previous attempts to eliminate it. The existing

model, which assumes that atoms entering the third apparatus have both S_z+ and S_x+ components, is clearly inadequate to explain this phenomenon. This example is frequently cited to demonstrate the principle in quantum mechanics that we cannot simultaneously determine both S_z and S_x. Specifically, when the second apparatus (SGx) selects the S_x+ beam, it erases any prior information about the S_z property of the particles and it is called the wavefunction collapses. In Eqn. 4.7 is similarly to the two spin-1/2 particles (say two electrons) representation $|\uparrow\rangle = |s = 1/2, m = 1/2\rangle$ and $|\downarrow\rangle = |s = 1/2, m = -1/2\rangle$ are,

$$|\uparrow\rangle \equiv \begin{pmatrix} 1 \\ \\ 0 \end{pmatrix}, |\downarrow\rangle \equiv \begin{pmatrix} 0 \\ \\ 1 \end{pmatrix}. \tag{4.21}$$

4.5.1 Collective spin operators

Quantum optics [24] and condensed matter theory are extensively studied, particularly in the context of angular momentum. For a comprehensive understanding of these topics, I have included references that delve into these subjects [2, 28].

For two spin-1/2 particles (say, two electrons), the total spin operators is usually written as

$$S = S_1 + S_2 \tag{4.22}$$

but again it is to be understood as

$$S = S_1 \otimes 1 + 1 \otimes S_2 \tag{4.23}$$

Where 1 is the identity operator in the spin space of electron.

The usual commutation relations are,

$$[S_{1x}, S_{1y}] = i\hbar S_{1z}, \quad [S_{2x}, S_{2y}] = i\hbar S_{2z}, \quad [S_x, S_y] = i\hbar S_z.$$

The eigenvalues of the various spin operators are denoted as follows

$$S^2|s, m_z\rangle = s(s+1)\hbar^2|s, m_z\rangle, \quad S_z|s, m_z\rangle = m_z\hbar|s, m_z\rangle, \tag{4.24}$$

Again, we can expand the ket corresponding to an arbitrary spin state of the two electrons in terms of either the eigenkets of S^2 and S_z or the eigenkets of S_{1z} and S_{2z}. The two possibilities are as follows,

1) The $\{m_1, m_2\}$ representation based on the eigenkets of S_{1z} and S_{2z}

$$|++\rangle, \ |+-\rangle, \ |-+\rangle, \ |--\rangle, \quad \text{or} \quad |\uparrow\uparrow\rangle, \ |\uparrow\downarrow\rangle, \ |\downarrow\uparrow\rangle, \ |\downarrow\downarrow\rangle$$

where $|+-\rangle$ stands for $m_1 = \pm\frac{1}{2}$.

2) The $\{s, m\}$ representation (or the triplet-singlet representation) based on the eigenkets of S^2 and S_z. where $S = 1$ ($S = 0$) is referred to as spin triplet. $S = 0$ is singlet.

$|s = 1, m = 1\rangle = |\uparrow\uparrow\rangle$ tell us that we have both electrons with spin up. This situation can correspond only to $s = 1$, $m = 1$ and apply ladder operator to both side of below equation.

$$S_- \equiv S_{1-} + S_{2-}, \tag{4.25}$$

and

$$S_-|s = 1, m = 1\rangle = (S_{1-} + S_{2-})|\uparrow\uparrow\rangle \tag{4.26}$$

In doing so, we must remember that operators like S_{1-} affects just the first spin-1/2 and

S_{2-} affects just the second spin-1/2 of particles $|\uparrow\uparrow\rangle$ and so on. using the $C^{\pm}_{jm}$ coefficients of ladder operators and $S_+|-\rangle = \hbar|+\rangle$, $S_-|+\rangle = \hbar|-\rangle$ and acting $S_+|+\rangle = 0$, $S_-|-\rangle = 0$ and so on.

$$S_\pm|s,m\rangle = \sqrt{s(s+1) - m(m\pm 1)}\hbar|s,m\pm 1\rangle. \tag{4.27}$$

The N-qubit system can be described using a wavefunction for N-spin-1/2 moments, which are expressed in terms of total angularmomentum states $|S_{tot}, m_{tot}\rangle$. The total spin operators are determined by the sum of the individual qubit operators.

$$\hat{S}_Z = \sum_{l=0}^{N} \sigma_z^l, \quad S^v_{tot} = S^v_1 + \cdots + S^v_N, \quad \text{with} \quad v = x, y, z. \tag{4.28}$$

The ladder operators have the greatest effect on states with m close to zero and coefficients $\sim S$, and the least effect on states that are almost fully polarized and have coefficients $\sim \sqrt{S}$. Therefore, bigger spins—or, in the case of an ensemble, more spins—have a more noticeable effect.

In Chapter 2, we delved into topics such as the second quantized number operator $\hat{n} = \hat{a}^\dagger\hat{a}$, the qubit representation of photons, and in this chapter add the spin quantization. The primary focus of this thesis is to generate W states and Bell states within the spin system. To understand the generation of W states within the cavity setup, it is crucial to grasp the interaction between atoms and photons in a two-level system. This interaction occurs within the context of Dicke model in the cavity quantum electrodynamics (QED) setups.

4.6 Dicke model

In the field of quantum optics [44,117,129], the examination of N two-level atoms (qubits) interacting with an oscillator holds significant importance. Excitation of the atoms occurs when the frequency of the oscillator is resonant with the energy difference between the

two atomic energy levels. The subsequent transition of the excited state to the ground state leads to the spontaneous emission of light [116]. When atoms (or molecules) are in proximity, the collective emission of photons is naturally accelerated and more intense compared to the emission from isolated atoms. The direction of emission is distinct and depends on the geometry of the sample [19].

The emission of light in each direction is random, resulting in the incoherent cyclic process of radiation emission. In this context, the radiation field's intensity, represented by I, is observed to be proportional to N, demonstrating a linear relationship between them. However, Dicke introduced the concept of coherent radiation emission when the frequency of the oscillator significantly exceeds the qubit frequency [30]. This condition leads to the collective interaction of the ensemble of atoms with the incident radiation field. The atoms jointly undergo de-excitation to the ground states, resulting in the coherent emission of more powerful radiation, recognized as superradiance.

Within the rotating wave approximation [**?**, 137], this system is described by the Dicke Hamiltonian,

$$H = \lambda \hat{S}^{z}_{tot} + \omega_c a^{\dagger} a + g\{\hat{S}^{-}_{tot} a^{\dagger} + \hat{S}^{+}_{tot} a\}, \tag{4.29}$$

where a ($a^{\dagger}$) represents photon annihilation (creation), ω_c is a cavity mode and $\hat{S}_{tot}$ collective spin operator as shown in Eqn. (4.28).

For a qualitative grasp of the phenomenon of superradiance, envisioning N atoms collectively emitting radiation in phase is crucial. This cooperative emission results in superradiance, where the coherent emissions reveal a dependence of I on the number of atoms as N^2. Consequently, the emission rate is amplified by a factor of N in superradiance, a characteristic not observed in the typical incoherent spontaneous emission of radiation.

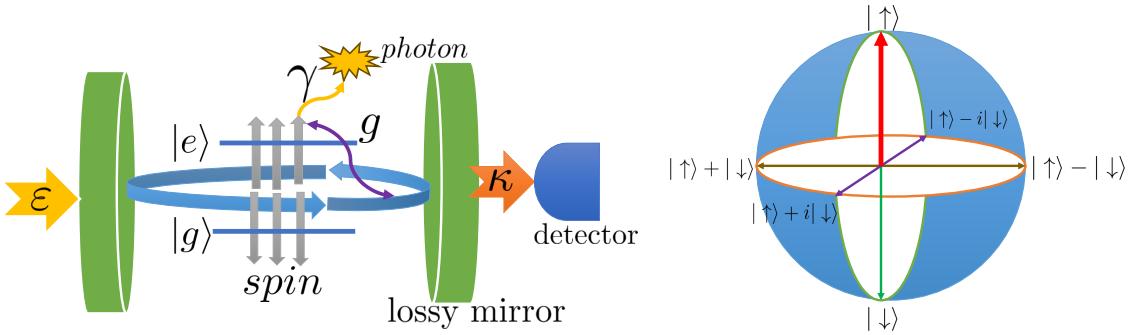

Figure 4.7: Cavity QED setup and Spin representation of Bloch sphere

4.7 Two Spin-1/2 particles

For the two qubit system containing one atom in the excited state $|\uparrow\rangle$ and the other in the ground state $|\downarrow\rangle$, the initial state is taken to be $|\downarrow\uparrow\rangle$ as shown in Fig. 4.7. Consider a pair of electron 1 and 0.The total spin of pair of electron is 1 and 0. The three states of total spin 1 is called triplet, the state of spin 0 is called singlet.

$$S_Z = S_{1z} + S_{2z} = \frac{1}{2} \pm \frac{1}{2} = 1, 0. \tag{4.30}$$

Now $|s = 1, m = -1, 0, +1\rangle \rightarrow$ three states are triplet $|t_{-1,0,+1}\rangle$:

$$\begin{aligned} |t_1\rangle &= |s = 1, m = 1\rangle = |\uparrow\uparrow\rangle \\ |t_0\rangle &= |s = 1, m = 0\rangle = \frac{[|\uparrow\downarrow\rangle + |\downarrow\uparrow\rangle]}{\sqrt{2}} \\ |t_{-1}\rangle &= |s = 1, m = -1\rangle = |\downarrow\downarrow\rangle, \end{aligned} \tag{4.31}$$

and $|s = 0, m = 0\rangle \rightarrow |S_0\rangle$ one states is singlet:

$$|s_0\rangle = |s = 1, m = 0\rangle = \frac{[|\uparrow\downarrow\rangle - |\downarrow\uparrow\rangle]}{\sqrt{2}}. \tag{4.32}$$

Normally four states are available but in our aims to generate the Bell state and W

state since $m_z = 0$, we can write initial state as superposition of two states,

$$|\Psi_I\rangle = |\downarrow\uparrow\rangle = \alpha_1|s = 1, m_z = 0\rangle + \alpha_2|s = 0, m_z = 0\rangle \tag{4.33}$$

It is prepared in such a way that atoms have non overlapping spatial wave functions. This initial state is in the superposition of the singlet state $|s_0\rangle$ and triplet state $|t_0\rangle$. It is then allowed to interact with the radiation field where the triplet part participates in the radiation process and jumps to the lower energy triplet state. The singlet state does not couple with the triplet states during the process. It is observed that after a long period of time there is still a probability of one-half that a photon has not been emitted. When there is no emission of photons even after a sufficient period of time two atoms resides in a singlet state and it is impossible to say which atom is in the excited one.

Suppose if we consider the initial state as the triplet state $|t_0\rangle$, a state with single excited atom and the transition probability of this state upon emission of radiation would be double that for a lone excited atom. Thus the presence of the unexcited atom in this case doubles the radiation rate. In the event that a photon is detected, this measurement will cause the spinwave function to collapse into the $|t_1\rangle$ state. On the other hand, when photon emission is not observed, the system collapses into a singlet state $|s_0\rangle$, leaving both spins entangled. Eq. (4.15) indicates that the singlet and triplet states are Bell states.

4.7.1 Three Spin-1/2 particles

Initially three spin-1/2 particles are

$$S = S_1 + S_2 + S_3 = |\downarrow\downarrow\uparrow\rangle, \quad S = \frac{3}{2}, \frac{1}{2}, \frac{1}{2};\ m_z = -\frac{1}{2}. \tag{4.34}$$

Given that $m_z = -1/2$ out of the eight states, only three states are accessible. We can represent the initial states as a superposition of these three states for a system of three

spin-1/2 particles.

$$|\Psi_1\rangle = |\downarrow\downarrow\uparrow\rangle = \alpha_1|\frac{3}{2}, -\frac{1}{2}\rangle + \alpha_2|\frac{1}{2}, -\frac{1}{2}, A\rangle + \alpha_3|\frac{1}{2}, -\frac{1}{2}, B\rangle. \tag{4.35}$$

Starting $|\frac{3}{2}, -\frac{3}{2}\rangle = |\downarrow\downarrow\downarrow\rangle$, with the given state we aim to identify another state using ladder operators. These two states are both normalized and orthogonalized. Applying ladder operators will allow us to find additional states. The lowering operator is connected to the concept of "collective emission" of a photon, wherein a single atom undergoes a transition from the excited to the ground state by emitting a photon. However, the specific atom responsible for the emission remains uncertain.

Now, consider three atoms situated in close proximity (though not close enough to directly interact with each other), all initially in the ground state collectively absorb a photon.

$$|s = 3/2, m_z = -3/2\rangle = |\downarrow\downarrow\downarrow\rangle. \tag{4.36}$$

When a photon is absorbed collectively, the atoms transition to the subsequent state.

$$|s = 3/2, m_z = 3/2\rangle = |\uparrow\uparrow\uparrow\rangle. \tag{4.37}$$

The state $|\frac{3}{2}, -\frac{1}{2}\rangle$ undergoes photon emission, while the states $|\frac{1}{2}, -\frac{1}{2}, A\rangle$ and $|\frac{1}{2}, -\frac{1}{2}, B\rangle$ do not emit photons. However, the two not emitted photon states can absorb photons through interaction with the cavity mode. This is because the reduction of m_z values is not possible, defining them as dark states. This distinction highlights the difference between a singlet state and a dark state.

In scenarios where the atoms are not freely floating in space but instead interacting with their surroundings, the state would rapidly decohere, and the uncertainty would be resolved. If one of the atoms absorbs the photon, the uncertainty arises regarding which specific atom is involved. In such cases, a single atom, chosen randomly, would be identi-

fied as the one that absorbed the photon, aligning with everyday intuitive expectations. However, for the current discussion, we assume the absence of decoherence. In this context, it is implied that the distance between the atoms is significantly smaller than a wavelength; otherwise, the expression would be modified.

$$|s = 3/2, m_z = 1/2\rangle = \frac{1}{\sqrt{3}}\Big[\exp^{ik.r_1}|\downarrow\uparrow\uparrow\rangle + \exp^{ik.r_2}|\uparrow\downarrow\uparrow\rangle + \exp^{ik.r_3}|\uparrow\uparrow\downarrow\rangle\Big] \tag{4.38}$$

where k is the wavevector of that absorbed photon and r_1,r_2, and r_3 are the atom positions. It represents a generalized W state. Let's assume that the atoms are either extremely close together (much smaller than a wavelength) or precisely spaced at one wavelength intervals, allowing us to disregard the influence of exponential factors for simplicity.

Under the Dicke condition, this process leads to the formation of the W state with equal amplitude and phase.

$$|s = 3/2, m_z = -1/2\rangle = \frac{1}{\sqrt{3}}\Big[|\downarrow\downarrow\uparrow\rangle + |\downarrow\uparrow\downarrow\rangle + |\uparrow\downarrow\downarrow\rangle\Big], \tag{4.39}$$

when $N = 3$, this state represents the three spin W state that resembles the Eq. (4.19).

Dicke's original thought experiment was recently reproduced in a lab setting with two superconducting qubits inside a microwave cavity [12, 95] . They showed that the spins together create a mixed state with both dark and bright components by measuring the density matrix of the released photon. The following succinctly sums up their findings: Interaction with a shared photon field causes two spins that would otherwise be isolated to become entangled. An innovative method for creating entangled quantum states in a lab is presented in this experiment. Increasing the number of spins in parallel to create highly entangled states with superradiance and subradiance (Dark state) is an extension of this experiment. From a technological standpoint, it is more advantageous to store information in the subradiant state and share information in the superradiant state.

4.8 Many-body Entangled state

We first take the simplest non-trivial initial state [37,137], $|\uparrow\downarrow\downarrow\cdots\downarrow\rangle$. This can have only two S_{tot} components:

$$|\Psi_{initial}\rangle = |\uparrow\downarrow\cdots\downarrow\rangle = \alpha_{S=N/2}|\psi_{N/2}\rangle + \alpha_{S=N/2-1}|\psi_{N/2-1}\rangle, \tag{4.40}$$

where $|\psi_{N/2}\rangle \sim \hat{\mathcal{P}}_{S=N/2}|\uparrow\downarrow\cdots\downarrow\rangle$ and $|\psi_{N/2-1}\rangle \sim \hat{\mathcal{P}}_{S=N/2-1}|\uparrow\downarrow\cdots\downarrow\rangle$.

Different numbers of photons will be emitted by each component of this state, which is indexed by S_{tot} [45,46]. Perform a Stern-Gerlach-type measurement, which collapses the wavefunction, by counting the number of photons emitted. Specifically, the wavefunction collapses onto the W state observation.

$$|\Psi_{W-state}\rangle \sim \hat{P}_{S=N/2}|\Psi_{initial}\rangle. \tag{4.41}$$

This is because any permutation of spins in the projection operator itself results in symmetry. This is evident in construction,

$$\hat{P}_{S=\Sigma} = \prod_{S'\neq\Sigma} \frac{\hat{S}_{tot}^2 - S'(S'+1)}{\Sigma(\Sigma+1) - S'(S'+1)}. \tag{4.42}$$

It is symmetric under any permutation of the constituent spins because it only contains $\hat{S}_{tot}$.

We use $\hat{\mathcal{P}}_{S=\Sigma}$ to denote the projector onto states with total spin $S_{tot} = \Sigma$. In analogy with the two-spin problem, $|\psi_{N/2}\rangle$ is a bright state which will emit a photon and decay to $|S_{tot} = N/2, m_{tot} = -N/2\rangle$. On the other hand, $|\psi_{N/2-1}\rangle$ is a dark state as it cannot reduce its m_{tot} quantum number further.

The generalized W-state as

$$|\psi_{W-state}\rangle = \frac{1}{\sqrt{N}} \sum_{k=1}^{N} e^{i\phi_k} | \downarrow_1 \ldots \downarrow_{k-1} \uparrow_k \downarrow_{k+1} \ldots \downarrow_N \rangle. \tag{4.43}$$

Every component within the system shares the same probability amplitude, although the phases ϕ_k may not necessarily be identical. If all ϕ_k values are equal, this configuration corresponds to the familiar W state [34]. However, it's important to note that there are no constraints imposed on the values of ϕ_k in this context. In fact, as we will explore later, the ϕ_k values cannot be independently adjusted in many situations.

In the context of the Dicke condition, the projection of the initial state, representing the equal amplitude and phase $\psi_{N/2}$ state, can be expressed as follows:

$$|\Psi_{W-state}\rangle = \frac{1}{\sqrt{N}} \left(|\uparrow\downarrow\downarrow \cdots \downarrow\rangle + |\downarrow\uparrow\downarrow \cdots \downarrow\rangle + \cdots + |\downarrow\downarrow \ldots \downarrow\uparrow\rangle \right). \tag{4.44}$$

This $|\Psi_{W-state}\rangle$ represents the W maximally many-body entangled state.

Chapter 5

Spreading entanglement through pairwise exchange interactions

This chapter includes content from the following journals: (**Theerthagiri, L**., Ganesh, R. Spreading entanglement through pairwise exchange interactions. Quantum Inf Process 22, 355 (2023). https://doi.org/10.1007/s11128-023-04104-z)

5.1 Introduction

The synthesis of entangled states is an enduring problem in quantum science.This Thi requires systematic protocols for transforming a direct-product state into certain superpositions. To mitigate decoherence effects, any such process must be optimized to minimize operation time. This has inspired several studies on time-optimized protocols [13, 17, 18, 27, 49, 136, 141]. At the same time, it is important to ensure scalability. As quantum devices grow in qubit-number, entangling protocols must be able to operate within reasonable timeframes. This requires optimization with respect to qubit-number-complexity (operating time vs. number of qubits). Motivated by these ideas, we consider the simplest entanglement-spreading task – that of spreading a single excitation equally

among N participating qubits. We impose a constraint informed by the design of multiple quantum architectures: this task is to be achieved solely by pairwise exchange interactions. We present three solutions and discuss their scaling with qubit number.

The interest in entanglement spreading can be gauged from the large number of studies on the W state – a prototypical entangled state where an excitation is equally spread over N qubits [34] as explained in chapter 4. Many proposals have been put forward to synthesize the W-state [11, 101] and many experiments have succeeded in creating it [52,55,68,97] . The challenge in these protocols can be stated as follows: starting from an unentangled initial state with only one qubit excited, how can the excitation be spread equally among all qubits? In this article, we take an approach that is inspired by *mancala* games – a family of games with a long history and wide geographical spread [109]. They are played on a board with pits that contain pieces. In a typical game, a player picks pieces from one pit and distributes them over the other pits. Here, we have N qubits that are analogous to N pits. An excitation (an $\uparrow$ state or a 1-state) is initially stored in one qubit, analogous to pieces stored in a pit. The goal of the game is to spread the pieces evenly among N pits. Below, we describe three protocols to achieve this goal and characterize their scaling with N.

We assume an architecture where qubits can undergo pairwise exchange interactions. Exchange interactions have been proposed as a mechanism for designing logic gates [85] and it is explained in chapter 4. They can be achieved in many settings. For example, with ultracold atoms in an optical lattice, a lattice-modulation can be used to induce an XXZ-exchange interaction [5]. The time period and the strength of the interaction can both be controlled by tuning the modulation. In semiconductor qubits, exchange interactions can be induced in a similar fashion by tuning tunnelling barriers [71, 91, 102]. Alternatively, they can be mediated by a cavity-mode [142] explained in chapter 4, where the strength and duration can be controlled by varying the detuning.

5.2 Entanglement by exchange

To set the stage, we begin by considering two two-level atoms (qubits), labelled A and B. They undergo an exchange interaction which entangles them. The degree of entanglement can be tuned by varying the interaction time, t.

We first discuss Heisenberg exchange as it leads to a simple form for the time-evolution operator. We then generalize to anisotropic exchange of the XXZ type. The results discussed in subsequent sections hold for the any value of the XXZ anisotropy, including the Heisenberg limit. A Heisenberg exchange interaction between two qubits is described by the Hamiltonian $\hat{H}_{AB} = J\left[\sigma_x^A\sigma_x^B + \sigma_y^A\sigma_y^B + \sigma_z^A\sigma_z^B\right]$, where σ's are single-qubit operators encoded by Pauli matrices. With the two qubits interacting for time t, the wavefunction undergoes unitary evolution. The time-evolution operator can be written in various forms. For our purposes, it is best written as

$$\hat{U}_{AB}(t) = e^{it/2}\Big\{\cos(t)\ \hat{\mathbb{1}}_{AB} - i\sin(t)\ \hat{\Pi}_{AB}\Big\}, \tag{5.1}$$

where time t is measured in units of $2\hbar/J$. The identity operator, $\hat{\mathbb{1}}_{AB}$, leaves both qubits unchanged. In contrast, $\hat{\Pi}_{AB}$ is the permutation operator that switches the states of A and B. In the S_z basis ($\{\uparrow\uparrow, \uparrow\downarrow, \downarrow\uparrow, \downarrow\downarrow\}$), it is given by

$$\hat{\Pi}_{AB} = \begin{pmatrix} 1 & 0 & 0 & 0 \\ 0 & 0 & 1 & 0 \\ 0 & 1 & 0 & 0 \\ 0 & 0 & 0 & 1 \end{pmatrix} \tag{5.2}$$

If one qubit is initially excited and the other is in the ground state, the permutation

operator transfers the excitation from the former to the latter. As seen from Eq. 5.1, the amplitude for excitation transfer is $\sin(t)$, while that for retaining the excitation at the same qubit is $\cos(t)$. By tuning the interaction time t, the 'transferred weight' can be tuned. For a generic value of t, the final state is entangled with the excitation spread over two qubits.

We next consider a more general interaction Hamiltonian of the XXZ form,

$$\hat{H}^{\lambda}_{AB} = J\Big[\sigma^A_x\sigma^B_x + \sigma^A_y\sigma^B_y + \lambda\sigma^A_z\sigma^B_z\Big], \tag{5.3}$$

where λ is an anisotropy parameter. This Hamiltonian leads to the unitary time-evolution operator,

$$\hat{U}^{\lambda}_{AB}(t) = e^{-i\lambda t/2}\hat{P}_{\sigma_A\neq\sigma_B}\Big\{\cos(t)\;\hat{\mathbb{1}}_{AB} - i\sin(t)\;\hat{\Pi}_{AB}\Big\} + e^{i\lambda t/2}\hat{P}_{\sigma_A=\sigma_B}, \tag{5.4}$$

Here, $\hat{P}_{\sigma_A=\sigma_B}$ is a projection operator onto the $\sigma_A = \sigma_B$ sector, where both qubits are in the same state. In this case, $\hat{U}^{\lambda}_{AB}(t)$ leaves the state unchanged (up to a global phase). In contrast, $\hat{P}_{\sigma_A\neq\sigma_B}$ selects states where the qubits are in opposite states. Acting on such states, $\hat{U}^{\lambda}_{AB}(t)$ exchanges their states with probability amplitude $\sin(t)$. If the initial state had one qubit excited and one in the ground state, the final state will generically be entangled. The interaction time, t, controls the spread of the excitation across the two qubits.

Before stating the problem of interest, we note that the amplitudes in Eqs. 5.1 and 5.4 are periodic in time with period 2π. In the following discussion, we always choose the shortest time that can effect a desired operation.

5.3 Problem statement

In chapter 4, we explained the N two-level atoms (qubits) in the cavity QED setup. We consider N two-level atoms and we assume a setup where pairs of atoms can be selected and made to interact for a specified period of time. For instance, this may involve bringing two atoms close to one another—at a certain fixed distance and for a chosen time interval. Initially, the N qubits are in a direct-product state represented as

$$\psi_{initial} = |\uparrow_1\downarrow_2\downarrow_3 \ldots \downarrow_N\rangle. \tag{5.5}$$

The first qubit is in the excited state, while the others are in the ground state. This can be viewed as one quantum of information stored in qubit-1.

The target state is a generalized W-state as seen in chapter 4 given by

$$\psi_{target} = \frac{1}{\sqrt{N}} \sum_{j=1}^{N} e^{i\phi_j} |\downarrow_1 \ldots \downarrow_{j-1}\uparrow_j\downarrow_{j+1} \ldots \downarrow_N\rangle. \tag{5.6}$$

This is a sum of N components, each having the excitation positioned at a different qubit. Each component has the same probability amplitude, but not necessarily the same phase. If all ϕ_j's are equal, this would be the well-known W state [34]. We do not place any restriction on ϕ_j's here. In fact, we will see below that ϕ_j's cannot be independently tuned.

In the following sections, we propose three protocols that take the initial state of Eq. 5.5 to the target state of Eq. 5.6. Our arguments hold for interactions of the XXZ type with any value for the anisotropy parameter, λ.

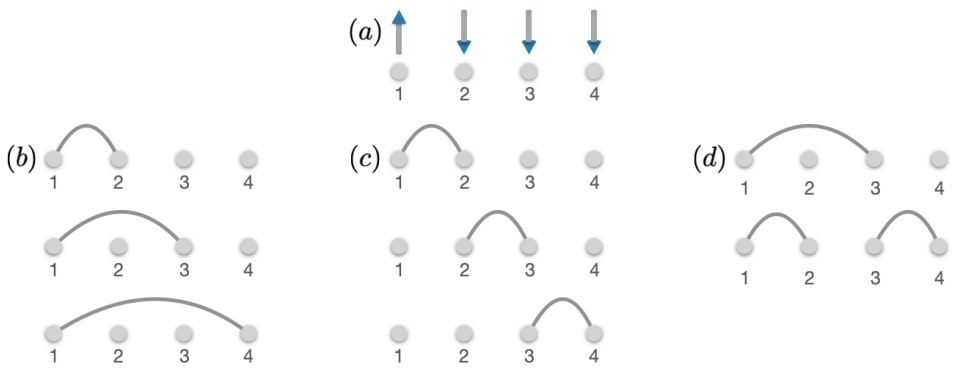

Figure 5.1: Three protocols illustrated for a system with $N = 4$ qubits. (a) The initial direct product state with one qubit excited and $N - 1$ qubits in the ground state. (b) A flying-qubit protocol where qubit-1 interacts with each of the other qubits in order. (c) A sequential protocol where pairs of neighbouring qubits interact in succession. (d) A divide-and-conquer protocol where the system is arranged hierarchically in units of two qubits. At each stage, interactions act at one level of the hierarchy.

5.4 Protocol with a single flying qubit

We assume that one of the qubits can move freely and interact with each of the others. The qubit could be a photon or a vibration mode that can selectively couple to static qubits. In fact, the protocol discussed below was successfully used to generate a generalized W state with trapped ions in 2005 [55]. In this study, the role of the flying qubit was played by a vibration mode of a trapped-ion-chain. In the following discussion, we assume that this flying qubit is labelled as $j = 1$. We further assume that this qubit is initially in the excited state while all other qubits ($j = 2, 3, \ldots, N$) are in the ground state.

We propose a protocol where qubit-pairs interact in the following order: qubits 1 and 2 interact for time $t_{1,2}$, qubits 1 and 3 interact for time $t_{1,3}$, ..., qubits 1 and N interact for time $t_{1,N}$. Initially, qubits 1 and 2 begin in the state $|\uparrow_1\downarrow_2\rangle$. As they interact for time $t_{1,2}$, their state is acted upon by the time-evolution operator of Eq. 5.1 or 5.4. The resulting state is (up to a global phase)

$$\cos(t_{1,2})|\uparrow_1\downarrow_2\downarrow_3 \ldots \downarrow_N\rangle - i\sin(t_{1,2})|\downarrow_1\uparrow_2\downarrow_3 \ldots \downarrow_N\rangle.$$

After time $t_{1,2}$, qubit 2 does not interact with any of the other qubits. The component that is proportional to $\sin(t_{1,2})$ remains unchanged in amplitude, although it may accrue a phase. Therefore, in the final state, the probability amplitude for qubit 2 to be excited is $\sin(t_{1,2})$. Upon comparing with the target state of Eq. 5.6, we must have

$$\sin(t_{1,2}) = \frac{1}{\sqrt{N}}. \tag{5.7}$$

This fixes $t_{1,2}$. Subsequently, qubit 1 interacts with qubit 3 for time $t_{1,3}$. At the start of this process, the amplitude for qubit 1 to be excited is $\cos(t_{1,2}) = \sqrt{\frac{N-1}{N}}$. The probability amplitude for the excitation to be transferred to qubit 3 is given by a product of two amplitudes: (i) that for qubit 1 to be initially excited and (ii) that for the excitation to be transferred during the interaction. This is given by

$$\sqrt{\frac{N-1}{N}} \times \sin(t_{1,3}) = \frac{1}{\sqrt{N}}. \tag{5.8}$$

We have set the amplitude to $1/\sqrt{N}$ in order to match the target state of Eq. 5.6. As qubit 3 does not interact after this step, it will always retain its amplitude through to the end. We obtain

$$\sin(t_{1,3}) = \frac{1}{\sqrt{N-1}}. \tag{5.9}$$

At this point, the amplitude for qubit-1 to be excited is

$$\sqrt{\frac{N-1}{N}} \times \cos(t_{1,3}) = \sqrt{\frac{N-1}{N}} \times \sqrt{\frac{N-2}{N-1}} = \sqrt{\frac{N-2}{N}}. \tag{5.10}$$

At the next step, qubits 1 and 4 interact. The amplitude for an excitation to be transferred to qubit 4 is given by

$$\sqrt{\frac{N-2}{N}} \times \sin(t_{1,4}) = \frac{1}{\sqrt{N}}. \tag{5.11}$$

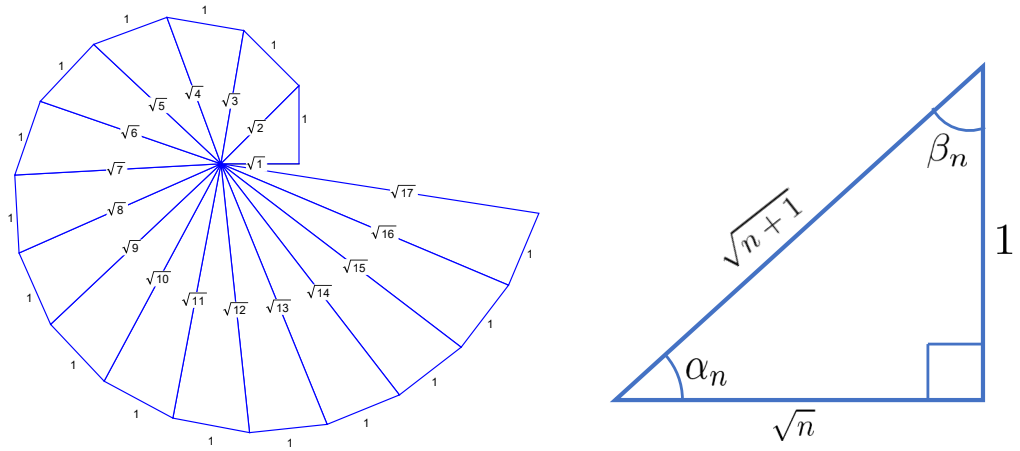

Figure 5.2: Top: The spiral of Theodorus, constructed as a sequence of right-angled triangles. Bottom: The n^{th} triangle in the spiral, with sides 1, $\sqrt{n}$ and $\sqrt{n+1}$.

This fixes $\sin(t_{1,4}) = \frac{1}{\sqrt{N-2}}$. Proceeding in this manner, we find

$$\sin(t_{1,5}) = \frac{1}{\sqrt{N-3}}, \quad \ldots, \quad \sin(t_{1,N}) = \frac{1}{\sqrt{2}}. \tag{5.12}$$

These relations can be gather into a general expression for the j^{th} time interval,

$$t_{1,j+1} = \sin^{-1}\{1/\sqrt{N-j+1}\}. \tag{5.13}$$

Remarkably, these time periods have an elegant geometric interpretation. These are angles within the spiral of Theodorus, a geometric construction known since the 5th century BCE [26, 53]. The spiral is constructed as a series of right-angled triangles. At each step, a unit line segment is drawn perpendicular to the hypotenuse of the previous step. This forms a new right-angled triangle with a longer hypotenuse. This procedure leads to a sequence of points spiralling outwards. The n$^{\text{th}}$ point is given as (r_n, θ_n) in polar coordinates. Here, $r_n = \sqrt{n}$ and θ_n is a monotonically increasing function of n. For large n, it is known [26, 62] that $\theta_n \sim 2\sqrt{n}$, with corrections that are subleading in powers of n.

Fig. 5.2 shows the angles as they appear in the spiral. The 'interior angles', denoted

as α_n's, are precisely the time intervals given in Eq. 5.13,

$$\alpha_1 = t_{1,N}; \;\; \alpha_2 = t_{1,N-1}; \;\; \ldots; \;\; \alpha_{N-1} = t_{1,2}. \tag{5.14}$$

From the figure, it is clear that the interior angles decrease progressively, i.e., α_n monotonically decreases with n. We deduce that the time intervals increase progressively, with $t_{1,2} < t_{1,3} < \ldots < t_{1,N}$. The total process time, excluding overheads such as rearranging qubits, is given by

$$t_{flying} = t_{1,2} + t_{1,3} + \ldots + t_{1,N} = \sum_{j=1}^{N-1} \alpha_j = \theta_N \approx 2\sqrt{N}. \tag{5.15}$$

where α_j's are angles as shown in Fig. 5.2. The sum over α_j's yields θ_N, the angular coordinate of the N^{th} point of the Theodorus spiral. In the last step, we have used the approximate form for θ_N when N is large. We arrive at the following result: this protocol yields a generalized W-state with the operation time scaling as $\sqrt{N}$ for large N. This time scale applies to the setup discussed in Chapter 4.

5.5 Protocol with sequential pairwise interactions

We next consider a protocol where qubit-pairs interact in the following order: qubits 1 and 2 interact for time $t_{1,2}$, qubits 2 and 3 interact for time $t_{2,3}$, ..., qubits $N-1$ and N interact for time $t_{N-1,N}$. Initially, qubit 1 is taken to be excited while all others are in the ground state. As qubits 1 and 2 interact, their state is acted upon by the time-evolution operator of Eq. 5.1 or Eq. 5.4. A portion of the excitation can be transferred from qubit 1 to 2. At the next step, a portion of the excitation in qubit 2 is transferred to 3 and so on.

Qubit 1 is only modified during the first step. As a result, its final excitation-amplitude is determined at the first step alone. From Eq. 5.1 or 5.4, this is given by $\cos(t_{1,2})$ – the

amplitude for no excitation transfer occurring during the first step. In the final target state, the amplitude for qubit-1 to be excited must be $1/\sqrt{N}$, so that

$$\cos(t_{1,2}) = \frac{1}{\sqrt{N}}. \tag{5.16}$$

This fixes time $t_{1,2}$. After the first step, the amplitude for qubit-2 to be excited is given by $\sin(t_{1,2}) = \sqrt{\frac{N-1}{N}}$. During the second step, this excitation may be passed onto qubit-3. Beyond the second step, qubit-2 remains unchanged. As a result, the final amplitude for qubit-2 to be excited is given by $\sin(t_{1,2}) \times \cos(t_{2,3})$. In the final target state, the amplitude for qubit-2 to be excited must be $1/\sqrt{N}$, so that

$$\sqrt{\frac{N-1}{N}}\cos(t_{2,3}) = \frac{1}{\sqrt{N}} \implies \cos(t_{2,3}) = \frac{1}{\sqrt{N-1}}. \tag{5.17}$$

This fixes $t_{2,3}$. Considering each following step in the same fashion, we arrive at

$$\cos(t_{3,4}) = \frac{1}{\sqrt{N-2}}, \quad \ldots, \quad \cos(t_{N-1,N}) = \frac{1}{\sqrt{2}}. \tag{5.18}$$

These relations determine all time intervals in the problem, with $t_{j,j+1} = \cos^{-1}(1/\sqrt{N-j+1})$. These times are, once again, angles that appear in the spiral of Theodorus. As shown in Fig. 5.2, they are 'exterior angles' denoted as β_n's. We have $\beta_1 = t_{N-1,N}, \beta_2 = t_{N-2,N-1}, \ldots,$ $\beta_{N-1} = t_{1,2}$.

From Fig. 5.2, we see that β's increase monotonically with n. We conclude that the time intervals in this protocol are arranged in descending order: $t_{1,2} > t_{2,3} > \ldots > t_{N-1,N}$.

As seen from Fig. 5.2, β_j and α_j form a pair of complementary angles for any j. In Sec. 5.4, the total operation time was written as a sum over α-angles. Here, the total

operating time is

$$t_{sequential} = t_{1,2} + t_{2,3} + \ldots + t_{N-1,N} = \sum_{j=1}^{N-1} \beta_j$$
$$= (N-1)\frac{\pi}{2} - \sum_{j=1}^{N-1} \alpha_j \approx (N-1)\frac{\pi}{2} - 2\sqrt{N}.$$

We have used the result quoted in Eq. 5.15 for the sum over α_j. We conclude that the total operating time scales linearly with N in this protocol. This time scale applies to the configuration described in Chapter 4.

5.6 Divide-and-conquer protocol

The previous two sections present two protocols. In both, an initial excitation in one qubit is spread over N qubits in serial fashion – through a sequence of exchange interactions that must be executed in serial order. We now consider a third protocol that allows for parallel operations. At each step, we consider two qubits. One has a certain probability of being in the excited state, while the other is entirely in the ground state. An exchange interaction is carried out to equally spread the excitation-amplitude between the two qubits.

This protocol is particularly suited for N's that are powers of 2, i.e., $N = 2^M$ where M is an integer. The protocol proceeds through M stages where each stage may involve multiple pairwise interactions. For illustration, we take the example of 4 qubits ($M = 2$). Initially, qubit-1 is excited while all others are in the ground state. During the first stage, qubit-1 and qubit-3 are made to interact. The interaction time is chosen such that the qubit-1 and 3 both acquire the same excitation-amplitude. That is, $\cos(t_{1,3}) = \sin(t_{1,3}) = 1/\sqrt{2}$.

During the second stage, qubit-1 interacts with qubit-2 while qubit-3 interacts with qubit-4. These two interactions may take place at the same time, in parallel. For each

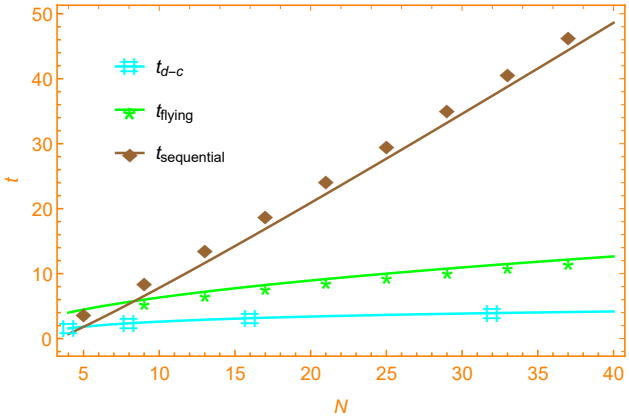

Figure 5.3: The total interaction time t vs. the number of qubits, N for the three protocols discussed here. The lines show the approximate scaling form for large N.

interaction, the time period is fixed such that the likelihood of excitation-transfer is equal to that of excitation-retention, i.e., $\cos(t_{1,2}) = \sin(t_{1,2}) = \cos(t_{3,4}) = \sin(t_{3,4}) = 1/\sqrt{2}$. This yields the target state, with each qubit having the same amplitude $(1/2)$ for carrying an excitation.

For any larger value of M, we have M stages. It can be easily seen that the total number of pairwise interactions is still $N-1$, the same as for the previous two protocols. However, all interactions within a stage may take place in parallel. Each of these interactions takes place over a time period given by $\cos(t) = 1/\sqrt{2}$, i.e., $t = \pi/4$.

If the setup is such that only one pairwise interaction can take place at a time, the total operating time would be $(N-1)\pi/4$, scaling linearly with N. If parallel pairwise interactions are possible, they significantly reduce operating time. We have M distinct stages in the problem, each involving pairwise interactions over a time period of $\pi/4$. The lowest time is achieved if all interactions of a stage are performed simultaneously. This yields a lower bound for the operating time, $t_{lower\ bound} = M\pi/4$. This quantity scales as $M \sim \ln_2 N$. For the setup covered in Chapter 4, this timeline is relevant.

5.7 Phase differences in the target state

The target state, as defined in Eq. 5.6, has N phases denoted as ϕ_j's. These phases cannot be independently controlled. With the Heisenberg exchange of Eq. 5.1, every action of the permutation operator carries a phase of $3\pi/2$ (a factor of $-i$). With an XXZ interaction, we get additional phases as seen from Eq. 5.4. As a result, in any of the three protocols, the final state corresponds to Eq. 5.6 with disparate values of ϕ_j's. To illustrate this, we formally show that a W state (with all ϕ_j's being equal) cannot be synthesized using pairwise exchange interactions.

Our argument is based on two observations: (i) pairwise interactions, as described by the operator in Eq. 5.1 are unitary and therefore, reversible. (ii) The W state is invariant under any permutation. As a result, it is unchanged (up to a global phase) by operators of the form Eq. 5.1 or Eq. 5.4. Suppose the W state could be synthesized starting from a direct product state via pairwise interactions. It must be possible to reverse the process – to start from a W state and to arrive at a direct product state with only pairwise interactions. However, this is not possible, as any operation of the form of Eqs. 5.1 or 5.4 does not change the W state. We conclude that the W state cannot be produced within this approach.

Chapter 6

Conclusion

The developments in quantum mechanics, especially with regard to non-classical phenomena, have had a revolutionary effect on a number of contemporary technologies, such as computation, communication, metrology, and sensing. The idea behind quantum illumination (QI) is to use the existence of quantum correlations in a system to enhance its performance and make them a useful tool for obtaining a quantum advantage. This idea is used in "quantum target detection," a subset of problems related to quantum sensing.

Throughout this dissertation, we have methodically investigated a number of significant open problems and limitations related to quantum illumination (QI). We started Chapter 1 by going over the Gaussian QI that Tan et al. had proposed, but recasting it in terms of symmetric and asymmetric Quantum Hypothesis Testing (QHT) and adding arbitrary quantum correlations. According to this analysis, maximal entanglement is not strictly necessary to achieve a quantum advantage. Additionally, the study provided a concrete interpretation of parameters by drawing parallels between quantum and classical radar theories. This analogy showed that, akin to QI, the target range affects the effective limit of entanglement-based quantum target detection, particularly when taking into account the feasibility of carrying out experiments to produce a significant number of entangled states in a practical amount of time.

Continuing the exploration of practical considerations in experimental settings, Chapter 1 delves into the implications of a conventional microwave Quantum Illumination (QI) technique. The concept involves using the stored half of an entangled photon pair for dual-balanced difference detection following the phase conjugation of the reflected light. In scenarios where $N_s \ll 1$, $\kappa \ll 1$, and $N_B \gg 1$, this method provides an identical 3 dB error exponent gain in error probability. Additionally, it demonstrates superior performance compared to the Optical Parametric Amplification (OPA) receiver.

Chapter.2 focused on examining the mathematical foundations essential for the quantum illumination (QI) setup. The target detection in QI involves employing hypothesis testing and continuous variable theory. The continuous variable theory discussed in Chapter 3 specifically applied to the microwave correlation-to-displacement conversion-based receivers quantum illumination setup. In conclusion, this study looked into methods based on correlation-to-displacement conversion that could be used to handle experimental imperfections in receivers. The findings showed that extra loss in heterodyne detection can be effectively compensated for by boosting the return signals. In addition, we developed a Kennedy receiver and proved that under optimal conditions, its error exponent is optimal. This receiver outperforms other known practical receivers for quantum illumination and still shows quantum advantages over classical optimal schemes in realistic scenarios. All things considered, our research demonstrates the feasibility of realistic microwave quantum illumination systems that can overcome experimental flaws and provide quantum advantages for target detection in noisy environments. These discoveries advance quantum sensing technologies and have implications for the design of upcoming quantum illumination systems.

Chapter 4 delves into the realm of entanglement within systems composed of multiple particles. The GHZ class state and the W class state are the predominant categories of states that have garnered significant focus in the study of multiparticle entanglement. It's noteworthy that the combination of GHZ and W states is not achievable through stochastic

local operations and classical communications (SLOCC); these two types of states are distinct and cannot be transformed into each other through such operations. Chapter 4 discusses two separate experimental configurations—namely, the Dicke model and the circuit QED—employed for generating the *W* state.

Chapter 5: We have discussed procedures that initiate from a direct product state and create highly entangled generalized W states. The entanglement is generated through pairwise interactions, where two qubits are brought together and allowed a specific duration for interaction at each step. This configuration imposes significant constraints on both the protocol and the resulting state. Despite enabling equal-weight superposition, it lacks the flexibility to adjust the phase difference between components. Nevertheless, these limitations lead to highly structured solutions. Geometrically, the time intervals involved can be interpreted as angles along Theodorus' spiral.

Our initial protocol is rooted in the flying-qubit model, and a practical implementation involves a cavity-photon mode that can be tuned into resonance through a set of static qubits, as demonstrated in studies such as [14, 78]. The protocol described in [55] utilized this approach to generate a generalized-W state with trapped ions, where inter-qubit interactions are sequential.

In the second protocol, inter-qubit interactions take place sequentially. A similar protocol has been realized with semiconductor spin-qubits, as documented in [70], although the primary objective in that case was to transfer a qubit-state between the ends of a chain. Our sequential protocol can be applied within the same setup to produce a generalized W state. Notably, prior research has explored qubit chains where all interactions occur simultaneously, investigating the transfer of a qubit state from one end of the chain to the other, as discussed in [42].

We have evaluated three protocols and compared them based on the required time, noting that the time for each protocol scales with the number of qubits, as illustrated in Fig. 5.3. Our analysis has focused solely on the overall interaction time, without account-

ing for potential overheads associated with moving qubits, adjusting interaction circuits, and other tasks inherent in experimental implementations. Future studies dedicated to practical realizations may consider these additional times.

Furthermore, our analysis has not addressed adiabaticity concerns, assuming that exchange interactions precisely drive the system's evolution. However, variations in interactions over time can introduce errors in practice, as discussed in, for instance, Ref. [131]. Despite these limitations, our research provides valuable approximations that can aid in protocol development. It is worth acknowledging that not all the protocols discussed here may be feasible on a given quantum computing platform. For example, in systems where qubits are arranged in a linear configuration, like ultracold atoms in optical lattices, the divide-and-conquer algorithm may not be well-suited due to the requirement for extensive qubit movement. Nevertheless, our results provide a rough estimation of the time duration for such scenarios.

6.1 Future Direction

My upcoming research direction involves investigating the benefits of the simplest experimental models to extract advantages and exploring the utilization of non-Gaussian entangled multi-mode states in Quantum Illumination C-D model setups.

In the future direction of the cavity QED setup bridge with condensed matter system, various physical systems, including Bose-Einstein condensates [64], nuclear spins [110], magnons [106], and excitons in quantum dots [139], have been utilized to realize and experimentally test the concept of superradiance. Presently, researchers are actively exploring spin-spin interactions within quantum dot spin systems, leveraging optical connections to interface with condensed matter systems [57, 138]. Two intriguing areas of investigation include the cyclic activation and deactivation of an isotopically enriched "nuclear-spin island" by electrons and the examination of superradiant-like dynamics in

the nuclear-spin bath within a single-electron quantum dot [40, 76]. The study assumes a uniform hyperfine interaction and meticulously analyzes the evolution of nuclear spin during shuttling, exploring its connection to superradiance. Additionally, the study calculates the shortest time required to exit spin evolution while maintaining adiabaticity.

The existence of long-lived dark states [23, 133], where an experimentally accessible qubit remains out of thermal equilibrium with the surrounding spin bath, is a common phenomenon in solid-state systems [114, 115]. These dark states, situated near integrable lines that share the same dark eigenstates, are prevalent in various inhomogeneous central spin models. Over extended periods, the qubit retains its initial polarization, and these dark states persist as eigenstates even under significant departures from integrability, within the range accessible to numerical simulations.

Bibliography

[1] Rising above the noise: quantum-limited amplifiers empower the readout of ibm quantum systems, baleegh abdo. https://www.ibm.com/blogs/research/2020/01/quantum-limited-amplifiers/. Accessed: 2022-01-15.

[2] G. A and L. S. *Addition of Angular Momenta: The Clebsch-Gordan Coefficients. In: Quantum Mechanics: Theory and Applications. Fundamental Theories of Physics, vol 137.* Springer Dordrecht, 2004.

[3] B. Abdo, A. Kamal, and M. Devoret. Nondegenerate three-wave mixing with the josephson ring modulator. *Phys. Rev. B*, 87:014508, 2013.

[4] P. Agrawal and A. Pati. Perfect teleportation and superdense coding with *w* states. *Phys. Rev. A*, 74:062320, Dec 2006.

[5] M. Anderlini, P. J. Lee, B. L. Brown, J. Sebby-Strabley, W. D. Phillips, and J. V. Porto. Controlled exchange interaction between pairs of neutral atoms in an optical lattice. *Nature*, 448(7152):452–456, 2007.

[6] R. Assouly, R. Dassonneville, T. Peronnin, A. Bienfait, and B. Huard. Demonstration of quantum advantage in microwave quantum radar. *arXiv:2211.05684*, 2022.

[7] K. M. R. Audenaert, J. Calsamiglia, R. Muñoz Tapia, E. Bagan, L. Masanes, A. Acin, and F. Verstraete. Discriminating states: The quantum chernoff bound. *Phys. Rev. Lett.*, 98:160501, Apr 2007.

[8] D. Awschalom, K. K. Berggren, H. Bernien, S. Bhave, L. D. Carr, P. Davids, S. E. Economou, D. Englund, A. Faraon, M. Fejer, et al. Development of quantum interconnects (quics) for next-generation information technologies. *PRX Quantum*, 2(1):017002, 2021.

[9] S. Barzanjeh, S. Guha, C. Weedbrook, D. Vitali, J. H. Shapiro, and S. Pirandola. Microwave quantum illumination. *Phys. Rev. Lett.*, 114:080503, Feb 2015.

[10] S. Barzanjeh, S. Pirandola, D. Vitali, and J. M. Fink. Microwave quantum illumination using a digital receiver. *Science Advances*, 6(19), may 2020.

[11] A. Biswas and G. S. Agarwal. Preparation of w, ghz, and two-qutrit states using bimodal cavities. *Journal of Modern Optics*, 51(11):1627–1636, 2004.

[12] Blais, Alexandre, and Wallraff. Cavity quantum electrodynamics for superconducting electrical circuits: An architecture for quantum computation. *Phys. Rev. A*, 69:062320, Jun 2004.

[13] A. D. Boozer. Time-optimal synthesis of su(2) transformations for a spin-1/2 system. *Phys. Rev. A*, 85:012317, Jan 2012.

[14] F. Borjans, X. G. Croot, X. Mi, M. J. Gullans, and J. R. Petta. Resonant microwave-mediated interactions between distant electron spins. *Nature*, 577(7789):195–198, 2020.

[15] S. L. Braunstein and P. van Loock. Quantum information with continuous variables. *Rev. Mod. Phys.*, 77:513–577, Jun 2005.

[16] B. M. Brubaker, J. M. Kindem, M. D. Urmey, S. Mittal, R. D. Delaney, P. S. Burns, M. R. Vissers, K. Lehnert, and C. A. Regal. Optomechanical ground-state cooling in a continuous and efficient electro-optic transducer. *Phys. Rev. X*, 12:021062, 2022.

[17] M. Bukov, A. G. R. Day, D. Sels, P. Weinberg, A. Polkovnikov, and P. Mehta. Reinforcement learning in different phases of quantum control. *Phys. Rev. X*, 8:031086, Sep 2018.

[18] G. Burkard, D. Loss, D. P. DiVincenzo, and J. A. Smolin. Physical optimization of quantum error correction circuits. *Phys. Rev. B*, 60:11404–11416, Oct 1999.

[19] G. C. and Z. P. *Quantum Noise*. (Springer-Verlag Berlin Heidelberg, 2004, 2004.

[20] J. Calsamiglia, R. Muñoz Tapia, L. Masanes, A. Acin, and E. Bagan. Quantum chernoff bound as a measure of distinguishability between density matrices: Application to qubit and gaussian states. *Phys. Rev. A*, 77:032311, Mar 2008.

[21] C. W. S. Chang, A. M. Vadiraj, J. Bourassa, B. Balaji, and C. M. Wilson. Quantum-enhanced noise radar. *Appl. Phys. Lett.*, 114:112601, 2019.

[22] X. Chen and Q. Zhuang. Entanglement-assisted detection of fading targets via correlation-to-coherence conversion, 2022.

[23] T. V. P. W. Claeys and A. Chandran. Persistent dark states in anisotropic central spin models. *Sci Rep 10, 16080 (2020).*

[24] G. G. Claude Cohen-Tannoudji, Jacques Dupont-Roc. *A Survey of Some Interaction Processes Between Photons and Atoms*, chapter 2, pages 67–163. John Wiley and Sons, Ltd, 1998.

[25] D. C. Cole, J. J. Wu, S. D. Erickson, P.-Y. Hou, A. C. Wilson, D. Leibfried, and F. Reiter. Dissipative preparation of w states in trapped ion systems. *New Journal of Physics*, 23(7):073001, jul 2021.

[26] P. Davis, W. Gautschi, and A. Iserles. *Spirals: From Theodorus to Chaos*. Taylor & Francis, 1993.

[27] A. G. R. Day, M. Bukov, P. Weinberg, P. Mehta, and D. Sels. Glassy phase of optimal quantum control. *Phys. Rev. Lett.*, 122:020601, Jan 2019.

[28] V. Devanathan. *Angular Momentum Techniques in Quantum Mechanics.* Springer Dordrecht, Published: 08 December 2010.

[29] R. Di Candia, H. Yiğitler, G. Paraoanu, and R. Jäntti. Two-way covert quantum communication in the microwave regime. *PRX Quantum*, 2:020316, May 2021.

[30] R. H. Dicke. Coherence in spontaneous radiation processes. *Phys. Rev.*, 93:99–110, Jan 1954.

[31] A. V. Dixit, S. Chakram, K. He, A. Agrawal, R. K. Naik, D. I. Schuster, and A. Chou. Searching for dark matter with a superconducting qubit. *Phys. Rev. Lett.*, 126(14):141302, 2021.

[32] L.-M. Duan, G. Giedke, J. I. Cirac, and P. Zoller. Inseparability criterion for continuous variable systems. *Phys. Rev. Lett.*, 84:2722–2725, Mar 2000.

[33] W. Dür, G. Vidal, and J. I. Cirac. Three qubits can be entangled in two inequivalent ways. *Phys. Rev. A*, 62:062314, Nov 2000.

[34] W. Dür, G. Vidal, and J. I. Cirac. Three qubits can be entangled in two inequivalent ways. *Phys. Rev. A*, 62:062314, Nov 2000.

[35] A. Einstein, B. Podolsky, and N. Rosen. Can quantum-mechanical description of physical reality be considered complete? *Phys. Rev.*, 47:777–780, May 1935.

[36] D. G. England, B. Balaji, and B. J. Sussman. Quantum-enhanced standoff detection using correlated photon pairs. *Phys. Rev. A*, 99:023828, Feb 2019.

[37] J. E.T., Cummings, and F.W. Comparison of quantum and semiclassical radiation theories with application to the beam maser. *Proceedings of the IEEE*, 51(1):89–109, 1963.

[38] K. A. H. S. P. M. et al. Experimental realization of controlled quantum teleportation of arbitrary qubit states via cluster states.

[39] L. Fan, C.-L. Zou, R. Cheng, X. Guo, X. Han, Z. Gong, S. Wang, and H. X. Tang. Superconducting cavity electro-optics: a platform for coherent photon conversion between superconducting and photonic circuits. *Sci. Adv.*, 4(8):eaar4994, 2018.

[40] Y. Fang, Y.-D. Wang, R. Fazio, and S. Chesi. Superradiantlike dynamics of nuclear spins by nonadiabatic electron shuttling. *Phys. Rev. B*, 103:155301, Apr 2021.

[41] A. Ferraro, S. Olivares, and M. G. A. Paris. Gaussian states in continuous variable quantum information, 2005.

[42] A. Ferrón, P. Serra, and O. Osenda. Understanding the propagation of excitations in quantum spin chains with different kind of interactions. *Physica Scripta*, 97(11):115103, oct 2022.

[43] E. Flurin, N. Roch, F. Mallet, M. Devoret, and B. Huard. Generating entangled microwave radiation over two transmission lines. *Phys. Rev. Lett.*, 109:183901, 2012.

[44] M. Fox. *Quantum Optics: An Introduction*. Oxford University Press, 2006, 2006.

[45] R. Ganesh, L. Theerthagiri, and G. Baskaran. Generating resonating-valence-bond states through dicke subradiance. *Phys. Rev. A*, 96:033829, Sep 2017.

[46] R. Ganesh, L. Theerthagiri, and G. Baskaran. Resonating valence bonds and spinon pairing in the Dicke model. *SciPost Phys.*, 4:044, 2018.

[47] J. Gao, L. Santos, G. Krishna, Z.-S. Xu, A. Iovan, S. Steinhauer, O. Gühne, P. J. Poole, D. Dalacu, V. Zwiller, and A. W. Elshaari. Scalable generation and detection of on-demand w states in nanophotonic circuits. *Nano Letters*, 23(11):5350–5357, 2023. PMID: 37224010.

[48] B. M. . Garraway. The dicke model in quantum optics: Dicke model revisited. *Philosophical Transactions of the Royal Society A: Mathematical, Physical and Engineering Sciences. Royal Society.*

[49] J. Geng, Y. Wu, X. Wang, K. Xu, F. Shi, Y. Xie, X. Rong, and J. Du. Experimental time-optimal universal control of spin qubits in solids. *Phys. Rev. Lett.*, 117:170501, Oct 2016.

[50] R. J. Glauber. Coherent and incoherent states of the radiation field. *Physical Review*, 131(6):2766, 1963.

[51] V. Gorbachev, A. Trubilko, A. Rodichkina, and A. Zhiliba. Can the states of the w-class be suitable for teleportation? *Physics Letters A*, 314(4):267–271, 2003.

[52] M. Gräfe, R. Heilmann, A. Perez-Leija, R. Keil, F. Dreisow, M. Heinrich, H. Moya-Cessa, S. Nolte, D. N. Christodoulides, and A. Szameit. On-chip generation of high-order single-photon w-states. *Nature Photonics*, 8(10):791–795, 2014.

[53] D. Gronau. The spiral of theodorus. *The American Mathematical Monthly*, 111(3):230–237, 2004.

[54] S. Guha and B. I. Erkmen. Gaussian-state quantum-illumination receivers for target detection. *Physical Review A*, 80(5), nov 2009.

[55] H. Häffner, W. Hänsel, C. F. Roos, J. Benhelm, D. Chek-al kar, M. Chwalla, T. Körber, U. D. Rapol, M. Riebe, P. O. Schmidt, C. Becher, O. Gühne, W. Dür, and R. Blatt. Scalable multiparticle entanglement of trapped ions. *Nature*, 438(7068):643–646, 2005.

[56] X. Han, W. Fu, C.-L. Zou, L. Jiang, and H. X. Tang. Microwave-optical quantum frequency conversion. *Optica*, 8(8):1050–1064, 2021.

[57] R. Hanson, L. P. Kouwenhoven, J. R. Petta, S. Tarucha, and L. M. K. Vandersypen. Spins in few-electron quantum dots. *Rev. Mod. Phys.*, 79:1217–1265, Oct 2007.

[58] C. W. Helstrom. Minimum mean-squared error of estimates in quantum statistics. *Phys. Lett. A*, 25(2):101–102, 1967.

[59] C. W. Helstrom. Quantum detection and estimation theory. *J. Stat. Phys.*, 1:231, June 1969.

[60] C. W. Helstrom. *Quantum Detection and Estimation Theory*. Mathematics in Science and Engineering: a series of monographs and textbooks. Academic Press, 1976.

[61] S. Hermelin, S. Takada, and etc. Electrons surfing on a sound wave as a platform for quantum optics with flying electrons. *Nature 477, 435–438 (2011).*

[62] E. Hlawka. Gleichverteilung und quadratwurzelschnecke. *Monatshefte für Mathematik*, 89(1):19–44, 1980.

[63] R. Horodecki, P. Horodecki, M. Horodecki, and K. Horodecki. Quantum entanglement. *Rev. Mod. Phys.*, 81:865–942, Jun 2009.

[64] S. Inouye, A. P. Chikkatur, D. M. Stamper-Kurn, J. Stenger, D. E. Pritchard, and W. Ketterle. Superradiant rayleigh scattering from a bose-einstein condensate. *Science*, 285(5427):571–574, 1999.

[65] D. Jenn. *Radarand Laser Cross Section Engineering*. American Institute of Aeronautics and Astronautics, Inc.(2005).

[66] Ji, Y. Shao, and etc. Fusing atomic w states via quantum zeno dynamics. *Sci Rep 7, 1378 (2017).*

[67] J. Joo, Y.-J. Park, S. Oh, and J. Kim. Quantum teleportation via a w state. *New Journal of Physics*, 5(1):136, oct 2003.

[68] K. H. Kagalwala, G. Di Giuseppe, A. F. Abouraddy, and B. E. A. Saleh. Single-photon three-qubit quantum logic using spatial light modulators. *Nature Communications*, 8(1):739, 2017.

[69] Kamimaki, Wakamatsu, Mikata, and et al. Deterministic bell state measurement with a single quantum memory. *npj Quantum Inf 9, 101 (2023).*

[70] Y. P. Kandel, H. Qiao, S. Fallahi, G. C. Gardner, M. J. Manfra, and J. M. Nichol. Coherent spin-state transfer via heisenberg exchange. *Nature*, 573(7775):553–557, 2019.

[71] Y. P. Kandel, H. Qiao, and J. M. Nichol. Perspective on exchange-coupled quantum-dot spin chains. *Applied Physics Letters*, 119(3):030501, 2021.

[72] Kang and Q. et al. Fast generation of w states of superconducting qubits with multiple schrödinger dynamics. *Sci Rep 6, 36737*, (2016).

[73] A. Karsa, A. Fletcher, G. Spedalieri, and S. Pirandola. Quantum illumination and quantum radar: A brief overview, 2023.

[74] A. Karsa and S. Pirandola. Noisy receivers for quantum illumination. *IEEE Aerospace and Electronic Systems Magazine*, 35(11):22–29, 2020.

[75] G. Kraftmakher, V. Butylkin, Y. Kazantsev, and V. Mal'tsev. New functionality in microwave interferometry by application of metastructure as a tunable beam-splitter. *J. Phys.: Conf. Ser.*, 1461:012074, 2020.

[76] Z. Kurucz, M. W. Sørensen, J. M. Taylor, M. D. Lukin, and M. Fleischhauer. Qubit protection in nuclear-spin quantum dot memories. *Phys. Rev. Lett.*, 103:010502, Jul 2009.

[77] G. Lachs. Theoretical aspects of mixtures of thermal and coherent radiation. *Phys. Rev.*, 138(4 B):B 1012, 1965.

[78] Landig, Koski, and etc. Virtual-photon-mediated spin-qubit–transmon coupling. *Nature Communications*, 10(1):5037, 2019.

[79] M. Lanzagorta. *Classical Radar Theory*, pages 61–88. Springer International Publishing, Cham, 2012.

[80] N. Lauk, N. Sinclair, S. Barzanjeh, J. P. Covey, M. Saffman, M. Spiropulu, and C. Simon. Perspectives on quantum transduction. *Quantum Science and Technology*, 5(2):020501, 2020.

[81] N. B. Lenander and et al. Generation of three-qubit entangled states using superconducting phase qubits. *Nature 467, 570–573 (2010)*.

[82] J. Li, K. Chalapat, and G. S. Paraoanu. Entanglement of superconducting qubits via microwave fields: Classical and quantum regimes. *Phys. Rev. B*, 78:064503, Aug 2008.

[83] S. Lloyd. Enhanced sensitivity of photodetection via quantum illumination. *Science*, 321(5895):1463–1465, 2008.

[84] E. D. Lopaeva, I. Ruo Berchera, I. P. Degiovanni, S. Olivares, G. Brida, and M. Genovese. Experimental realization of quantum illumination. *Phys. Rev. Lett.*, 110:153603, Apr 2013.

[85] D. Loss and D. P. DiVincenzo. Quantum computation with quantum dots. *Phys. Rev. A*, 57:120–126, Jan 1998.

[86] D. Luong, C. W. S. Chang, A. M. Vadiraj, A. Damini, C. M. Wilson, and B. Balaji. Receiver operating characteristics for a prototype quantum two-mode squeezing radar. *IEEE Transactions on Aerospace and Electronic Systems*, 56(3):2041–2060, 2020.

[87] X.-S. Ma, S. Zotter, N. Tetik, A. Qarry, T. Jennewein, and A. Zeilinger. A high-speed tunable beam splitter for feed-forward photonic quantum information processing. *Optics Express*, 19(23):22723–22730, 2011.

[88] L. L. Marco G. Genoni and A. Serafini. Conditional and unconditional gaussian quantum dynamics. *Contemporary Physics*, 57(3):331–349, 2016.

[89] P. Marian and T. A. Marian. Squeezed states with thermal noise. i. photon-number statistics. *Phys. Rev. A*, 47:4474–4486, May 1993.

[90] e. Markus Gräfe, René Heilmann. On-chip generation of high-order single-photon w-states. *Nature Photonics volume 8, pages791–795 (2014)*.

[91] B. M. Maune, M. G. Borselli, B. Huang, T. D. Ladd, P. W. Deelman, K. S. Holabird, A. A. Kiselev, I. Alvarado-Rodriguez, R. S. Ross, A. E. Schmitz, M. Sokolich, C. A. Watson, M. F. Gyure, and A. T. Hunter. Coherent singlet-triplet oscillations in a silicon-based double quantum dot. *Nature*, 481(7381):344–347, 2012.

[92] O. Menegasso Pires, E. Inacio Duzzioni, J. Marchi, and R. De Santiago. Quantum circuit synthesis using projective simulation. *Inteligencia Artificial*, 24(67):90–101, Apr. 2021.

[93] J. Miguel-Ramiro, F. Riera-Sàbat, and W. Dür. Quantum repeater for w states. 2023.

[94] M.I.Skolnik. *Introductionto radar*. McGraw-Hill, 2008.

[95] Mlynek, A. A., E. C., and et al. Observation of dicke superradiance for two artificial atoms in a cavity with high decay rate. *Nat Commun 5, 5186 (2014).*

[96] R. Nair and M. Gu. Fundamental limits of quantum illumination. *Optica*, 7(7):771–774, Jul 2020.

[97] Neeley, Matthew, Bialczak, and etc. Generation of three-qubit entangled states using superconducting phase qubits. *Nature*, 467(7315):570–573, 2010.

[98] M. A. Nielsen and I. L. Chuang. *Quantum Computation and Quantum Information:*. 10th Anniversary Edition. Cambridge: Cambridge University Press., 2010.

[99] S. Olivares. *Quantum optics in the phase space*, volume 203. American Physical Society, 2012.

[100] G. D. Palma and J. Borregaard. Minimum error probability of quantum illumination. *Phys. Rev. A*, 98(1):012101, 2018.

[101] A. Perez-Leija, J. C. Hernandez-Herrejon, H. Moya-Cessa, A. Szameit, and D. N. Christodoulides. Generating photon-encoded *w* states in multiport waveguide-array systems. *Phys. Rev. A*, 87:013842, Jan 2013.

[102] J. R. Petta, A. C. Johnson, J. M. Taylor, E. A. Laird, A. Yacoby, M. D. Lukin, C. M. Marcus, M. P. Hanson, and A. C. Gossard. Coherent manipulation of coupled

electron spins in semiconductor quantum dots. *Science*, 309(5744):2180–2184, 2005.

[103] S. Pirandola, B. R. Bardhan, T. Gehring, C. Weedbrook, and S. Lloyd. Advances in photonic quantum sensing. *Nat. Photonics*, 12(12):724–733, 2018.

[104] S. Pirandola and S. Lloyd. Computable bounds for the discrimination of gaussian states. *Phys. Rev. A*, 78:012331, Jul 2008.

[105] S. Pirandola, A. Serafini, and S. Lloyd. Correlation matrices of two-mode bosonic systems. *Phys. Rev. A*, 79:052327, May 2009.

[106] S. M. Rezende. Theory of microwave superradiance from a bose-einstein condensate of magnons. *Phys. Rev. B*, 79:060410, Feb 2009.

[107] M. Richards, J. Scheer, and W. Holm. *Principles of Modern Radar*. Number v. 3 in Principles of Modern Radar. SciTech Pub., 2010.

[108] M. A. Richards. Fundamentals of radar signal processing. *US: McGraw-Hill Professional,*, Jun 2005.

[109] L. Russ and A. DeVoogt. *The Complete Mancala Games Book: How To Play the World's Oldest Board Games*. Da Capo Press, 1999.

[110] R. Röhlsberger, K. Schlage, B. Sahoo, S. Couet, and R. Rüffer. Collective lamb shift in single-photon superradiance. *Science*, 328(5983):1248–1251, 2010.

[111] M. F. Sacchi. Optimal discrimination of quantum operations. *Phys. Rev. A*, 71:062340, Jun 2005.

[112] R. Sahu, L. Qiu, W. Hease, G. Arnold, Y. Minoguchi, P. Rabl, and J. M. Fink. Entangling microwaves with optical light. *arXiv preprint arXiv:2301.03315*, 2023.

[113] J. J. Sakurai and J. Napolitano. *Modern Quantum Mechanics.* Cambridge University Press., 2nd edn., 2017.

[114] M. J. A. Schuetz, E. M. Kessler, L. M. K. Vandersypen, J. I. Cirac, and G. Giedke. Steady-state entanglement in the nuclear spin dynamics of a double quantum dot. *Phys. Rev. Lett.*, 111:246802, Dec 2013.

[115] M. J. A. Schuetz, E. M. Kessler, L. M. K. Vandersypen, J. I. Cirac, and G. Giedke. Nuclear spin dynamics in double quantum dots: Multistability, dynamical polarization, criticality, and entanglement. *Phys. Rev. B*, 89:195310, May 2014.

[116] M. O. Scully. Single photon subradiance: Quantum control of spontaneous emission and ultrafast readout. *Phys. Rev. Lett.*, 115:243602, Dec 2015.

[117] M. O. Scully and M. S. Zubairy. *Quantum Optics*. Cambridge University Press, 1997.

[118] A. Serafini. *Quantum Continuous Variables*, volume 203. A Primer of Theoretical Methods (1st ed.). CRC Press., 2017.

[119] J. H. Shapiro. Extended version of van trees's receiver operating characteristic approximation. *IEEE Transactions on Aerospace and Electronic Systems*, 35(2):709–716, 1999.

[120] J. H. Shapiro. The quantum illumination story. *IEEE Trans. Aerosp. Electron. Syst.*, 35(4):8–20, 2020.

[121] J. H. Shapiro and S. Lloyd. Quantum illumination versus coherent-state target detection. *New Journal of Physics*, 11(6):063045, jun 2009.

[122] A. Sharma and A. A. Tulapurkar. Generation of *n*-qubit *w* states using spin torque. *Phys. Rev. A*, 101:062330, Jun 2020.

[123] H. Shi, B. Zhang, and Q. Zhuang. Fulfilling entanglement's benefit via converting correlation to coherence. *arXiv:2207.06609*, 2022.

[124] H. Shi, B. Zhang, and Q. Zhuang. Fulfilling entanglement's optimal advantage via converting correlation to coherence, 2023.

[125] H. Shi, Z. Zhang, and Q. Zhuang. Practical route to entanglement-assisted communication over noisy bosonic channels. *Phys. Rev. Applied*, 13:034029, Mar 2020.

[126] R. Simon. Peres-horodecki separability criterion for continuous variable systems. *Phys. Rev. Lett.*, 84:2726–2729, Mar 2000.

[127] G. Sorelli, N. Treps, F. Grosshans, and F. Boust. Detecting a target with quantum entanglement. *IEEE Aerospace and Electronic Systems Magazine*, 37(5):68–90, 2022.

[128] G. Spedalieri and S. Pirandola. Optimal squeezing for quantum target detection. *Phys. Rev. Res.*, 3:L042039, Dec 2021.

[129] E. C. G. Sudarshan. Equivalence of semiclassical and quantum mechanical descriptions of statistical light beams. *Phys. Rev. Lett.*, 10:277–279, Apr 1963.

[130] M. Swain, V. Devrari, A. Rai, B. K. Behera, and P. K. Panigrahi. Generation of perfect w-state and demonstration of its application to quantum information splitting. 2020.

[131] T. Sägesser, R. Matt, R. Oswald, and J. P. Home. Robust dynamical exchange cooling with trapped ions. *New Journal of Physics*, 22(7):073069, jul 2020.

[132] M. Takeoka and M. Sasaki. Discrimination of the binary coherent signal: Gaussian-operation limit and simple non-gaussian near-optimal receivers. *Phys. Rev. A*, 78:022320, Aug 2008.

[133] V. Tamiro and etc. Integrability and dark states in an anisotropic central spin model. *Phys. Rev. Res.*, 2:032052, Aug 2020.

[134] S.-H. Tan, B. I. Erkmen, V. Giovannetti, S. Guha, S. Lloyd, L. Maccone, S. Pirandola, and J. H. Shapiro. Quantum illumination with gaussian states. *Phys. Rev. Lett.*, 101(25):253601, 2008.

[135] T. Tashima, T. Wakatsuki, S. K. Ozdemi, T. Yamamoto, M. Koashi, and N. Imoto. Preparation of a three-photon w state from two epr photon pairs by locc. In *CLEO/Europe - EQEC 2009 - European Conference on Lasers and Electro-Optics and the European Quantum Electronics Conference*, pages 1–1, 2009.

[136] K. Tatsuhiko. Quantum brachistochrone. *Phil. Trans. R. Soc. A.*, 380:20210273, 2022.

[137] M. Tavis and F. W. Cummings. Exact solution for an *n*-molecule—radiation-field hamiltonian. *Phys. Rev.*, 170:379–384, Jun 1968.

[138] J. M. Taylor, A. Imamoglu, and M. D. Lukin. Controlling a mesoscopic spin environment by quantum bit manipulation. *Phys. Rev. Lett.*, 91:246802, Dec 2003.

[139] P. Tighineanu, R. S. Daveau, T. B. Lehmann, H. E. Beere, D. A. Ritchie, P. Lodahl, and S. Stobbe. Single-photon superradiance from a quantum dot. *Phys. Rev. Lett.*, 116:163604, Apr 2016.

[140] R. G. Torrome and S. Barzanjeh. Advances in quantum radar and quantum lidar, 2023.

[141] S. van Frank, M. Bonneau, J. Schmiedmayer, S. Hild, C. Gross, M. Cheneau, I. Bloch, T. Pichler, A. Negretti, T. Calarco, and S. Montangero. Optimal control of complex atomic quantum systems. *Sci Rep*, 6:34187, Oct 2016.

[142] D. J. van Woerkom and e. Scarlino. Microwave photon-mediated interactions between semiconductor qubits. *Phys. Rev. X*, 8:041018, Oct 2018.

[143] Wallraff, Schuster, Blais, and et al. Strong coupling of a single photon to a superconducting qubit using circuit quantum electrodynamics. *Nature 431, 162–167 (2004).*

[144] X.-B. Wang, T. Hiroshima, A. Tomita, and M. Hayashi. Quantum information with gaussian states. *Physics Reports*, 448(1):1–111, 2007.

[145] P. Weedbrook, Christian. Gaussian quantum information. *Rev. Mod. Phys.*, 84:621–669, May 2012.

[146] F. Wu, L. Tang, M.-Q. Bai, and Z.-W. Mo. Multi-hop quantum teleportation with ghz-class states and bell states in quantum networks. *Physica A: Statistical Mechanics and its Applications*, 625:129022, 2023.

[147] e. Y. Q. Ji, X. Q. Fusing atomic w states via quantum zeno dynamics. *Sci Rep,*, 101:1378, 2017.

[148] B. K. B. . P. K. P. Yagnik Chatterjee, Vipin Devrari. Experimental realization of quantum teleportation using coined quantum walks. *Quantum Information Processing volume 19, Article number: 31 (2020).*

[149] e. Yi-Hao Kang, Ye-Hong Chen. Fast generation of w states of superconducting qubits with multiple schrödinger dynamics. *Sci Rep,*, 101:36737, 2016.

[150] e. Zang, Yang. Generating multi-atom entangled w states via light-matter interface based fusion mechanism. *Sci Rep 5, 16245*, (2015).

[151] Z. Zhang, S. Mouradian, F. N. C. Wong, and J. H. Shapiro. Entanglement-enhanced sensing in a lossy and noisy environment. *Phys. Rev. Lett.*, 114:110506, Mar 2015.

[152] Q. Zhuang. Quantum ranging with gaussian entanglement. *Phys. Rev. Lett.*, 126(24):240501, 2021.

[153] Q. Zhuang and J. H. Shapiro. Ultimate accuracy limit of quantum pulse-compression ranging. *Phys. Rev. Lett.*, 128(1):010501, 2022.

[154] Q. Zhuang, Z. Zhang, and J. H. Shapiro. Optimum mixed-state discrimination for noisy entanglement-enhanced sensing. *Phys. Rev. Lett.*, 118:040801, Jan 2017.

[155] N. Zou. Quantum entanglement and its application in quantum communication. *Journal of Physics: Conference Series*, 1827(1):012120, mar 2021.